Stable laser-driven proton acceleration in ultra-relativistic laser-plasma interaction

Inaugural-Dissertation

zur

Erlangung des Doktorgrades der
Mathematisch-Naturwissenschaftlichen Fakultät
der

vorgelegt von

Tong-Pu Yu

aus Yuexi, China

August 2011

Aus dem Institut für Theoretische Physik I
der Heinrich-Heine-Universität Düsseldorf

Gedruckt mit der Genehmigung der
Mathematisch-Naturwissenschaftlichen Fakultät
der Heinrich-Heine-Universität Düsseldorf

Referent: Prof. Dr. A. Pukhov
Korreferent: Prof. Dr. K.H. Spatschek

Tag der mündlichen Prüfung: 06.10.2011

Zusammenfassung

Aufgrund großen Potentials in den Bereichen Medizin, Trägheitsfusion und in der Protonenbildgebung genießt die lasergetriebene Ionenbeschleunigung in den letzten Jahren wachsende Aufmerksamkeit. In der vorliegenden Dissertation wird einer der effizientesten und erfolgversprechendsten Mechanismen zur Ionenbeschleunigung, die so genannte Strahlendruckbeschleunigung oder das Lichtsegel-Regime, vorgestellt und im Detail untersucht mithilfe von mehrdimensionalen particle-in-cell (PIC) Simulationen. Basierend auf einem einfachen "flying plasma mirror"-Modell leiten wir Skalierungsgesetze für die erreichten Ionenenergien, -geschwindigkeiten und für die Energiekopplungseffizienz im Lichtsegel-Regime her. Diese Skalierungsgesetze wurden mit eindimensionalen PIC-Simulationen bestätigt.

Jedoch treten mehrere Probleme auf, sobald wir das Modell auf den mehrdimensionalen Fall erweitern, wie zum Beispiel Deformation des zu beschleunigenden Ziels und transversale Instabilitäten. Um die Deformation zu vermeiden stellen wir ein angepasstes Folienziel vor (shaped foil target, SFT), welches die zu beschleunigenden Strukturen länger bewahrt als ein einfaches, flaches Ziel. PIC-Simulationen belegen dies und weisen außerdem im Energiespektrum klare mono-energetische Eigenschaften auf. Um die Stabilität des Verfahrens zu bewerten, haben wir mehrere Parameter untersucht, wie zum Beispiel die Oberflächenbeschaffenheit und das transversale Profil des Ziels. Darüber hinaus stellen wir ein weiteres Verfahren vor, das dichtemodulierte Folienziel (density modulated foil target, DMFT). In diesem Verfahren ist das zu beschleunigende Ziel flach, hat jedoch ein transversales Dichteprofil, das einer Gaußverteilung folgt, um dem Laserintensitätsprofil zu entsprechen. Sowohl 2D- als auch 3D-Simulationen zeigen, dass Ionen im Zentrum des Ziels quasi-monoenergetisch und gerichtet beschleunigt werden. Die Strahlqualitäten hierbei sind deutlich besser als im Fall des SFT.

Mehrdimensionale PIC-Simulationen zeigen, dass Rayleigh-Taylor ähnliche (RT) Instabilitäten merklich unterdrückt werden können bei der Verwendung der darüber hinaus vorgestellten zwei-Ionenspezies angepassten Folien (two-ion-species shaped foil). Wir stellen ein einfaches drei-Oberflächenmodell vor für die Unterdrückung der RT-ähnlichen Instabilitäten, welches gut übereinstimmt mit numerischen Beobachtungen in einer Vielzahl an Fällen. Die Gründe hierfür sind: Separation der Ionenspezies und die räumliche Verteilung der schwereren Ionen. Die schwereren Kohlenstoffionen wirken wie ein Puffer gegen die RT-ähnliche

Instabilität für die kompakte Lage der leichteren Protonen. Wir fanden des weiteren heraus, dass mit sinkendem Ionisationsgrad der Kohlenstoffionen sowohl RT-ähnliche Instabilitäten als auch Coulomb-Explosionen immer wichtiger werden und die Eigenschaften des quasi-monoenergetischen Protonenstrahls negativ beeinflussen.

Im Hinblick auf hochintensive Laserpulse im Lichtsegel-Regime studieren wir Effekte von Strahlungsreaktions auf Ionenbeschleunigung. Dafür modifizieren wir einen PIC-Code entsprechend des Impulserhaltungsgesetzes. Zu jedem Zeitpunkt während der Simulation gehen wir davon aus, dass das Strahlungspektrum Synchrotroncharakter hat und dass die relativistischen Elektronen in Impulsrichtung Strahlung emittieren. Mit dem modifizierten Code untersuchen wir die Elektronendynamik im Lichtsegel-Regime und beobachten die Erzeugung von GeV Elektronenbündel in Attosekundenlängen. In longitudinale Richtung bewegen sich die Elektronen zusammen mit den Protonen während sie um diese in Transversalrichtung rotieren. Wenn die Rotationsfrequenz der Elektronen sich an die Laserfrequenz annähert, erfolgt Betatronresonanz und effiziente Energieübertragung vom Laser zu den Elektronen. Zu diesem Zeitpunkt können harte Röntgenstrahlen und sogar Gammastrahlen beobachten werden, welche verschiedene Anwendung zum Beispiel in der Medizin oder der Plasmadiagnostik haben könnten.

Abstract

With a lot of potential applications in oncology, proton imaging and inertial confinement fusion, laser-driven ion acceleration has drawn increasing attention these years. In this dissertation, one of the most efficient and promising ion acceleration mechanisms, so-called radiation pressure acceleration or light-sail regime is re-visited and studied in detail by multi-dimensional particle-in-cell (PIC) simulations. Based on a simple "flying plasma mirror" model, we derive accurate scaling laws of the final ion energy, velocity, and energy coupling efficiency in the light-sail regime. These laws have been well demonstrated by a series of one-dimensional PIC simulations.

However, when we extend the model to multi-dimensional cases, several issues take place such as foil target deformation and transverse instabilities. To overcome the foil target deformation, a shaped foil target (SFT) is suggested, which can help keeping the acceleration structure for a longer time as compared to a normal flat target. The final energy spectrum shows a monoenergetic character. To demonstrate the robustness of the scheme, several facts such as the surface roughness and the transverse profile of the shaped foil are evaluated. Furthermore, an alternative scheme, namely, density modulated foil target (DMFT) is proposed. In this case, the initial foil target is a flat one, but the transverse plasma density follows a Gaussian distribution to match the laser intensity profile. Both 2D and 3D simulations show that the protons from the center part of the target can be monochromatically accelerated and are well collimated in the forward direction. Overall, the beam quality is much improved as compared to the case using a SFT.

Multi-dimensional PIC simulations also show that Rayleigh-Taylor-like (RT) instability can be significantly suppressed by using the additionally proposed two-ion-species shaped foil. A simple three-interface model is proposed to interpret the suppression of the proton-RT instability, which agrees well with the numerical observations in a variety of cases. This should be attributed to two effects: ion species separation and heavier ion spreading in space. The heavier ions (carbon ions) act to buffer the compact lighter layer (protons) from the RT-like instability. It is also found that with the decrease of the carbon ions charge state, both the RT instability and Coulomb explosion become increasingly violent and tend to degrade the monoenergetic proton beam.

In view of intense laser pulses in the light-sail regime, we also study the radiation reaction

effects on the ion acceleration. The PIC code is modified according to the momentum conservation law. At any given time, we suppose that the radiation spectrum is synchrotron-like and the relativistic electrons emit radiation along their momentum direction. By using the modified code, we study the electron dynamics in the light-sail regime and observe the generation of GeV spiral electron bunches with an obvious attosecond structure. The electrons move together with the protons longitudinally and rotate dramatically around the latter in the transverse direction. When the oscillation frequency of the electron gets close to the laser frequency as witnessed by the electron, a betatron-like resonance occurs and an effective energy exchange between the laser and electron takes place. Such energetic spiral electron bunches would be of great interest for the emission of efficient betatron-like X-ray and even γ burst, which might have diverse applications, e.g., in oncology and plasma diagnostics.

Contents

List of Figures

List of Tables

Chapter 1

Introduction

With the rapid development of laser technologies after the invention of chirped pulse amplification (CPA) [1, 2], laser systems are capable of delivering radiation in excess of 1 PW with peak laser intensities well above the threshold $10^{18}\mathrm{Wcm}^{-2}$. The quiver velocity of electrons in this laser field approaches the speed of light c with energies comparable to their rest energies $m_\mathrm{e}c^2$ where m_e is the electron rest mass. It is generally considered as relativistic laser-plasma interaction because the bulk of electrons starts to oscillate at relativistic velocities. Under the influence of such a relativistic laser pulse, foils or other materials are immediately ionized via above-threshold ionization (ATI) process [3], tunnel ionization process [4] or multi-photon ionization process [5] and plasma is formed [6]. The interaction between the laser radiation and plasma sets in, which gives rise to a new branch of physics called relativistic optics or the physics of relativistic laser-plasma interaction including effects such as high harmonics generation [7, 8, 9], THz radiation [10, 11], laser-driven particle beam acceleration [12, 13], and attosecond nonlinear optics [14, 15], etc. Among these, laser-plasma based ion accelerators have drawn increasing attention due to their unique features, e.g., compact size, low beam emittance, low cost, and high accelerating gradient [16, 17, 18]. These advantages make laser-accelerated ions potential candidates for many applications such as particle acceleration, fast ignition for inertial confinement fusion (ICF) [19], ion injection into conventional accelerators [14], and medical therapy for cancer.

In the last decades, both theoretical and experimental studies have contributed to achieving energetic ion beams and to improving the beam quality, e.g., higher peak energy, lower beam divergency, narrower energy spread, and larger particle flux. Several ion acceleration mechanisms were proposed theoretically, studied by the use of multi-dimensional particle-in-cell (PIC) simulations, and demonstrated experimentally. However, the beam quality is still far

away from the requirements of practical applications. Recently, one of the most efficient and promising ion acceleration mechanisms, so-called radiation pressure acceleration (RPA) or light-sail regime [13, 20, 21] is re-visited. It is shown that the light-sail regime might be a unique method to obtain GeV high quality proton beams with current laser intensities. However, several issues such as foil target deformation and transverse instabilities [13, 22, 23] have to be overcome because these multi-dimensional effects tend to degrade the stable acceleration structure and result in a broad ion energy spectrum. Previous studies showed that a properly tailored laser pulse with a sharp intensity rise might stabilize the foil acceleration [13]. However, the transverse instability is still unavoidable though its growth gate is smaller.

In this dissertation, we concentrate on these multi-dimensional effects and try to find some solutions to overcome the foil deformation and transverse instabilities. For a typical Gaussian laser pulse in experiments, we might modify the foil parameters or the laser profile to overcome the foil deformation during the interaction of a laser beam with an ultra-thin foil. In Chapter 3 and 4, two schemes are proposed by the use of a shaped foil target or a density modulated foil target. In order to overcome the transverse instabilities, e.g., Rayleigh-Taylor-like (RT) instability, a two-ion-species shaped foil target is proposed in Chapter 5, by which we might get a stable proton beam acceleration. In Chapter 6, the effects of the radiation reaction (RR) on the proton/ion acceleration are checked and evaluated because the electromagnetic field emitted by each relativistic electron might influence the motion of the electron itself and thus the ion acceleration through space-charge fields. Previous studies showed that this effect should become essential under the extreme conditions, e.g., laser intensities above $10^{22}\mathrm{Wcm}^{-2}$ [24]. Finally, it is a summary to the whole dissertation and an outlook of the ion acceleration in the light-sail regime is also given.

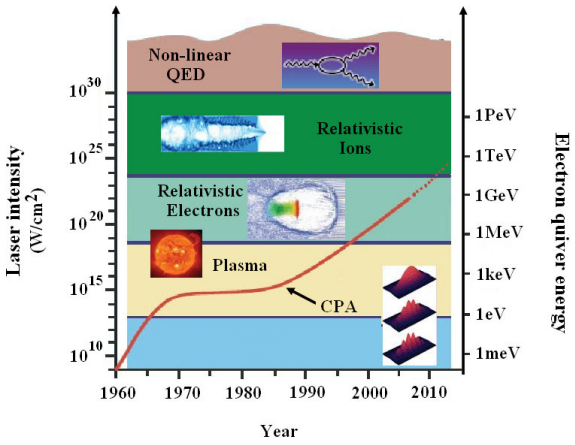

Figure 1.1: History of laser output power density growth.

Before addressing this new kind ion acceleration mechanism, it is worth having a short review of recent progresses on both laser technologies and laser-driven particle acceleration to better understand the work expounded in this dissertation. In the following, we first recall the CPA invention which increased the laser radiation intensity by 5-6 orders of magnitude, up to $2.2 \times 10^{22}\mathrm{Wcm}^{-2}$ [25, 26]. This is the primary impetus behind the laser-driven particle acceleration in the last decades (see Fig. 1.1). Benefitting from the CPA technology, laser-driven electron acceleration made a significant progress in the last years [27]. A few to a few tens of GeV electron beams have been reported in experiments by several groups [28, 29]. By contrast, laser-driven ion acceleration has a shorter history due to the larger ion mass ($m_{\mathrm{H}} \approx 1836 m_{\mathrm{e}}$). However, laser-driven ion acceleration has attracted increasing attention since the proposal of the ion acceleration mechanism, target normal sheath acceleration (TNSA) [30]. In the third section of this chapter, we concentrate on both theoretical and experimental developments of TNSA as well as its drawbacks and inherit problems for future applications. This also paves the way for the introduction of the new ion acceleration mechanism, i.e., the light-sail regime.

1.1 Chirp pulse amplification (CPA)

Before the advent of CPA, the laser intensity was limited to the level of $10^{14}\mathrm{Wcm}^{-2}$ despite of using Q switching [31] and mode-locking technique [32]. Above this level, non-linear effects, e.g., radiation self-focusing and optical damage in the amplifiers and optical components take place which slowed down the further increase of the laser intensity [14, 33]. In order to keep the intensity of laser pulses below the threshold of the nonlinear effects, the laser systems had to be large-size, low-efficiency, expensive and unwieldy. In 1985, the physicists at the University of Rochester demonstrated a new way, called chirped pulse amplification, to overcome these difficulties. The use of CPA technology was very successful because a table-top laser system with the CPA technology can deliver intensities 10^5-10^6 times higher than in the past. The invention of CPA was considered to be the most important progress in laser power during the last decades. It extends the horizon of laser physics from atomic and condensed-matter studies to relativistic plasma. It also opens up new physics such as relativistic optics, high-energy physics, non-linear wave breaking, and laser-driven particle acceleration physics.

The key point to ultra-high peak power and laser intensity is the amplification of ultrashort pulses on the picosecond and femtosecond time scales [14]. As we know, the saturation

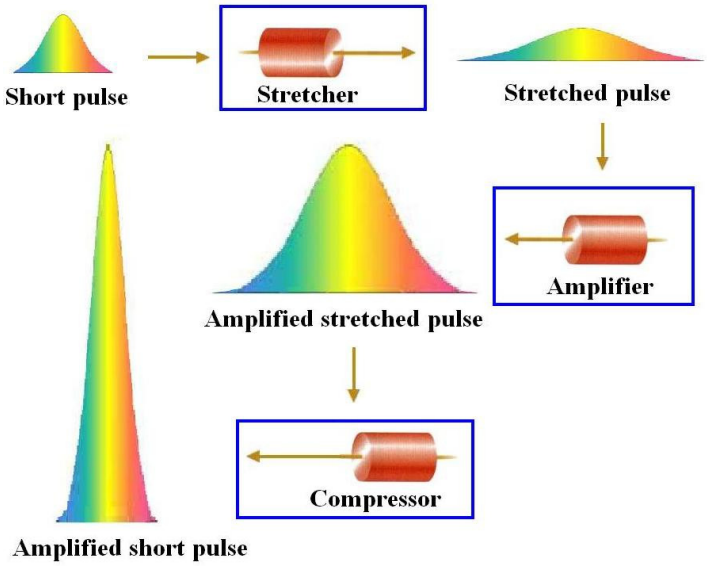

Figure 1.2: The conceptual layout of a CPA laser.

fluence of the amplifier media is given by

$$F_{sat} = \frac{\hbar\omega}{\sigma_\alpha}, \tag{1.1}$$

where $\hbar$ is Planck's constant, ω is the angular laser frequency, and σ_α is the amplifier transition cross section. A smaller transition cross section will benefit the compact laser system. However, it requires a beam with a large fluence, thousands times the limit value for destruction. Although the mode-locking technique reduced the laser pulse duration to femtosecond, such a short laser pulse can not be amplified because of non-linear effects as described above. This led to a stagnant period of laser power until 1985. The invention of CPA solves the problem perfectly. The concept of CPA is depicted in Fig. 1.2, which can be divided into three steps:

- A short laser pulse from an oscillator is first stretched in time several thousand times by passing through a stretcher, an optical dispersion system in which the original pulse undergoes linear frequency modulation. As a consequence, the output pulse is stretched out in space and chirped. Accordingly, the laser intensity lowers and becomes much smaller than that of the initial pulse.
- The stretched pulse has a sufficiently low intensity compared to the intensity limit of gigawatts per square centimeter which is safely introduced to the gain medium and amplified by a factor of 10^6-10^{12}. For example, a nanojoule pulse is amplified to energy in the mJ-J range.

- Finally, the amplified pulse is compressed by an inverted optical dispersion system which is a reverse process of the first step. The final pulse duration is almost same as the initial pulse but the peak power is boosted by a factor of several thousand times compared to its initial value.

As soon as the CPA concept was demonstrated at millijoule and joule levels in experiments, one expects that it could be extended to much higher energies to create a PW laser system. However, the pulse duration is limited by the gain narrowing because large gain will result in reduction of the laser system as it is amplified [14]. A new scheme, called optical parametric pulse amplification (OPCPA) was then proposed and soon demonstrated [34] in experiments. This new scheme was able to provide an extremely large bandwidth that could be pumped by large-scale laser systems. By using CPA or OPCPA technology, the laser peak power increased significantly in the last decades. The first petawatt pulse was demonstrated ten years ago [35] and several PW laser facilities such as Vulcan in Rutherford Appleton Laboratories, and OMEGA EP in University of Rochester, are operating. The Extreme Light Infrastructure (ELI) project with the aim to built a laser generating pulses with the peak power 0.2 exawatt ($0.2 \times 10^{18}\mathrm{W}$) is on the way and the preparatory stage of the project (2008-2011) will be completed this year [36]. Meanwhile, National Ignition Facility (NIF), the world's highest-energy laser system with 192 giant lasers was built in Lawrence Livermore National Laboratory and the first large-scale laser target experiments were performed in 2009 [37]. Besides, another international HiPER project to build first demonstration reactor for ICF is also scheduled, which uses much smaller lasers than conventional designs, yet produces fusion power outputs of about the same magnitude [38]. In Chapter 2, the light-sail regime for ion acceleration works in a typical laser intensity $10^{22}\mathrm{Wcm}^{-2}$ for a sub-micrometer foil target, which may be realized in the upcoming ELI and NIF laser systems in the next years.

1.2 Laser-driven particle acceleration

Since the invention of CPA, the laser intensity increased 5-6 orders of magnitude, up to $2.2 \times 10^{22}\mathrm{Wcm}^{-2}$ by focusing the beam on a spot with $\sim \mu\mathrm{m}$ radius, which suffices to ionize the foil target immediately and plasma is formed. Finally, the laser field interacts with the foil plasma directly, leading to a new branch of physics as mentioned above. Among these, relativistic laser-driven particle accelerators attract a lot of attention due to their compact size, low expenditure, and high accelerating gradient as compared to the conventional accelerators (TeV/m vs MeV/m). With the rapid development of laser technologies and foil engineering, it is believed that the laser-driven plasma-based ion accelerator should be used for several potential applications, e.g., medical therapy for cancer [39, 40, 41] and proton imaging, where

hundreds of MeV protons are required. This is approachable with current laser intensities and foils in the light-sail regime.

Let's consider particle (electron and proton) dynamic behavior in a relativistic electromagnetic field. It is well known that, in classical optics the amplitude of the light wave is small and electrons oscillate in the direction of the electric field at the light's frequency. In this case, there is no obvious displacement along the light's propagation direction and the electron-oscillation velocity is small compared to the speed of light. In relativistic optics, the amplitude of the light wave is much larger and the electrons can be accelerated close to the speed of light c transversely. Thus, the light's magnetic field becomes important compared to the electric field (noting the relationship $|\mathbf{B}| = |\mathbf{E}|/c$ in the motion equation $\mathbf{F}=q\mathbf{E}+q\mathbf{v}\times\mathbf{B}$). Under the combined action of the electric and magnetic fields, electrons are pushed forward significantly. For an electron in a plane wave of finite duration propagating along $\boldsymbol{x}$ direction, we can derive

$$\frac{p_x}{m_e c} = \frac{1}{2}a^2, \tag{1.2}$$

$$\frac{p_\perp}{m_e c} = a, \tag{1.3}$$

$$\frac{E_{kin}}{m_e c^2} = \gamma_e - 1 = \frac{1}{2}a^2, \tag{1.4}$$

where p_x ($p_\perp$) is the longitudinal (transverse) electron momentum, E_{kin} is the electron kinetic energy, and a is the dimensionless laser amplitude. As we can see, when $a = 1$, the kinetic energy of the electron oscillation in the light field is comparable to its rest energy $m_e c^2$. The light intensity at this point is

$$I\lambda^2 = \zeta \left[1.37 \times 10^{18} \mathrm{W}\mu\mathrm{m}^2\mathrm{cm}^{-2}\right] a^2, \tag{1.5}$$

where λ is the light wavelength, $\zeta = 1$ corresponds to linear polarization and $\zeta = 2$ for circular polarization. This kind of direct electron acceleration by the laser field is also referred to as ponderomotive acceleration of electrons. When the light wave is reflected by a steep overdense plasma surface, it leads to $\mathbf{J}\times\mathbf{B}$ heating of electrons [42, 43].

One alternative electron acceleration is in an indirect way by the laser wakefield (LWFA) proposed by Tajima and Dawson in Ref. [16]. The basic concept of LWFA can be divided into two steps [44]. At first, an intense laser pulse drives a plasma wave by the ponderomotive force, like a boat generates a wake on the sea. This plasma wave is accompanied by strong longitudinal electric fields and is co-moving with the laser pulse. At the second step, when electrons are injected at the peak of the wake, they can gain energy from the space-charge electric field of the plasma wave, similar to the way a surfer does from an ocean wave. In the linear regime where the laser intensity is not so high, this mechanism is, in principle,

capable of generating collimated electron bunches with narrow energy spread. There are several methods to excite the plasma wave for electron acceleration but we will not go into the details in this dissertation.

In the nonlinear regime, as the laser fields surpass a certain threshold, the plasma wave breaks and the so-called Bubble regime, proposed by Pukhov and Meyer-ter-Vehn [45], sets in. The Bubble exhibits strong electric fields pointing toward the bubble's center. Electrons are injected at the rear side of the bubble (wave-breaking) and can be accelerated for a long time to high energies. In this case, three-dimensional (3D) PIC simulations predicted the generation of GeV quasi-monoenergetic electron beams with a few percent energy spread [46]. In 2004, three groups reported experimental results of the electron acceleration in this non-linear regime independently [47, 48, 49]. Now, the Bubble regime is believed to be a unique efficient method to stably accelerate electrons in current experimental conditions. So far, 1 GeV electrons have been obtained in the linear regime by using a 3cm stack of discharged-produced low-density plasma [28, 50], and 1.45 GeV electron beam was achieved in the Bubble regime which should be the highest energy for laser acceleration systems [51].

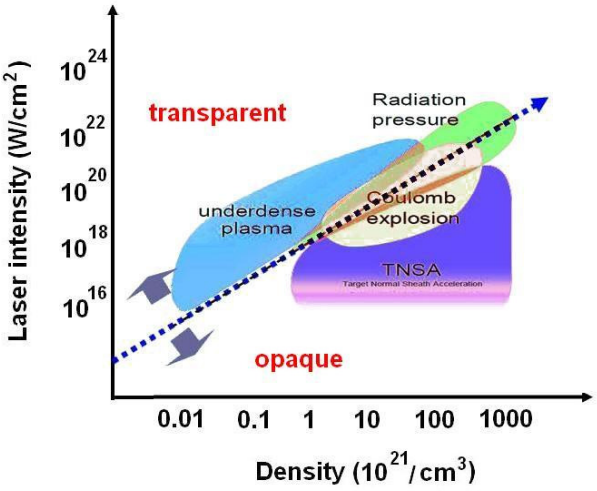

Figure 1.3: Ion acceleration mechanisms in laser-plasma interaction.

However, for ions it is very difficult to accelerate them directly by the laser field because of the larger ion mass. We can estimate the required laser intensity for direct proton acceleration in the following way. Assuming a relativistic proton oscillation in laser fields, the laser

intensity has to satisfy

$$I[\lambda = 1\mu\mathrm{m}] = \left(\frac{m_\mathrm{H}}{m_\mathrm{e}}\right)^2 I_0 = 4.6 \times 10^{24}\mathrm{Wcm}^{-2}, \tag{1.6}$$

$$a = \frac{m_\mathrm{H}}{m_\mathrm{e}} = 1836, \tag{1.7}$$

where $I_0 = 1.37 \times 10^{18}\mathrm{Wcm}^{-2}$ is the relativistic laser intensity. Obviously, the laser intensity above is far beyond the present laser technology though the new concept of OPCPA might make even these fantastic intensities technologically feasible in the future [34]. Direct proton acceleration is impractical in the current experimental condition and a new solution should be explored. In the last decades, several ion acceleration mechanisms have been proposed (see Fig. 1.3 [52]), such as TNSA, shock wave acceleration [53, 54, 55], Coulomb explosion [56], etc. As the first successful ion acceleration mechanism demonstrated in experiments [57], TNSA has been extensively studied in the last ten years since it was proposed by Wilks in Ref. [30]. TNSA is also the best understood laser-driven ion acceleration mechanism to date. Here we concentrate on the TNSA by reviewing the concept, theoretical model, scaling laws, recent progresses as well as its drawbacks in future applications.

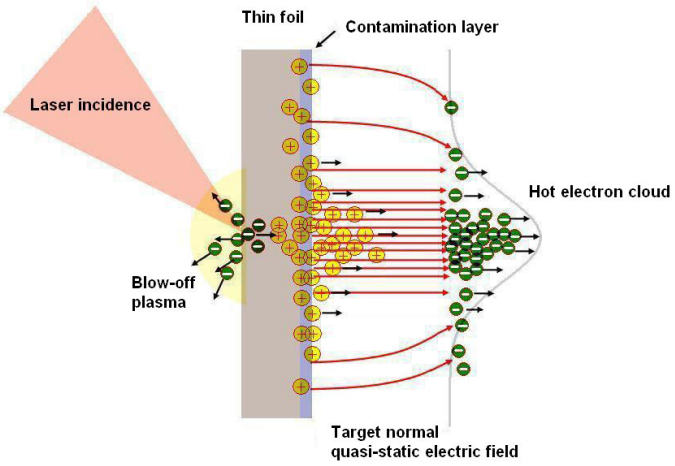

Figure 1.4: Schematic diagram of TNSA

1.3 Target normal sheath acceleration (TNSA)

The basic concept of TNSA is depicted in Fig. 1.4. A relativistic laser pulse irradiates a solid target with contamination at the rear side. The prepulse creates large plasma in front

of the solid target. Once the impinging main pulse hits the target, a cloud of hot electrons with energy $\sim 10\ \mathrm{MeV}$ is generated which extends past the ions on both the front and back of the target. The electrons pushed inside by the ponderomotive force pass through the foil and escape into the vacuum from the rear side, forming a hot electron cloud. To maintain quasineutrality in the plasma, quasi-static space-charge separation fields build up to prevent further loss of electrons, which, in essence, points normal to the target rear surface. The resulting potential difference is sufficient to accelerate the light protons from the contamination layer forward. Subsequent fast electrons travel through the target, experience these fields and are deflected back towards the target surface [58]. The accelerating field is as large as a few TeV/m, which is much larger than in radio-frequency (RF) accelerators (20 MeV/m), so that the protons and ions can be accelerated to MeV in distances of a few laser wavelengths.

At the front of the foil, the ions expand in space and the outermost ions are in a sphere. A similar but weaker accelerating field can be set up so that the ions are accelerated to much lower energies with a large emittance in space. Several models have been proposed to describe the dynamics in the TNSA [30, 59, 60, 61, 62]. In the following, we introduce the plasma expansion models (PEM) proposed by Mora that has been verified by several experiments [59].

At time $t = 0$, the plasma is assumed to occupy the half-space $x < 0$. The ions are cold and initially at rest. The electron density follows a Boltzmann distribution. Then we can derive from the Poisson equation

$$\varepsilon_0 \frac{\partial^2 \phi}{\partial x^2} = e(n_\mathrm{e} - Z n_i), \tag{1.8}$$

$$n_\mathrm{e} = n_{\mathrm{e}0} exp\left(\frac{e\phi}{k_B T_\mathrm{e}}\right), x \in (-\infty, \infty), \tag{1.9}$$

$$n_i = n_{i0}, x \in (-\infty, 0); n_i = 0, x \in (0, \infty), \tag{1.10}$$

$$n_{e0} = Z n_{i0}, \tag{1.11}$$

$$\phi(-\infty) = 0, \tag{1.12}$$

where n_{e0} and n_{i0} are the electron and ion density in the unperturbed plasma at $t = 0$, ϕ the electrostatic potential, T_e the electron temperature, Z is the ion charge number and k_B the Boltzmann constant. At $t > 0$, the ions start to move and electrons still follows the Boltzmann distribution. Therefore, the above equations are still valid but the ions are described by the equations of continuity and motion as

$$\left(\frac{\partial}{\partial t} + v_i \frac{\partial}{\partial x}\right) n_i = -n_i \frac{\partial v_i}{\partial x}, \tag{1.13}$$

$$\left(\frac{\partial}{\partial t} + v_i \frac{\partial}{\partial x}\right) v_i = \frac{Ze}{m_i}(-\nabla\phi) = -\frac{Ze}{m_i}\frac{\partial \phi}{\partial x}, \tag{1.14}$$

where v_i is the ion velocity. Accurate results can be obtained by assuming an isothermal expansion and introducing a self-similar expansion assuming quasineutrality in the expanding plasma. Finally, we obtain the maximal ion energy as follows

$$E_{max} = 2ZT_h \left[\mathrm{In}(\frac{\omega_{pi}t}{\sqrt{2e}} + \sqrt{1 + (\frac{\omega_{pi}t}{\sqrt{2e}})^2}) \right]^2, \tag{1.15}$$

$$\approx 2ZT_h \left[\mathrm{In}(\frac{2\omega_{pi}t}{\sqrt{2e}}) \right]^2, \tag{1.16}$$

$$T_h = m_e c^2 \left(\sqrt{1 + \frac{I_{\mathrm{Wcm^{-2}}}\lambda^2_{\mu\mathrm{m}}}{1.37 \times 10^{18}}} - 1 \right), \tag{1.17}$$

where $\omega_{pi} = \sqrt{n_{i0}Z^2e^2/m_i\varepsilon_0}$ is the ion plasma frequency and T_h is the temperature of hot electrons. As we can see, the final ion energy is dominated by the temperature and density of the hot electron population and hence scales as $(I\lambda^2)^{1/2}$. This model well interpreted the experimental results observed in early time [57, 63] and was verified by subsequent experiments and PIC simulations.

The TNSA has a number of characteristic advantages. In particular the generated beams are very bright ($\sim 10^{12}$ ions in ps pulse) with a low emittance ($\sim 0.005\pi$mm.mrd) and small source size ($\sim 100\mu$m), that is 10,000-fold improvement over conventional accelerator beams. Meanwhile, the acceleration is nearly instantaneous and there is no need of periodic lattices and long term stability condition. For CPA lasers with intensity $> 10^{19}\mathrm{Wcm}^{-2}$ and duration $< 1\mathrm{ps}$, studies show that the TNSA is a dominant ion acceleration mechanism [64].

In the past 10 years, the highest recorded proton energy remained 58 MeV on the Nova PW laser with 423J of laser energy. In order to enhance the energy gain, one can use different target geometries other than flat foils, such as reduced-mass targets [65, 66, 67, 68], stacked targets [69], cone targets [70, 71], or targets with various structures at the backside (e.g. rectangle, hemicycle, ellipse or concave) to enhance the coupling of the laser pulse with the particles [72, 73, 74, 75, 76, 77]. The energy conversion efficiency from the laser pulse to the protons can now be $10\% \sim 20\%$. Recently, the maximal cut-off energy of protons in TNSA has been reported as high as 67.5 MeV with more than 5×10^6 protons per MeV by using flat-top hollow microcone targets [78]. However, the ion energy usually shows a quasi-Maxwellian distribution over velocities with the mean energy of several MeV. In order to obtain a quasi-monoenergetic ion beam, it was proposed to make use of a heavy metal foil with a thin H-rich coating on the backside [17, 18]. In this case, the heavy ions stay at rest but the light ions are extensively accelerated. Finally, a quasi-monoenergetic proton beam with peak energy 1.2 ± 0.3 MeV and the spread $\sim 25\%$ was achieved in the experiment.

Despite of the relative success of the TNSA in several experiments, the beam quality of the generated protons and heavy ions are much lower than in the conventional accelerator, which is insufficient for further applications in practice, for example, in oncology, proton imaging and fast ignition [79]. Most applications mentioned above require high quality proton/ion beams, e.g., a beam with high particle energy and sufficiently small energy spread. Fig. 1.5 shows one example of potential applications of TNSA ion beams in brain tumor therapy, which demands a narrow energy spread to ensure that the ion energy is deposited over a small distance in the patient's tissue. For direct applications of ion beams in oncology, one requires protons with energy $E \sim 235 - 250$ MeV, spread $\Delta E/E \leq 1\%$, flux $N = 10^{12}$, dose 5×10^{10}pr/s or heavy carbon ions with energy $E \sim 120 - 400$ MeV/u, dose 4×10^{8}pr/s, so that one can use the Bragg-peak to treat a tumor close to a fragile and vital organ. When the protons reach the end of their paths in the body, the burst of energy released by protons is deposited mainly at the site of a tumor. In the concept of fast ignition with laser-driven ions, it is desirable to be able to control the ion energy spectrum as this may lead to a significant reduction in the proton beam energy required for ignition [79].

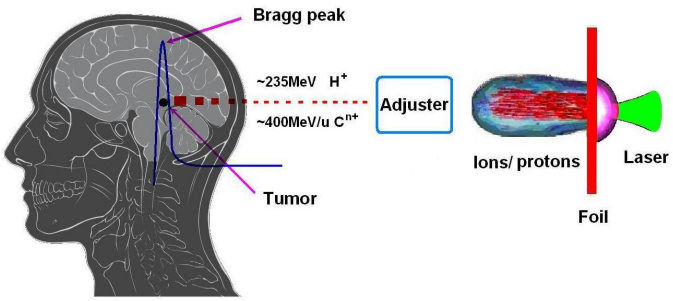

Figure 1.5: Concept map of brain tumor therapy with laser-driven ion beams.

However, in current TNSA experiments to date, the obtained maximum energy is only 67.5 MeV for protons and 10 MeV/u for heavy ions both with a quasi-thermal distribution [78]. The smallest energy spread obtained in recent experiments is about 17% with a low conversion efficiency $\sim 10\%$. Obviously, that is far away from the requirements of medical applications and a new ion acceleration scheme is required. With the rapid development of OPCPA technology, the state-of-the-art laser systems such as ELI and NIF make it possible to generate ultra-intense ultra-short ultra-clean (3U) laser pulse and the light-sail regime, to be discussed in the next chapter, might be a good candidate.

1.4 Conclusion

The motivation and main goal as well as the structure of this dissertation were described at the beginning of this chapter. For completeness, a short review of the CPA technology and the history of laser-driven particle acceleration were given to pave the way to better understanding of the work in the next chapters. Especially, TNSA was introduced in detail because it has been extensively studied in the past years. The characteristics and drawbacks of the TNSA were also enumerated to emphasize the importance and urgency of a new ion acceleration mechanism that can deliver high energy, low-emittance, small energy spread, and tunable proton and ion beams. Due to the higher energy conversion efficiency and uniform acceleration feature, the light-sail regime, to be discussed in the next chapter, might be an alternative.

Chapter 2

Ion acceleration in light-sail regime

The inefficiency, wide energy spread and low ion energy in TNSA probably come from the fact that the acceleration is only due to space-charge effects. The final energy of TNSA ions are dependent on hot electron population and temperature. Generally, linearly polarized laser pulses are favorable to generate plenty of hot electrons for TNSA because of the oscillation term in the ponderomotive force. However, these hot electrons follow an inhomogeneous distribution at the rear side of the foil so that it is relatively difficult to get a uniform space-charge field thus monoenergetic ion beams in TNSA.

Recently, with the rapid development of CPA and plasma mirror technology [80, 81], both the laser intensity (in excess of $10^{22}\mathrm{Wcm}^{-2}$) and the contrast ($\sim 10^{-12}$) have increased significantly. One of the most straightforward ion acceleration mechanisms, radiation pressure acceleration [13, 20, 21, 64] (RPA) or laser piston [20] or light-sail regime [21], is being re-visited. The basic concept came from the proposal of interstellar vehicle propelled by terrestrial laser beam by Marx in 1966 [82]. The laser propulsion from the earth or solar light might provide a unique and unlimited impetus for the spacecraft. Esirkepov *et. al.*, introduced the concept to the efficient ion acceleration in ultra-intense laser-foil interaction [20]. Later, Macchi *et. al.*, proposed to make use of circularly polarized laser pulses to suppress the undesirable electron heating and reduce the laser intensity required for the light-sail regime [83]. Subsequently, Zhang *et. al.* and Yan *et. al.* observed the proton "spiral structure" in phase space by using circularly polarized laser pulses [84, 85, 86]. Since then, the light-sail regime became a very active domain in laser-driven ion acceleration physics. Many studies contributed to further improving the beam quality, tunability and conversion efficiency in the following years [21, 22, 23, 55, 64, 87, 88, 89, 90, 91, 92, 93, 94, 95]. The first experimental demonstration of radiation pressure acceleration of thin foils has also been claimed in Max-

Planck-Institut (Garching) recently [96].

In the following, we derive accurate expressions of the ion energy, velocity and momentum from a simple "flying plasma mirror" model in the light-sail regime. 1D simulations are performed to demonstrate the feasibility of the model. It is shown that the simulations are in excellent agreement with the model predictions. However, when we extend the model to multi-dimensional cases, several issues arise, such as the foil target deformation and Rayleigh-Taylor-like instability. These multidimensional effects finally destroy the acceleration structure and result in a broad energy spectrum though it has a promising energy conversion efficiency.

2.1 "Flying plasma mirror" model and scaling laws

When an ultra-intense laser pulse irradiates an ultra-thin over-dense foil, the foil can be regarded as a plasma mirror. Most of the laser energy is transferred to the foil with only a small part carried away by the reflected laser pulse. Fig. 2.1 shows the schematic diagram of laser-foil interaction in the light-sail regime. Assuming the frequency of the incident and reflected laser pulse to be ω and ω_1, respectively, we have $\omega_1/\omega = (1-\beta)/(1+\beta) \simeq 1/4\gamma^2$ as a result of the red-shift, where β is the foil velocity normalized by the speed of light c and γ is the relativistic factor. As the foil is accelerated to near the speed of light, the laser energy is efficiently converted to the kinetic energy of the foil with the energy conversion efficiency $\eta = 2\beta/(1+\beta) \simeq 1 - 1/4\gamma^2 \approx 1$. Considering a flat foil irradiated by a plane laser wave, the whole foil is uniformly accelerated forward. This holds the promise of generating high energy monoenergetic ion beams.

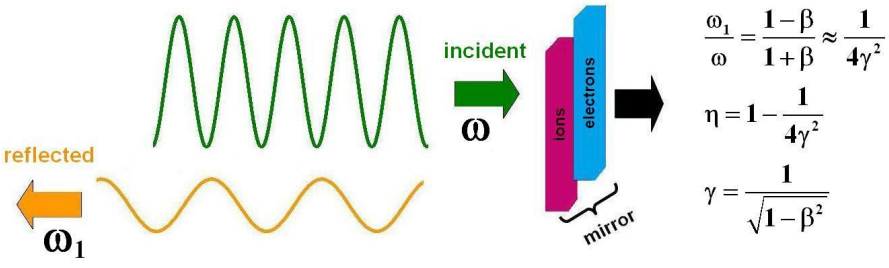

Figure 2.1: Schematic diagram of laser-foil interaction in the light-sail regime.

We begin with the basic equation of the foil motion. Assuming an element of area $d\sigma$ of a perfectly reflecting mirror, the motion equation can be written in the laboratory reference

frame (LF) as

$$\frac{d\mathbf{p}}{dt} = \mathcal{P} d\sigma, \tag{2.1}$$

where **p** is the momentum of the mirror element, d$\boldsymbol{\sigma}$ is a vector normal to the foil, and $\mathcal{P}$ is the radiation pressure. Assuming the relative amplitudes of reflected and transmitted waves being ζ and ϱ in the rest frame of the foil, we have $|\zeta|^2 + |\varrho|^2 = 1$ because of energy conservation. The radiation pressure can thus be written as

$$\mathcal{P} = \frac{{E_M}^2}{4\pi}(1 + |\zeta|^2 - |\varrho|^2), \tag{2.2}$$

$$= \frac{E^2}{2\pi}(\frac{\omega_M}{\omega})^2 |\zeta|^2, \tag{2.3}$$

where $E_M = E(\omega_M/\omega)$ and $\omega_M = \omega\sqrt{(1-\beta)/(1+\beta)}$ are the laser electric field and frequency as witnessed in the moving reference frame (MF). For a perfect flying mirror, $|\zeta|^2 = 1$ and we get

$$\mathcal{P} = \frac{E^2}{2\pi}\frac{1-\beta}{1+\beta}, \tag{2.4}$$

According to the particle conservation, we finally get the equation of the foil motion as

$$\frac{dp}{dt} = \frac{E^2}{2\pi n_i l}\frac{\sqrt{p^2 + m_i^2 c^2} - p}{\sqrt{p^2 + m_i^2 c^2} + p}, \tag{2.5}$$

$$p = \gamma m_i v_i, \tag{2.6}$$

where v_i, m_i, n_i, and l are the ion velocity, ion mass, ion density, and foil thickness, respectively. The equation describes the ion dynamics in a perfect flying mirror model. Further, we can get simplified form of the motion equation and the velocity evolution as following

$$\rho\frac{d(\gamma\beta)}{dt} = \frac{E^2}{2\pi c}\frac{1-\beta}{1+\beta}, \tag{2.7}$$

$$\frac{d\beta}{dt} = \frac{E^2}{2\pi m_i n_i l c}\frac{1}{\gamma^3}\frac{1-\beta}{1+\beta}, \tag{2.8}$$

where $\rho = \sum_i m_i n_i l$ is the target area mass density. Obviously, the foil dynamics is defined only by the area mass density ρ and the laser electric field E, which is quite different from the collisionless shock wave acceleration in Ref. [54, 55]. These equations also imply the possibilities of improving the foil acceleration by modifying the foil geometry, i.e., l, n_i, or the laser electric field profile E. We will discuss those in Chapter 3 and 4.

Eq. (2.8) is a highly nonlinear equation and it is impossible to get solutions by directly integration. We can use hyperbolic functions by defining $\beta = \tanh\theta$. Then, a very compact form of the parameters is given, such as $\gamma = \cosh\theta$ and $\gamma\beta = p = \sinh\theta$. The Eq. (2.8) can be rewritten as

$$(\cosh\theta + \sinh\theta)^2 d(\sinh\theta) = A dt, \tag{2.9}$$

$$A = \frac{{E_L}^2}{2\pi c\rho}, \tag{2.10}$$

Noting $\sqrt{1+u}du = (2/3)d(1+u)^{3/2}$ and considering the initial condition $\beta_{t=0} \sim 0$, we obtain

$$p + \frac{2}{3}p^3 + \frac{2}{3}\gamma^3 = At + \frac{2}{3}, \tag{2.11}$$

Eq. (2.11) describes the correlation between the ion momentum and ion energy in the light-sail regime. For $p \ll 1$ or $\beta \ll \sqrt{2}/2$, $p \approx At$. As the target approaches the speed of light ($\beta \to 1$), $p \approx (3/4)At^{1/3}$. This indicates that the ion energy initially increases at a rate of $(It/\rho)^2$, but slows to $(It/\rho)^{1/3}$ later. Further, we can obtain the exact solution of Eq. (2.1) as

$$\beta = 1 - [\varsigma(t) + \varkappa(t)]^{\frac{1}{3}} - [\varsigma(t) - \varkappa(t)]^{\frac{1}{3}}, \tag{2.12}$$

$$\gamma - 1 = \frac{[\xi(t) - 1]^2}{2\xi(t)}, \tag{2.13}$$

where $\varsigma(t) = 1/[1 + h(t)^2]$, $\varkappa(t) = h(t)/[1 + h(t)^2]^{3/2}$, $\xi(t) = \sqrt{(1+\beta)/(1-\beta)}$, and $h(t) = 3At + 2$. Eq. (2.12) is based on the assumption that the foil remains intact during the acceleration and both ion species and electrons are accelerated to the same velocities. Fig. 2.2 shows one example of the scaling laws for parameters $m_i = 1836m_e$, $n_i = 320n_c$, $l = 0.1\mu\mathrm{m}$ and $a = 100$, where $n_c = m_e\omega/4\pi e^2$ is the critical density. As we can see, the ion energy increases linearly very fast at the beginning, scaling as $\sim t$, and becomes slow gradually, scaling as $\sim t^{1/3}$. By contrast, in TNSA the final energy is scaled as $\sim \mathrm{In}^2(t)$ which is much lower than in the light-sail regime.

By using this perfect flying mirror model, we can predict the final ion energy, velocity and momentum. However, here we assumed a complete reflection of the electromagnetic wave and take no account of multi-dimensional effects, e.g., transverse instabilities. Though the model predicts a promising energy scaling, it can not be applied directly in 2D and 3D cases.

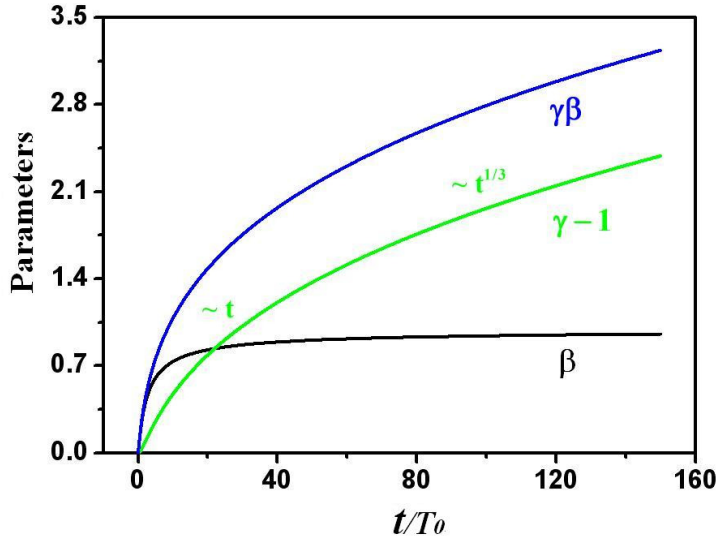

Figure 2.2: Scaling laws of the ion energy, momentum and velocity in the light-sail regime.

2.2 Pre-hole-boring and minimal target thickness

In this section, we first study, in detail, the electron and ion dynamics during the laser impinging the solid foil. At the first stage of the light-sail regime, electrons will be accelerated and piled up by the laser pressure and later ions will be accelerated by the charge separation field. We call this process pre-hole-boring since during this time ions have not catched up with the compressed electron layers (CEL), and the hole boring process has not yet reached its stationary stage. For convenience, we use normalized variables here. The intensity of the laser electric field is normalized as $a = eE/m\omega c$, spatial coordinate and time are normalized by laser wavelength λ and period $T_0 = 2\pi/\omega$, respectively. The velocity, mass, density are normalized by the speed of light in vacuum c, electron mass m_e and critical density n_c, respectively.

If we only consider the ponderomotive force of laser pulse acting on plasma electrons (light pressure), the dynamics of the CEL is governed by the equations as following

$$n_0 l_1 \frac{d\gamma\beta}{dt} + n_0\gamma\beta\frac{dl_1}{dt} = \frac{a_0^2(t)}{\pi}\frac{1-\beta}{1+\beta} - \pi n_0^2 l_1(l_1 + l_e), \tag{2.14}$$

$$\frac{dl_1}{dt} = \beta, \tag{2.15}$$

where β is the normalized velocity of the CEL, γ is the relativistic factor, l_1 is the displacement

of the CEL, n_0 is the initial plasma density, $a_0(t)$ is the amplitude of the laser electric field and l_e is the thickness of the CEL. In the first equation, the second term on the left side comes from the mass increase of the CEL. The first one on the right side is the contribution of the laser pressure and the second one is from the field of charge separation. For the ions, we solve the following hydrodynamical equations

$$\frac{\partial n}{\partial t} + \frac{\partial (n\beta_i)}{\partial x} = 0, \tag{2.16}$$

$$\frac{\partial \beta_i}{\partial t} + \beta_i \frac{\partial \beta_i}{\partial x} = \frac{2\pi}{m_i} E_x, \tag{2.17}$$

$$\frac{\partial E_x}{\partial x} = 2\pi(n - n_e), \tag{2.18}$$

where n is the ion fluid density, β_i is its velocity, m_i is the ion mass and E_x is the space-charge separation field. The density distribution of electrons (n_e) is calculated from the evolution of the CEL. We simply assume that electrons from the front target are piled up, compressed and uniformly distributed within a region with the size of l_e. It is true because the CEL is always in front of the accelerated ions at this early stage. This assumption will become invalid as soon as the ions catch up with the CEL. Our calculation ends before the time and ensures that the hydrodynamic velocity of the ions at the density peak point is larger than the CEL velocity. The moving distance of the CEL at this time equals the minimum thickness of the target for ion acceleration (l_{hydro}). As we will see, this usually gives a smaller value than the one ($l_{immo} = a/\pi n$) obtained in the immobile ion model [97].

The thickness of the CEL (l_e) is a variable that is difficult to derive. In a simple model, one usually assumes that it equals the skin length [86]. However, from PIC simulations we see that the real thickness is far less than the skin length. We improve this by considering the relativistic motion of the CEL. It corresponds to the skin length of a moving plasma $l_s = l_{s0}\sqrt{p_\perp/\gamma_x}$ where $l_{s0} = c/\omega_p$ is the normal non-relativistic skin length, $p_\perp$ is the normalized transverse momentum of the electrons in the CEL and $\gamma_x = 1/\sqrt{1-\beta_x^2}$ with β_x the longitudinal velocity of the CEL.

We solve the system of equations above numerically. In our calculations, we vary the ion mass, target density and laser intensity to evaluate their effects on the minimum target thickness. The foil is assumed to be thick enough initially ($0.2\lambda < x < 1.8\lambda$) so that ions can catch up with the CEL. The density distributions of the electrons and ions when the calculation ends are shown in Fig. 2.3(a). The density distributions also indicate one of the necessary criteria to end our calculation: the time (t_{end}) when the peak of the ion density distribution reaches the CEL. After $t = t_{end}$, the charge separation field for CEL will obviously deviate from the one used in Eq. (2.14). The moving distance of the CEL at this time (t_{end}) is assumed to be the minimum thickness of the target l_{hydro} since the ions can catch up with the CEL once

the target is thicker than l_{hydro}. Obviously we can obtain l_{hydro} from the numerical calculations as shown in Fig. 2.3(a). It can also be obtained from the force balance as we will show in the following.

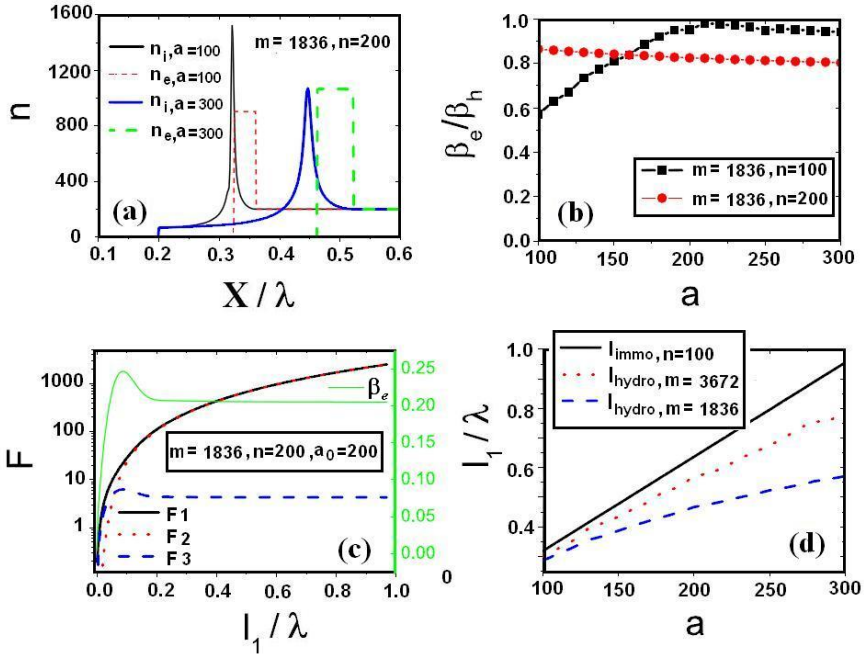

Figure 2.3: Analytical results for the pre-hole-boring process. (a) Density distribution of electrons and ions at the end of numerical calculation. (b) Dependence of final velocity of the CEL on laser intensity and target density. (c) Evolution of CEL velocity and forces on the CEL along with CEL displacement (l_1). (d) CEL displacements for different ion masses and laser intensities.

Fig. 2.3(b) shows the ratio of the CEL velocity (β_e) at the end of the calculation to the theoretical relativistic hole boring velocity $\beta_h = a/(a + \sqrt{m_i n_0})$ [98]. As we see, the value tends to a constant. Having this constant value, it is then easy to calculate the displacement of the CEL at t_{end} from the relationship of the balance between the charge separation force and the laser pressure:

$$\pi n_0^2 l_1 (l_1 + l_e) = \frac{a_0^2}{\pi} \frac{1 - \beta_e}{1 + \beta_e}, \tag{2.19}$$

The force balance can be seen from Fig. 2.3(c). The black line indicates the force due to the laser pressure (F_1), the red dotted line indicates the charge separation force (F_2) and the blue dashed line indicates the force due to the mass increase (F_3). The first two forces balance each other very quickly once the CEL moves 0.1λ into the target. The displacements of the CEL obtained in Fig. 2.3(a) fit well with those from the force balance calculation. The former is shown in Fig. 2.3(d) for different ion mass. The value based on the immobile ions model

(l_{immo}) is also shown in the figure marked by the black line. As we can see, when the intensity of the laser electric field is larger than $a_0 = 100$, the present results l_{hydro} are smaller than l_{immo}. The lighter the ion mass, the larger the difference with the one of the immobile ion model. l_{hydro} is just the minimum thickness of the foil target for ion acceleration. When the target is thinner than this minimum value, ions cannot catch up with the electrons and neutralize them. Then electrons are smashed away from the ions completely by the light pressure and the target is transparent to the laser thereafter. The electrons are dispersed by the laser pulse and the naked protons experience Coulomb explosion. The stable RPA acceleration structure thus disappears.

From the present calculation, we see that ions have already caught up with the electrons before the CEL moves a distance of l_{immo} and the CEL will not completely separate from the ions. So our model shows that the usual value l_{immo} overestimates the minimum thickness. This finding is important for the selection of the target thickness for the multicascade ion acceleration scheme proposed by Gonoskov *et. al.* [99].

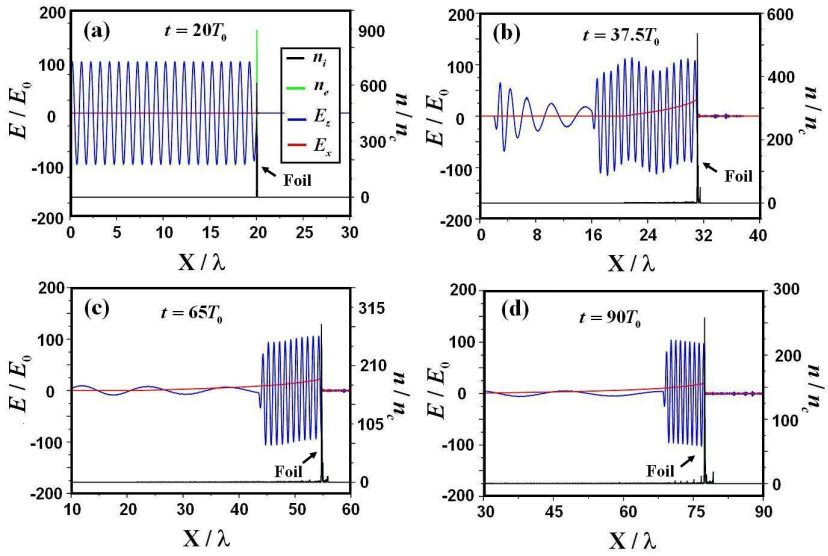

Figure 2.4: Snapshots of laser-foil interaction by using a circularly polarized laser pulse in 1D simulations at (a) $t = 20T_0$, (b) $37.5T_0$, (c) $65T_0$ and (d) $90T_0$.

2.3 1D simulation results

For comparison, we first carry out a series of 1D simulations to investigate the detailed acceleration process by using the fully electromagnetic relativistic PIC code VLPL [100]. In

the 1D case, the longitudinal length of the simulation box is $x = 100\lambda$ with 2×10^4 cells so that the expected density spike can be resolved. For simplicity, we take the laser wavelength as $\lambda = 1.0\mu\mathrm{m}$. Each cell contains about 1000 numerical macro-particles because of the solid density. The target is 0.1λ long, located at $x = 20\lambda$ and composed of fully ionized protons and electrons with the number density $320n_c$ (the critical density $n_c \sim 1.1 \times 10^{21}/\mathrm{cm}^3$ for $\lambda = 1.0\mu\mathrm{m}$ laser). We first consider a circularly polarized laser pulse that is incident from the left boundary at $t = 0$. The laser intensity follows a trapezoidal profile (linear growth - plateau - linear decrease) in time. The dimensionless laser amplitude is $a_0 = 100$ and the duration is $\tau_L = 22T_0$ ($\sim 73.3\mathrm{fs}, 1T_0 - 20T_0 - 1T_0$). Absorbing boundary conditions are applied to both the fields and particles.

Fig. 2.4 shows the detailed acceleration process. Here, we choose the optimal foil thickness according to the transparency threshold $a_0 = \pi n_e l$ [97]. As we can see in Fig. 2.4(b), when the laser pulse irradiates the foil, it is reflected by the foil immediately and the foil is simultaneously accelerated forward by the strong laser radiation. The foil acceleration depends on the efficient momentum transfer from the laser photons to the ions. At the very beginning, the foil velocity v_i is very small and the wavelength of the reflected wave is almost same as the incident wave. As times goes on, the wavelength increases gradually and scales well as $(1 + \beta)/(1 - \beta)$ where β is the foil velocity normalized by the speed of light. At the final stage, the wavelength of the reflected laser pulse is about 30λ which indicates a relativistic factor $\gamma_i = 3$. This estimation agrees well with the energy spectrum as displayed in Fig. 2.5 (d).

There are several key points we have to clarify in the 1D simulations. First, we observe a strong longitudinal electric field E_x as large as $10^{14}\mathrm{V/m}$, which is the same order of magnitude of the laser electric field. In other words, the plasma foil works like a rectifier to convert the transverse laser field to a strong longitudinal accelerating field. As we know, the laser transverse field is periodic and has no capability to accelerate any ions directly. The self-forming accelerating field in our case results from the space-charge separation. Once the ponderomotive force of the incident laser pulse acts on the foil, electrons are pulled out immediately. These electrons separate from the immobile ions (within the time of electrons' separation), forming a strong space-charge field that can thus accelerate ions forward. Such a separation is determined by the balance between the laser radiation pressure and electrostatic potential. Fig. 2.5(a) shows the acceleration field E_x and the protons/electrons position at $t = 40T_0$. Obviously, both protons and electrons move together at almost the same velocity so that an intact foil structure can be kept, which is crucial for a stable ion acceleration structure in the light-sail regime. Most protons are located in the decreasing phase of field E_x, resulting in a well-organized "spiral structure" in phase space as shown in Fig. 2.5(b).

The ion acceleration in this way is also referred to as "phase-stable" acceleration [86]. As

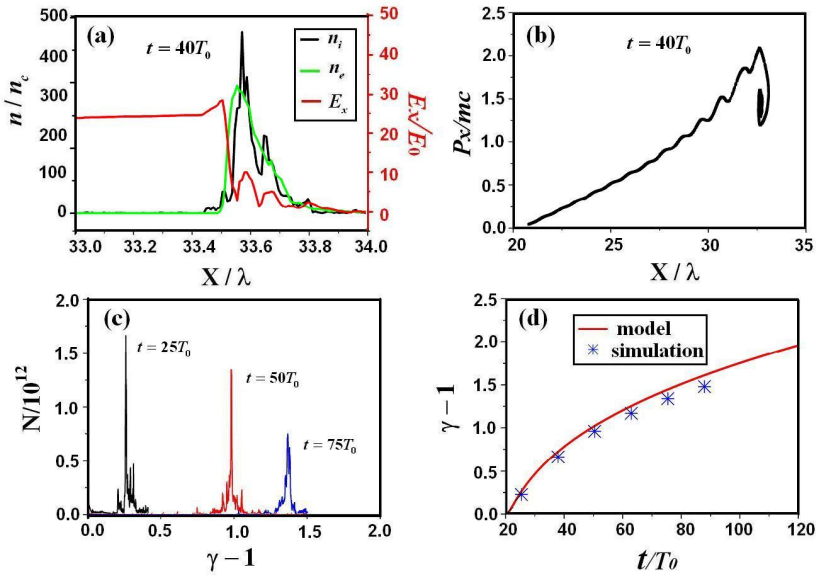

Figure 2.5: (a) Acceleration field E_x and particles position at $t = 40T_0$. (b) Proton phase space distribution at $t = 40T_0$. (c) Proton energy spectrum evolution. (d) Comparison of the averaged proton energies from 1D model and 1D simulations.

expected, we obtain a monoenergetic proton beam with a pronouncing peak in the energy spectrum as plotted in Fig. 2.5(c). The final proton energy is as high as 2 GeV with a few percent energy spread. For comparison, Fig. 2.5(d) presents the averaged proton energy and the analytical predictions from Eq. (2.13). Obviously, the simulation results are in excellent agreement with the model predictions, which well demonstrates the validation of the 1D model discussed above.

Another point to be emphasized is the requirement for the laser polarization in the light-sail regime. Here, it is shown that circular polarization of the laser pulse is an essential requirement for monoenergetic proton beam generation. By contrast, we also show the simulation results by using a linearly polarized lase pulse. In this case, the dimensionless laser amplitude $a_0 = 141.4$ so that both cases have the same laser intensity. Fig. 2.6 exhibits the acceleration process that is quite different from the circularly polarized case as displayed in Fig. 2.4. First, we don't observe a strong space-charge separation field E_x in this case. This implies that the laser ponderomotive force potential dominates the acceleration and the balance between the radiation pressure and the electrostatic potential is broken. The laser pulse penetrates the foil and propagates into the vacuum behind the foil since a very early time, e.g., $t = 35T_0$. We attribute it to the strong electron heating as shown in Fig. 2.7(a). A comb structure is observed in the electron phase space. This is a typical feature of "$\mathbf{J} \times \mathbf{B}$" heating as we discussed in Chapter 1 [42, 43]. As regards the physical reason of differences between the two cases, we

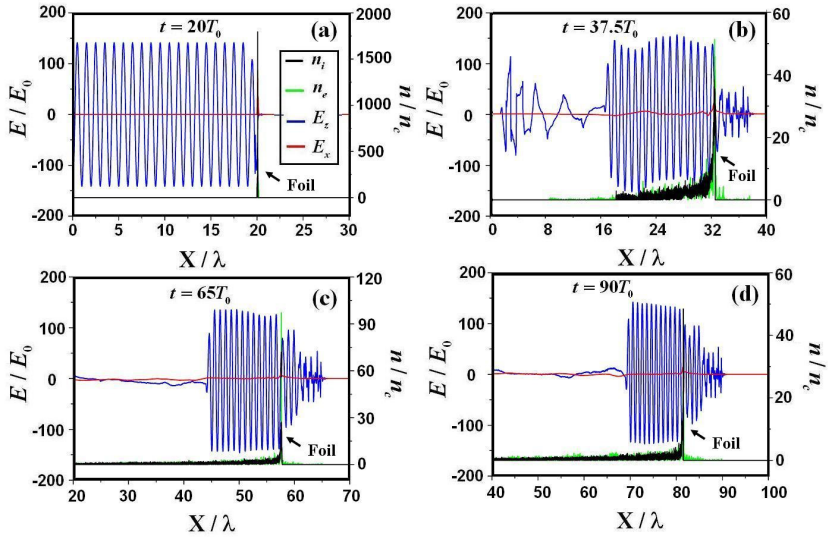

Figure 2.6: Snapshots of laser-foil interaction by using a linearly polarized laser pulse in 1D simulations at (a) $t = 20T_0$, (b) $37.5T_0$, (c) $65T_0$, and (d) $90T_0$.

have to trace back to the original ponderomotive force expressions as shown below,

$$f_p^L = \frac{e^2}{4\gamma_e m_e \omega^2}\frac{\partial}{\partial z}E^2(z)[1+\cos(2\omega t)], \tag{2.20}$$

$$f_p^C = \frac{e^2}{4\gamma_e m_e \omega^2}\frac{\partial}{\partial z}E^2(z), \tag{2.21}$$

where $E(z)$ is the laser electric field component. For a linearly polarized laser pulse, the ponderomotive force f_p^L has an oscillating term, which can excite a strong oscillation of electrons. As a consequence, much more hot electrons are produced, which is essential for the TNSA mechanism but undesirable in the light-sail regime because strong electron heating results in the destruction of the stable acceleration structure. As shown in Fig. 2.7(b), we see a normal phase space distribution of protons instead of a "spiral structure". Eventually, a widely broad energy spectrum is observed in this case (not shown here). However, for a circularly polarized laser pulse, the ponderomotive force has no such an oscillating term, but only the time average or zero-frequency component [83]. The strong force directly pushes the electrons inwards the target and a strong electric field is formed behind the laser front [91]. The whole foil can keep a well-organized intact structure for a long time until the laser-foil interaction ends (see Fig. 2.5(c)).

The last point worthy to be mentioned is the high energies of the protons in the light-sail regime. According to the simulations above, the proton energy increases linearly at the first stage and then slows to $(It)^{1/3}$. Obviously, at the second stage the rate of energy increase

is much slower so that it is difficult to get a much higher energy. In current experimental conditions with the laser intensity $10^{18} - 10^{20}\mathrm{Wcm}^{-2}$ and $10nm$ foil, the light-sail regime is a very good candidate for producing a few GeV proton beams. This is very attractive for future applications ranging from medical therapy, proton imaging to fast ignition for ICF.

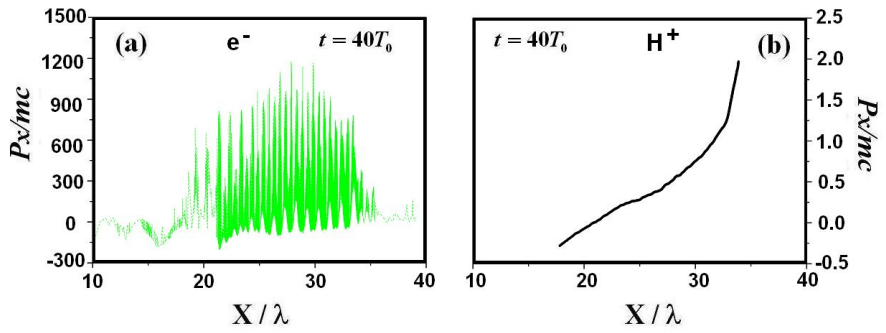

Figure 2.7: (a) Electron phase space distribution at $t = 40T_0$. A strong electron heating, e.g., **J** $\times$ **B** heating occurs. (b) Proton phase space distribution at $t = 40T_0$. A "spiral structure" observed in the circularly polarized laser case is absent.

2.4 Multi-dimensional effects

In the 2D case, the simulation box is $X \times Y = 32\lambda \times 32\lambda$, sampled by 6400×3200 cells with each cell 800 macro-particles. The time step is $\triangle t = 0.004T_0$. Here, we consider a transversely Gaussian laser pulse. At $t = 0$, a circularly polarized Gaussian laser pulse is incident from the left boundary and focuses on the left side of the solid foil. The laser intensity follows a trapezoidal profile in time with duration $\tau_L = 14T_0$ ($1T_0 - 12T_0 - 1T_0$), top intensity $a_0 = 100$, and focal radius $\sigma_L = 6\lambda$. The foil size is $0.1\lambda \times 32\lambda$, located at $x = 10\lambda$ and composed of fully ionized protons and electrons with the number density $320n_c$. Absorbing boundary conditions are applied to fields and periodic boundary conditions are applied to particles.

Fig. 2.8 shows the 2D simulation results. Obviously, it exhibits a totally different ion acceleration process from the 1D cases above. First, the foil is tremendously deformed soon after the laser irradiates the left side of the foil target. This modulation is induced by the Gaussian profile of the incident laser pulse. In fact, we can understand it from the basic foil motion equation Eq. (2.8) where the foil motion depends on the ratio $E_L^2/m_i n_e l$. For a flat foil and Gaussian laser pulse $E_L \sim E_0 exp(-r^2/\sigma_L^2)$, the foil acceleration is definitely inhomogeneous along the transverse direction and the foil deformation occurs at the very beginning

of the laser-foil interaction. Obviously, this deformation is undesirable that results in several problems, e.g., electron heating and surface instability. As we can see from Fig. 2.8(g), the electron energy spectrum shows a thermal distribution with a high cutoff energy $\sim$ GeV. As we know, in TNSA hot electrons are expected to enhance the energy conversion from the laser pulse to the electrons and thus ions through space-charge separation field. In the light-sail regime, one of the initial purposes to make use of circularly polarized laser pulses is to suppress the generation of these hot electrons.

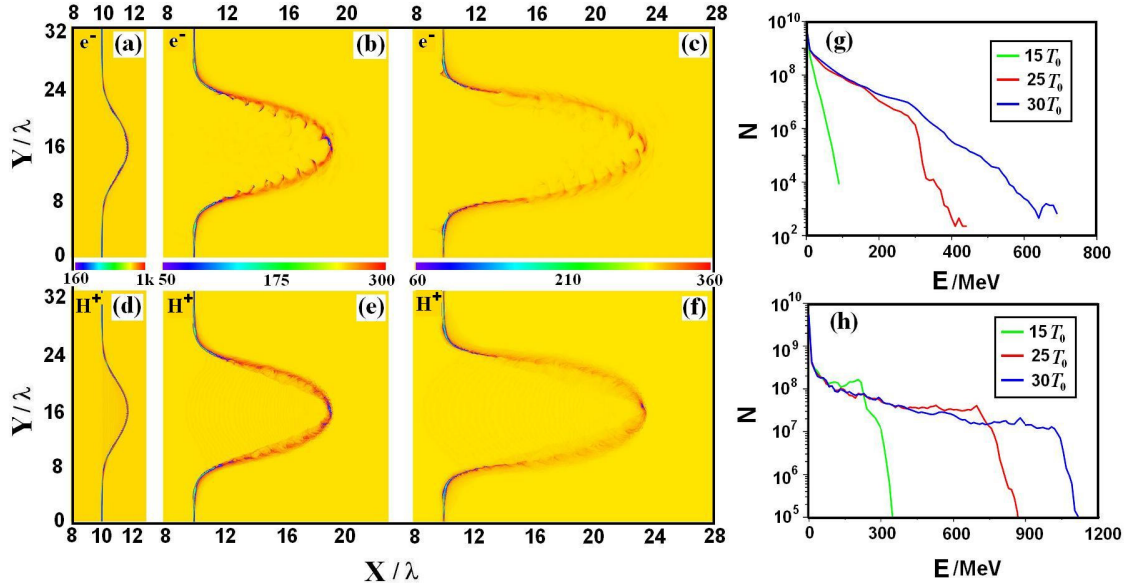

Figure 2.8: Snapshots of laser-foil interaction by using a circularly polarized laser pulse in 2D simulations at (a,d) $t = 15T_0$, (b,e) $25T_0$, and (c,f) $65T_0$. (g) and (h) show the electron and ion energy spectra at these time points.

Second, we observe serious transverse instabilities as displayed in Fig. 2.8(b,e). The characteristic of these instabilities is a clear surface sawtooth-like structure (or "clump" [13]). By additional simulations with a higher resolution [101], we find that the initial spacing of the surface rippling at the foil top and bottom side approximately equals laser wavelength λ. At the center of the foil, the spacing is about $(1/2)\lambda$. Swiftly, the instabilities propagate from the top and bottom to the center and the spacing along the whole transverse direction becomes $(1/2)\lambda$. Finally, the light wave penetrates the foil through the rippling structure and the initial intact structure of the foil is destroyed. In previous studies [13, 101], we referred this instability as Rayleigh-Taylor-like (RT) instability because this surface rippling seems like the conventional Rayleigh-Taylor instability occurring in ICF [19]. In the light-sail regime, we can consider laser photons a "light fluid" and the plasma a "heavy fluid". When the laser irradiates the foil and pushes the foil forward, so-called Rayleigh-Taylor instability takes place and surface rippling occurs. Of course, the underlying physics is much more complicated,

which involves several other factors such as the plasma density, the laser intensity and the foil thickness, etc. We will talk about this in Chapter 5.

Overall, the foil target deformation and transverse instability lead to the final destruction of the intact acceleration structure observed in the 1D simulations. Fig. 2.8(h) shows the proton energy spectrum. It exhibits a quasi-thermal distribution with a sharp cutoff. There is not any monoenergetic peak observed both at the beginning and at a later time. Though the cutoff energy is as high as GeV, it is impractical to be used in real applications because of the broad energy spectrum. Previous studies showed that a properly tailored laser pulse with a sharp intensity rise might stabilize the foil acceleration [13]. However, the transverse instability is still unavoidable though its growth gate is smaller. To solve these problems, we propose some schemes, such as using a shaped foil target or a density modulated foil target to overcome the foil target deformation, using a two-ion-species shaped foil target to suppress the RT-like instabilities. In the next chapters, we will treat these issues in detail.

2.5 Conclusion

As a promising and efficient ion acceleration mechanism, the light-sail regime has been re-visited these years with the rapid development of laser technologies. Based on the "flying mirror model", we derive the basic expressions of the foil velocity, ion momentum and ion energy. The validation of the model and the relevant scaling laws have been well demonstrated by a series of 1D PIC simulations. However, several issues take place when we extend the model to multi-seminal cases such as the foil target deformation and transverse instabilities. These multi-dimensional effects should be carefully attended for better understanding a real experiment.

Here, we would like to emphasize two points. First, in most laboratories the laser system can only deliver laser beams with peak intensity $10^{18} - 10^{20}\mathrm{Wcm}^{-2}$ with a tight focal size. In this case, the light-sail regime is also approachable. According to the optimal ion acceleration condition $a_0 = \pi n_e l$ in the light-sail regime, we may reduce the foil thickness to a few nanometers so that the light-sail regime takes place in lower laser intensities. For example, for a $10^{19}\mathrm{Wcm}^{-2}$ laser, the solid foil density is about hundreds critical density and the foil thickness should be 10nm (for $\lambda = 1\mu\mathrm{m}$ laser). This ultra-thin foil is available in laboratories. In fact, the first experiment on RPA in Garching employed a Diamondlike carbon (DLC) foils with thickness only 2.9-40nm. The laser pulse was normally incident on the foil with a moderate intensity ($5 \times 10^{19}\mathrm{Wcm}^{-2}$) [96]. An alternative method is to use a infrared CO_2 laser with a larger wavelength, e.g., $\lambda = 10\mu\mathrm{m}$. In this case, the laser intensity required for RPA

is also reduced significantly [102]. Second, the light-sail regime requires a very high laser contrast ($> 10^{-10}$), so that the main laser pulse interacts directly with the foil. Otherwise, a strong electron heating occurs and the acceleration structure shall be destroyed. In fact, by using double plasma mirrors [80], it is shown that the laser contrast can be increased up to 10^{-12}, which is sufficient for avoidance of the pre-plasma.

Chapter 3

Uniform ion acceleration in Shaped Foil Targets

When a transversely Gaussian laser pulse irradiates a flat foil, the foil is soon distorted that results in strong electron heating and thus a broad ion energy spectrum. In this chapter, a scheme is proposed to avoid the foil target deformation. A so-called shaped foil target (SFT) is suggested to realize a uniform foil acceleration, in which it is shown by multi-dimensional PIC simulations that, the ion acceleration structure can be maintained for a longer time as compared to a normal flat target. The final energy spectrum shows a monoenergetic character. To demonstrate the robustness of the scheme, several facts such as the surface roughness and the transverse profile of the shaped foil are evaluated. The optimal cutoff thickness and spot size of the foil are given by multi-parametric PIC simulations. These results shall benefit the future experiments and applications.

3.1 Shaped foil target (SFT)

Before introducing the shaped foil target, it is necessary to first understand the underlying physics of the scheme. In Chapter 2, we discussed the minimum target thickness for ion acceleration. Once the target is thicker than the minimum value, the whole target will be opaque to the laser pulse. Then the foil will be accelerated in a hole-boring process with a velocity of β_h. When the CEL arrives at the rear of the foil, the acceleration changes to the

light-sail process. The foil velocity evolution is derived as

$$\frac{d\beta}{dt} = \frac{E^2}{2\pi m_i n_i l c}\frac{1}{\gamma^3}\frac{1-\beta}{1+\beta}, \tag{2.7}$$

As we know, the foil motion depends on the laser electric field E_L and the foil area mass density $\rho = m_i n_i l$. We can modulate the foil motion by matching the transverse profile of the foil with the laser profile. Taking a transversely Gaussian laser pulse for example, $E_L = E_0 exp(-r^2/\sigma_L^2)$ where σ_L is the laser focal radius, we can employ a special foil with transversely varying thickness, e.g., $l = l_0 exp(-r^2/\sigma_T^2)$. Here, one required matching condition is $2/\sigma_L^2 = 1/\sigma_T^2$, that is $\sigma_L = \sqrt{2}\sigma_T$. In this case, the factor $E_L^2/m_i n_i l$ in Eq. (2.8) is a constant and equals $E_0^2/m_i n_0 l_0$ so that the foil motion is independent on the foil and laser transverse profile. The whole foil can thus be accelerated forward uniformly and the foil target deformation can be effectively avoided.

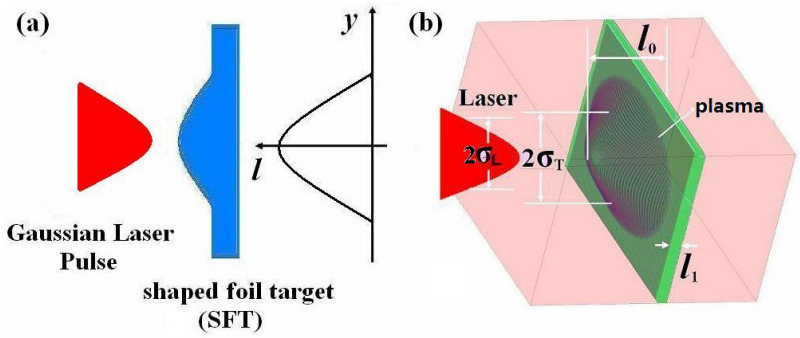

Figure 3.1: Schematic diagram of shaped foil target (SFT) in (a) 2D and (b) 3D cases. The foil geometry is defined by three parameters: l_0, l_1, and σ_T.

Fig. 3.1 shows the foil geometry in both 2D and 3D cases. We call this kind well-matched foil "shaped for target (SFT)". As we can see, the foil geometry is defined by three parameters, that is, the cutoff thickness l_1, the maximal thickness l_0 and the transverse spot radius σ_T. Among these, the maximal foil thickness is defined by the optimal foil acceleration condition, $l_0 = a_0/\pi n$. The transverse foil thickness meets

$$l = max\{l_1, l_0 \times \exp[(-r^2/\sigma_T^2)^m]\}, \tag{3.1}$$

Obviously, if we employ a transversely super-Gaussian laser beam, e.g., $m = 8$, a flat foil can be used to realize a uniform acceleration in multi-dimensional cases. This is also the underlying reason why we usually employ a flat foil and a super-Gaussian laser pulse or even a plane wave when we study ion acceleration in the light-sail regime.

3.2 Ion acceleration using SFT in 2D simulations

To demonstrate the feasibility of the scheme, we operate a series of PIC simulations. First, we do 2D simulations to find an optimal parameter region because they are computationally less expensive than simulations in the full 3D geometry. The total simulation box is $X \times Y = 32\lambda \times 32\lambda$ which corresponds to a grid of 3200×320. The time step of the simulation is $\triangle t = 0.008T_0$, here $T_0 = 3.33$fs is the laser period. The foil plasma consists of two species: electrons and protons. They are initially located in the region $5\lambda \leq X \leq 5.3\lambda$ with the density of $n = 100n_c$ where $n_c = 1.1 \times 10^{21}\mathrm{cm}^{-3}$ is the critical density for the laser pulse with $\lambda = 1\mu$m. We use 216 particles in every simulation cell. Here, a shaped foil target with parameters $l_0 = 0.3\lambda$, $\sigma_T = 7\lambda$, $l_1 = 0.15\lambda$ is employed. By contrast, we also do simulations for a flat target with thickness of $l_1 = 0.3\lambda$. All other parameters are same as the SFT case. The normalized amplitude of the laser electric field at the focus is $a = a_0 exp(-r^2/\sigma_L^2)$ with $a_0 = 100$ and $\sigma_L = 8\lambda$. This corresponds to the laser intensity of $I = 2.76 \times 10^{22}\mathrm{Wcm}^{-2}$ for the assumed laser wavelength. The laser pulse has a trapezoidal temporal intensity profile with duration $1T_0 - 8T_0 - 1T_0$. Thus, the total laser pulse energy is about 793.5 J. At $t = 0$, the laser pulse enters the simulation box from the left boundary.

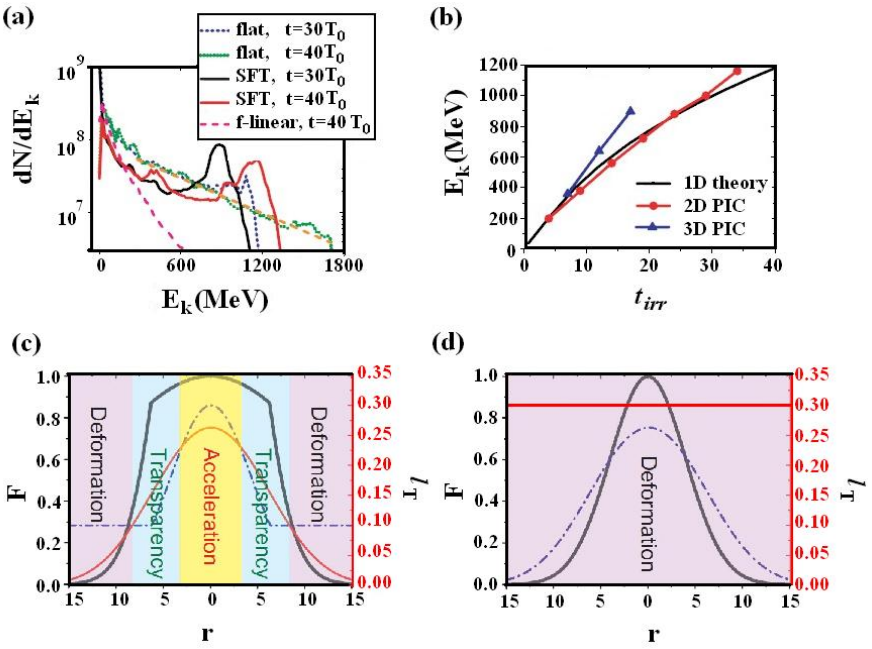

Figure 3.2: (a) Energy spectrum of ions. (b) Energy evolution of accelerated ions from multi-dimensional PIC simulations and 1D theoretical calculation. Here t_{irr} represents the time of laser irradiation on targets. (c) Target partitions in the SFT case and (d) flat target case according to the transparency calculation.

Fig. 3.2(a) shows the energy spectrum of the accelerated ions at $t = 30T_0$ and $40T_0$ for the flat and shaped targets. In the simulation, both the particles and fields satisfy periodical boundary conditions in the transverse direction (Y, Z) and they are within a region of 0.1μm long the Z direction. The flat target produces no obvious peak structure in the energy spectrum. Instead, it shows an exponential decrease like $dN/dE_k \propto exp(-E_k/E_{eff})$ with $E_{eff} = 500$ MeV for $E_k > 300$ MeV and a cutoff energy 1.7 GeV at $t = 40T_0$.

When a SFT is used with the transverse shape factor $\sigma_T = 7\lambda$, the energy spectrum becomes quasi-monoenergetic. The energy of the peak is about 1.2 GeV at $t = 40T_0$, which is very close to the analytical values obtained by solving Eq. (2.8) (see Chapter 2). As we can see, the maximum ion energy at $t_{sim} = 40T_0$ in the 2D simulation is a bit higher than the 1D theoretical value. This is because of reduction of the target area density during the interaction. Although the maximum cutoff energy of the ions in the SFT case is lower than that in a flat target case, much more protons are accelerated in a much narrower region, which benefits the further application of the accelerated proton beams. Overall, the foil acceleration by using the SFT is much improved as compared to a normal flat target.

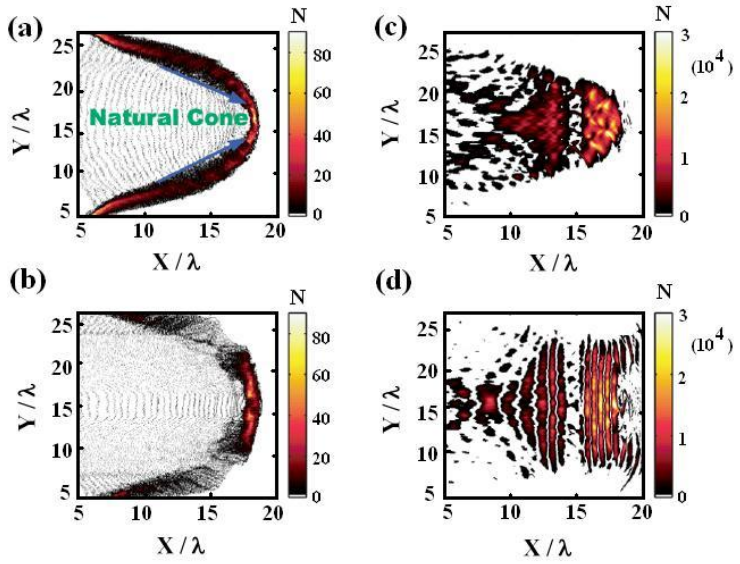

Figure 3.3: Spatial density distribution of ions in (a) flat target case and (b) SFT case at $t = 25T_0$. Spatial distribution of the laser intensity $(E_y^2 + E_z^2)$ in (c) flat target case and (d) SFT case at $t = 25T_0$.

To show the polarization effect, a linearly polarized laser pulse is also tested. The magenta dashed line in Fig. 3.2(a) shows the ion energy spectrum at $t = 40T_0$. In this case, the electrons are easily heated and scattered by the oscillating part of the laser ponderomotive force as discussed in Chapter 2. The target becomes transparent to the laser pulse very soon.

Finally, ions are only accelerated by the spatially dispersed electron cloud and cannot get as high energy as in the circularly polarized pulse case. The energy spectrum is again exponential with a lower cutoff.

Fig. 3.3(a) and (b) show the spatial distribution of ions at $t = 25T_0$ in the flat foil case and SFT case, respectively. The target shaping leads to a more transversely uniform ion acceleration. The initially flat target, in contrary, is deformed and a natural cone builds up during the interaction. The laser intensity distribution shown in Fig. 3.3(c) and (d) confirms this. The natural cone focuses the lateral laser energy to the center and thus reinforces the on-axis ion acceleration. On one hand, this effect destroys the foil, but on the other hand it leads to the higher cutoff energy as shown in Fig. 3.2(a). This is similar with the pre-cone-target used by Cao *et al.* [103]. However, in the present case the cone makes the chromaticity of the accelerated ions worse. When the laser pulse irradiates the cone, electrons are easily extracted out by the laser field from the inner wall of the cone and heated because of the oblique incidence. These heated electrons disperse in space, degrade the stable acceleration structure, and destroy the monoenergetic character of the ion spectrum. Instead, a shaped foil target can reduce these undesirable effects dramatically and the center part of the foil with the radius $\sim \sigma_L$ can be uniformly accelerated as a whole. Finally, the foil target deformation is effectively avoid by using the SFT.

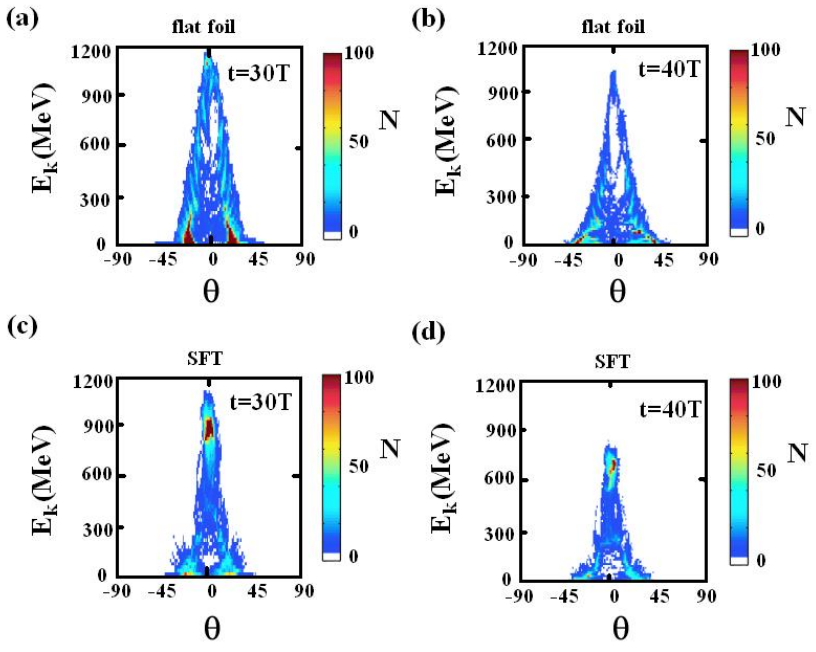

Figure 3.4: Angular distribution of ions at $t = 30T_0$ and $40T_0$. (a) and (b) correspond to the flat target case; (c) and (d) correspond to the SFT case. The color represents the relative ion numbers.

The angular distributions of the accelerated ions in the two target cases are presented in Fig. 3.4. It is shown that in the SFT case the accelerated ions mainly move forward. However, in the flat target case only a small portion of the highly energetic ions moves forward. Ions in the middle energy range get a considerable transverse momentum. From the simulation, we find the average emission angle for the ions whose energy is larger than 1 GeV is about $2.7°$ in the SFT case and $5.22°$ in the flat target case. The number of ions in this energy range is 1.9 times larger in the SFT case as compared to the flat target. Clearly, both the collimation and the total flux of accelerated ions are much improved in the SFT case.

3.3 3D simulations

To ensure that these effects are not a 2D artefact, we perform full 3D simulations. For the shaped foil target, we use $\sigma_T = 6\lambda$ in the 3D simulation. The initial position of the target is moved to $X = 2\lambda$ to reduce the computational cost. The laser longitudinal profile is also reduced to be $1T_0 - 5T_0 - 1T_0$. Other parameters are same as those in the 2D simulation above. The electron and ion distributions at $t = 20T_0$ are shown in Fig. 3.5. As we see, in the SFT case a stable compact target sheath with thickness of about 0.7λ breaks out from the rest of the foil. As expected, the deformation of the target are well suppressed and a energy peak is formed in the proton energy spectrum as displayed in Fig. 3.5(d). By contrast, in the flat target case, Fig. 3.5(c) displays a continuously dispersing ion density distribution. The foil target deformation is serious that results in a broad energy spectrum. The number of ions with energy larger than 800 MeV is 5.09×10^{11} and 6.63×10^{11} for the flat target and shaped target, respectively. And their total energies are 5.05×10^{14} MeV and 6.16×10^{14} MeV, the conversion efficiencies are 15.57% and 19%, respectively. The whole target in the SFT case can be stably accelerated until $t = 30T_0$. After the time, the energy peak dissolves due to the spatial scattering of the protons and other effects, e.g., transverse instabilities.

It deserves to note that in the 3D case the ion energies are higher than the 1D analytical prediction as displayed in Fig. 3.2(b). The calculated peak value of the ion energy is 635 MeV at $t_{sim} = 20T_0$; however, the simulation result is 910 MeV. The difference is also due to the target dispersion. In the 3D geometry electrons disperse easily in the transverse direction, then the laser pulse can also transmit through the lateral parts of the target. Central electrons are dragged out by the transmitted pulse and further disperse in space, which decreases the effective central target area density. Consequently, a few ions in the center part obtain a stronger acceleration. Generally, we find the 1D estimation based on Eq. (2.12) and Eq. (2.13) gives a higher energy conversion efficiency and a lower peak energy.

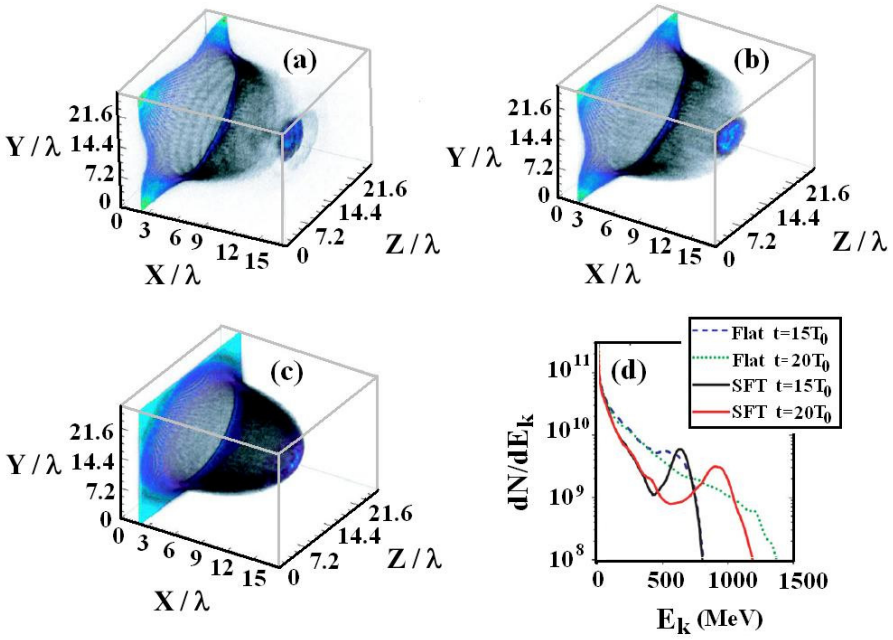

Figure 3.5: Spatial density distribution of electrons (a) and ions (b) in the 3D simulation at $t = 20T_0$ in the SFT case. (c) Spatial density distribution of ions in the flat target case. (d) Energy spectrum of ions in the SFT case and flat target case.

3.4 Three zones in laser-SFT interaction

As shown in Fig. 3.2(c), when a shaped foil target is used, the foil evolves into three different regions during the interaction. The center part is called "acceleration zone" where the ions can be uniformly accelerated. These ions correspond to the peak observed in the energy spectrum. Near to the center part is "transparent zone", where the laser pulse can easily penetrate the foil and propagate into the vacuum. Near to the floor and top is "deformation zone". Due to the existence of a cutoff thickness there, the ions from the "deformation zone" experience almost the same acceleration process as in a flat target. Because the wing of the laser pulse has a much lower intensity, the foil are easily deformed but the ions shall not be strongly accelerated. As a result, the center part at the "acceleration zone" breaks away the main target and a high quality proton bunch is formed behind the initial foil. In fact, all three parts can be clearly observed in Fig. 3.3(b), Fig. 3.5(a) and (b). However, for a flat target, the transparent factor is always lower than the critical value (see below) and the foil velocity is not uniform. The whole target is at the "deformation zone" (see Fig. 3.2(d), Fig. 3.3(a) and Fig. 3.5(c)) and we fail to observe any monoenergetic proton beam.

To explain the effects of the target shape clearly we show the transverse distributions of the acceleration factor ($F = a^2/l$) and the transparency factor ($\alpha = a/\pi nl$) of the target in

Fig. 3.2(c). F is normalized by the maximum value in the target center, which directly relates to the target deformation. In the figure, we also show the minimum thickness requirement from theoretical calculation. As we see when a shaped target is used, the acceleration factor F is almost uniform in the matched region. However, once F is uniform the transparent factor varies. In fact, the center of the SFT is thicker than the minimum value l_{min} so the acceleration factor F_{acc} is almost uniform. Thus, the target can get uniform acceleration. Besides this region, the target thickness is thinner than l_{min}. It will be transparent to the laser pulse and ions can not get effective uniform acceleration. In the outside region, we see the target is thicker than l_{min} again and F_{acc} decreases with radius, so in this region the target will be accelerated and deformed. Obviously, the balance depends on the ratio of the forces due to the laser pressure F_P and the charge separation between ions and electrons F_E,

$$F_P = \frac{m_i c^2 \lambda}{e^2} a^2 \frac{1-\beta_e}{1+\beta_e} dS, \tag{3.2}$$

$$F_E = \frac{m_i c^2 \lambda}{e^2} \pi^2 n^2 l^2 dS, \tag{3.3}$$

Here, the force $F_{P,E}$ and the area element dS are normalized by $m\omega c$ and λ^2, respectively; β_e is the normalized velocity of the compressed electron layer. When $F_P > F_E$, electrons are completely pushed out of the target and the target becomes transparent to the laser pulse later. It corresponds to the transparency factor α larger than the critical value $\alpha_c = \sqrt{(1+\beta_e)/(1-\beta_e)}$. Considering a finite ion mass and relativistic effects, we take $\beta_e = \beta_h = a/(a+\sqrt{mn})$, where β_h is the relativistic hole boring velocity [98]. The ion motion in the pre-hole-boring process is usually omitted; however, it is critical to get the correct value for the transparent thickness of the target.

By considering the space of the transparency region, we can get the maximum final radius of the accelerated ion bunch $r_b \simeq \sigma_T \sigma_L \sqrt{\mathrm{ln}(\alpha_c/\alpha_0)/(\sigma_L^2 - \sigma_T^2)}$, here $\alpha_0 = a_0/\pi n_0 l_0$. So the best choice for l_1 and σ_T should be $l_1 \leq l_0 exp(-r_b^2/\sigma_T^2)$ and $\sigma_T < \sigma_L$. This corresponds to $r_b = 3.1\lambda$, $l_1 \leq 0.23\lambda$ if we take $\sigma_T = 6\lambda$ and $\alpha_c = 1.19$ from Fig. 3.2(c). The bunch size is close to our 3D simulations ($r_b \approx 3.5\lambda$).

3.5 Effects of foil geometry on the ion acceleration

Both 2D and 3D PIC simulations demonstrate the feasibility of the SFT scheme for uniform acceleration by matching the transverse shape of the foil with the laser intensity profile. The energy conversion efficiency from the laser pulse to the high quality ions are much higher than from any other mechanisms, e.g., TNSA. However, the final beam quality is related with

several factors, such as the target shape and laser focal size. In experiments, we should take into account all these factors and choose the appropriative target and laser parameters. Below we discuss in detail the effects of these factors on the ion acceleration. It is very instructive for experiments and applications in future. In order to save the computational time, we only perform 2D simulations but these results are also valid for both 3D cases and real experiments.

3.5.1 Cut-off thickness l_1

We first take into account the influence of cutoff thickness l_1 on the beam quality. In the simulation we fix all other parameters and only vary l_1. The ratio of the target shaped factor to the laser focus (σ_T/σ_L) is kept as $7\lambda/8\lambda$. Fig. 3.6 shows the simulation results. Here, we consider three examples, $l_1 = 0.05\lambda$, 0.15λ and 0.25λ and take $l_0 = 0.3\lambda$. We can see that the spatial ion energy distributions in Fig. 3.6(a) and (b) are almost same. The cutoff thicknesses for these two cases are 0.05λ and 0.15λ, respectively. The corresponding energy spectra are shown in Fig. 3.6(d). Again, the energy distributions of protons for these two cases are also same. However, when we increase l_1 to 0.25λ, the energy spectrum changes significantly as displayed in Fig. 3.6(d). The peak energy decreases and the cutoff energy increases. The spectrum tends to be that of a flat target.

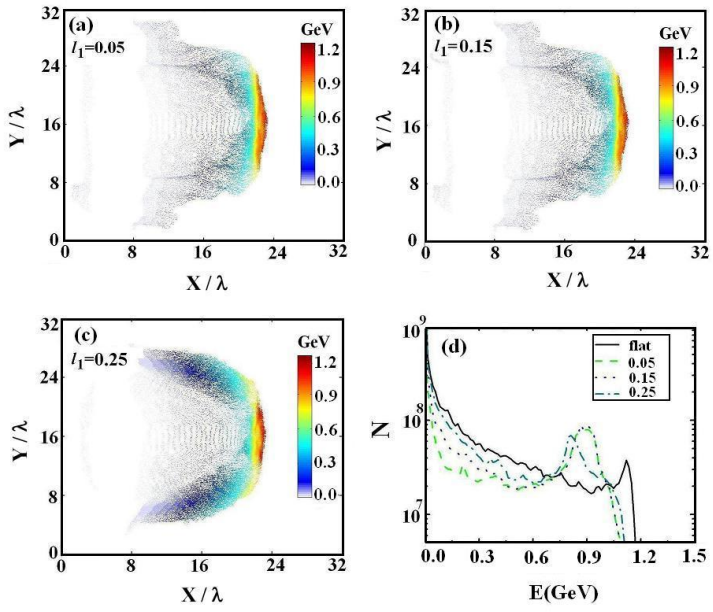

Figure 3.6: Proton energy distributions in $x-y$ space for different l_1: (a) 0.05λ, (b) 0.15λ, and (c) 0.25λ. (d) Proton energy spectra at $t = 30T_0$. Here, the flat target refers to the one with $n_0 = 100n_c$ and $l_0 = l_1 = 0.3\lambda$.

It is shown that there exists a threshold value for the cutoff thickness l_1. When l_1 is larger than the threshold, the spectra are significantly different. In additional simulations, we find that the threshold is about 0.20λ with the present parameters. This is close to the theoretical value of our analysis above. When the cutoff thickness is smaller than $l_0 \times exp(-r_b^2/\sigma_T^2)$, the accelerated bunch size is almost constant as shown in Fig. 3.6(a) and (b). When it increases, no obvious transparency region separates the "acceleration zone" from the deformation region. Target deformation happens continuously along the target and the effectively accelerated bunch is smaller as shown in Fig. 3.6(c). As times goes on, the final ion spectrum gets close to the flat target case.

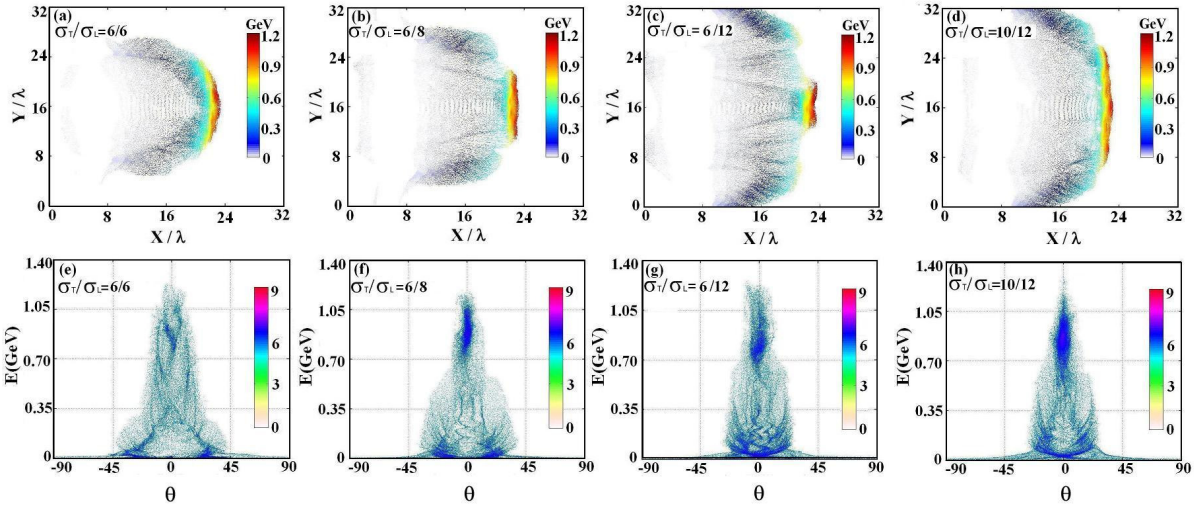

Figure 3.7: Proton energy distributions in $x-y$ space for different σ_T/σ_L at $t = 30T_0$: (a)6/6, (b)6/8, (c)6/12, and (d)10/12. Corresponding proton energy distributions as a function of divergency angle are shown in (e)-(h).

3.5.2 Matching factor $\sigma_T : \sigma_L$

The most important factors are the matching parameters: σ_T and σ_L. In the following we check their effects on the beam quality. Fig. 3.7 shows some typical simulation results for different σ_T and σ_L. The top four figures show the proton energy distributions in space while the bottom four correspond to the angular distributions. We fix $\sigma_T = 6\lambda$ and increase σ_L from 6λ to 12λ. It is shown that when σ_T is close to σ_L, target deformation happens. Most protons are located at the deformation region and the target evolves into a natural cone as observed in a flat foil case. The corresponding energy divergency distribution is widely spread, as displayed in Fig. 3.7(e). With the increase of the laser focus size, the center part of the target is uniformly accelerated so that it can break away from the whole target. The three regions

mentioned above can be easily distinguished from Fig. 3.7(b) and (c). A bunch of protons with higher energy and better collimation is formed in Fig. 3.7(f) and (g). The radius of the bunch decreases with σ_L, which confirms the theoretical analysis. When σ_L increases further, the transparency region extends to the target center and a larger laser focus (or laser energy) leads to a smaller accelerated bunch. These results show the importance of a well-matched target. Fig. 3.7(d) and (h) correspond to a well-matched case when the laser focus is $\sigma_L = 12\lambda$. When we increase the target width close to the σ_L, the acceleration region broadens and more ions are uniformly accelerated.

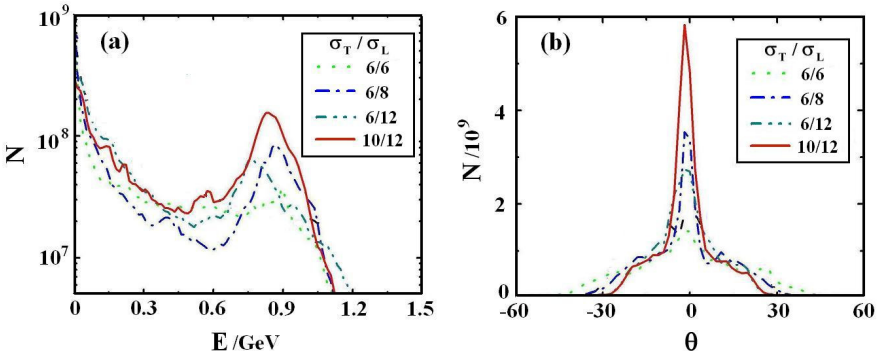

Figure 3.8: (a) Proton energy spectra and (b) divergency angle distributions for different laser focus radii σ_L and σ_T at $t = 30T_0$.

Fig. 3.8 shows both the energy spectra and the angular distributions for these cases. As expected, there is a clear quasi-monoenergetic peak in the case with $\sigma_T/\sigma_L = 6/8$ and $\sigma_T/\sigma_L = 10/12$. The peak energy is about 0.85GeV and 0.80 GeV, respectively. The corresponding full-width at half-maximum divergency angle is about 6λ and 4λ. Obviously, for the well-matched cases the larger the laser focus, the more protons are accelerated. In contrast, for the imperfectly matched case, both the peak energy and the total production of accelerated protons decrease. For the unmatched case, no clear peak appears and the proton number decreases further.

Table 3.1: Available and optimum values of σ_T/σ_L.

σ_T/σ_L							
Optimal values	Available values						$\sigma_T(\lambda)$
0.75	0.50	0.583	0.677	0.75	0.833	0.916	6
0.8125	0.375	0.50	0.60	0.75	0.8125	0.875	8
0.80	0.40	0.50	0.60	0.70	0.80	0.90	10

Note: The available values mean that a high quality proton bunch with a quasi-monoenergetic peak and low divergency angle can be observed but optimum values indicate the best bunch quality such as the narrowest energy spread and the lowest divergency.

In order to obtain the optimal ratio of σ_T/σ_L in the simulation, we perform the parameter scan as shown in Table (3.1). Here, all the target and laser parameters are same except for σ_T and σ_L. The available values of σ_T/σ_L mean that a high quality proton bunch with a quasi-monoenergetic peak and low divergency angle can be observed with these parameters. The optimum value indicates the best bunch quality such as the narrowest energy spread and the lowest divergency. It is shown that the tolerable values of σ_T/σ_L exist around 0.50-0.90 while the optimum value is about 0.80. These simulations supplement our analytical results, which only give the condition of $\sigma_T/\sigma_L < 1$ and also give some quantitative illumination to the experiments.

3.5.3 Surface roughness

Since in our scheme the target thickness is smaller than the laser wavelength, e.g. nanometer thickness, the relatively larger surface roughness of the target might be inevitable in real experiments, which may influence the final accelerated ion beam. Here we check its effects by comparing three simulations with different surface roughness: (a) a smooth surface, (b) 10% roughness and (c) 30% roughness. In our simulation, the roughness is completely randomly selected, which is close to a real target in experiments. It means that there are no "typical wavelengths" of the surface modulation as shown in Fig. 3.9(a). The amplitude of the roughness just means perturbation as a fraction of target thickness.

In the simulation, we randomly selected the left boundary of the plasma within the modulation amplitude along the transverse direction. The left boundary coordinate is $x_r(j) = x_s(j) - a \times f(j)$; here a is the modulation amplitude of the roughness and $f(j)$ is a random value within [0,1], j is the label of the cell in the transverse direction and $x_s(j)$ is the left boundary of a smooth target. The minimum undulation length of the roughness in the transverse direction is the cell length, which is 0.01λ. In order to resolve this surface roughness, both the longitudinal and transversal cell sizes should be small enough, which leads to extremely small steps in both space and time in the simulation. It makes the simulations extremely time consuming. Therefore, we only present the simulation results at an early time, e.g., $t = 10T_0$. This time is, however, long enough to see the final effects.

Fig. 3.9(c) shows proton energy spectra for these cases. We notice that all the spectra show a clear energy peak despite the different surface roughness. Yet, for the target with 30% surface roughness, the peak energy is about 0.25 GeV, which is higher than the value of 0.2 GeV in cases with a lower roughness. Similarly, the cutoff energy is also higher than the other two cases. The differences between the two lower roughness cases are much smaller. The main effect of the target roughness is to increase the laser absorption and conversion efficiency of its

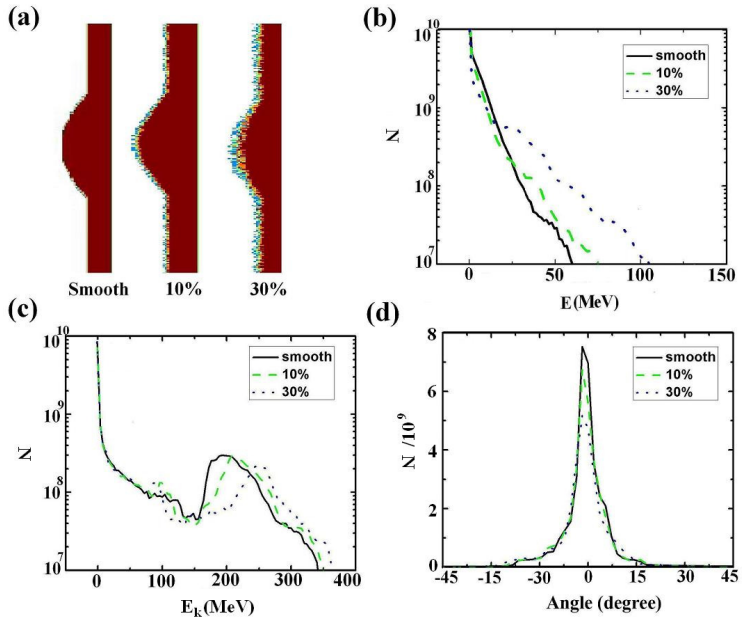

Figure 3.9: (a) Shaped foil targets with different surface roughness . (b) Electron energy spectra and (c) proton energy spectra for different surface roughness at $t = 20T_0$. (d) Proton divergency angle distributions at $t = 20T_0$. Here, the cutoff thickness for these cases is 0.15λ.

energy to superhot electrons. These hot electrons are easily dispersed in space and initiate the TNSA acceleration. This can be seen in Fig. 3.9(b) where the energy spectrum of the electrons is shown. Obviously the target with 30% roughness has a much higher electron temperature. The other two cases are similar. In addition to the energy spectrum, we also check the angular distribution. The results are shown in Fig. 3.9(d). There is no obvious difference with the case of a smooth target and a target with 10% roughness. So we believe a roughness of 10% should be acceptable in real experiments.

3.6 Conclusion

In this chapter, a shaped foil target was proposed to avoid the foil target deformation when a transversely Gaussian laser beam is incident on an ultra-thin solid foil. During the interaction, the foil is divided into three zones: acceleration zone (center), deformation zone (floor and top), and transparent zone (lateral). Among these, the ions located at the "acceleration zone" can be uniformly accelerated and it shows a well pronouncing monoenergetic peak in the energy spectrum and a low emittance in the angle distribution. Both 2D and 3D PIC simulations demonstrate that the beam quality in the SFT cases is much improved as compared to

the normal flat foil case. The peak energy evolution also agrees well with the 1D calculation based on Eq. (2.12) and Eq. (2.13). Besides, the effects of the foil geometry on the ion acceleration, such as the cutoff thickness, matching factor σ_T/σ_L and the foil surface roughness are evaluated. It is shown that there exists a threshold value for the cutoff thickness l_1. The best σ_T/σ_L is around 0.8 that is a little larger than the theory estimation $1/\sqrt{2}$. The simulations also indicate that the surface roughness within 10% is acceptable, above which the peak in the energy spectrum lowers and finally disappears.

It deserves to point out that target shaping only helps to reduce the electron heating and keeps the acceleration much more uniform for a longer time. However, transverse instabilities still exist in the accelerated plasma. Under the perfect matching condition, although the number of high quality protons can be increased by enlarging the laser focus size as Fig. 3.7(d) suggests, the surface instability will develop after some time which destroys the ion acceleration structure. These effects limit the final energy gain of protons [23, 95, 101]. Suppression of such kinds of instabilities should be an tough challenge both for the laser-driven ion acceleration itself and for fast ignition for ICF based on laser-accelerated ion beams [79, 104]. One may argue that a periodic modulation of the foil surface may suppress or excite the instabilities. However, in present simulations we have not observed the roughness effects on the transverse instability. A detailed discussion of the transverse instabilities will be addressed in Chapter 5.

Chapter 4

Improved ion acceleration in density modulated foil targets

In this chapter, we suggest an alternative scheme to produce high quality proton beams by avoiding the foil target deformation using so-called density modulated foil target (DMFT). In this case, the initial foil target is a flat one, but the transverse plasma density follows a Gaussian distribution to match the laser intensity profile. A circularly polarized laser pulse is employed and normally incident onto this target from the left boundary. Both 2D and 3D simulations have been performed, which show that protons from the center part of the target can be monoenergetically accelerated and are well collimated in the forward direction. The final proton peak energy is as high as 1.4 GeV with the full-width of half maximum divergence cone of less than 4°. Overall, the beam quality is improved as compared to the case using a SFT. The reason should be attributed to the surface curvature of the SFT that makes the electromagnetic wave obliquely irradiate the foil surface. The resulting electron heating is inevitable though it is not so significant as in a flat foil case. By using the DMFT, we overcome this issue perfectly because the initial foil is a flat one and the electron heating can thus be significantly suppressed. Without considering experimental feasibilities, e.g., foil engineering and laser pointing accuracy in experiments, we believe that the proposed DMFT is a better choice for GeV monoenergetic proton beam generation.

4.1 Density modulated foil target (DMFT) and 2D simulations

In principle, we may modulate the foil area mass density $\rho = m_i n_0 l_0$ to match the transverse laser profile as suggested in Chapter 2 and in Ref. [105]. However, it is relatively too difficult to operate in experiments with current foil fabricating technologies. Here, we propose an alternative scheme, called density modulated foil target (DMFT). In this scheme, we keep the foil thickness but vary transverse foil density to match the laser intensity profile. Fig. 4.1 shows the geometry of DMFT in both 2D and 3D cases. Similar to the SFT in Chapter 3, the foil density profile is also defined by three parameters: the cut-off density n_1, the maximal density n_0 and the matching factor σ_D. Obviously, one required condition based on Eq. (2.12) (see Chapter 2) is $\sigma_D \approx \sigma_L/\sqrt{2}$. The foil thickness is also defined by $l_0 = a/\pi n_0$ so that we can get an optimal foil acceleration in the light-sail regime.

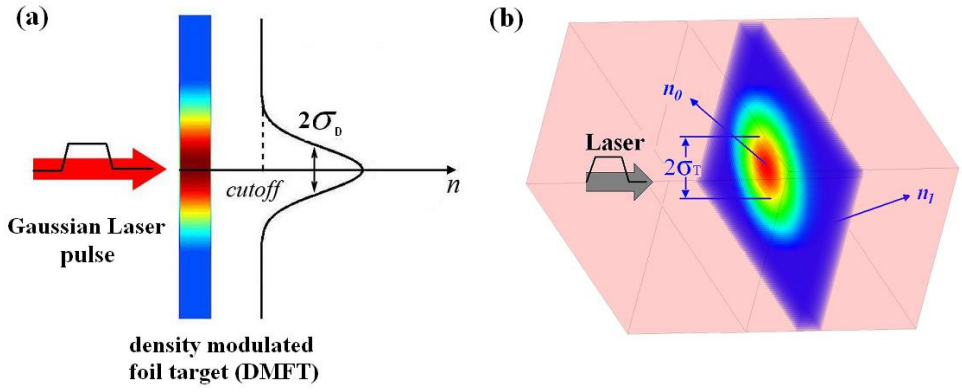

Figure 4.1: Schematic diagram of the DMFT scheme in (a) 2D and (b) 3D cases. The foil density profile is also defined by three parameters: the cut-off density n_1, the maximal density n_0, and the matching factor σ_D.

We first present 2D simulation results of the scenario using the PIC code VLPL. The simulation box is 48λ long and 32λ wide with the laser wavelength $\lambda = 1.0\mu\mathrm{m}$. Totally, 4800×320 cells are employed and more than 4.2×10^6 macro-particles are used in the simulations. The foil target is initially located between $x = 5.0\lambda$ and 5.3λ. A circularly polarized laser pulse with a Gaussian profile in space and a trapezoidal profile in time is normally incident on the

foil target. Thus the dimensionless laser amplitude satisfies

$$a = a_0 \exp\left(-\frac{y^2}{\sigma_L^2}\right) t, \quad 0 \le t < 1T_0, \tag{4.1}$$

$$a = a_0 \exp\left(-\frac{y^2}{\sigma_L^2}\right), \quad 1T_0 \le t \le 9T_0, \tag{4.2}$$

$$a = a_0 \exp\left(-\frac{y^2}{\sigma_L^2}\right) (10 - t), \quad 9T_0 < t \le 10T_0, \tag{4.3}$$

where $a_0 = 100$ is the top laser intensity, $\sigma_L = 8\lambda$ is the focal spot radius. The initial plasma density follows a transversely Gaussian distribution to match the laser intensity profile with the parameters $\sigma_D = 7\lambda$, $n_0 = 100n_c$ and $n_1 = 20n_c$. The transverse boundary conditions are periodic while both the front and back boundaries absorb outgoing radiation and particles. Considering the plasma expansion into vacuum, we provide an appropriate vacuum gap (longer than 42μm) between the foil target and the right boundary.

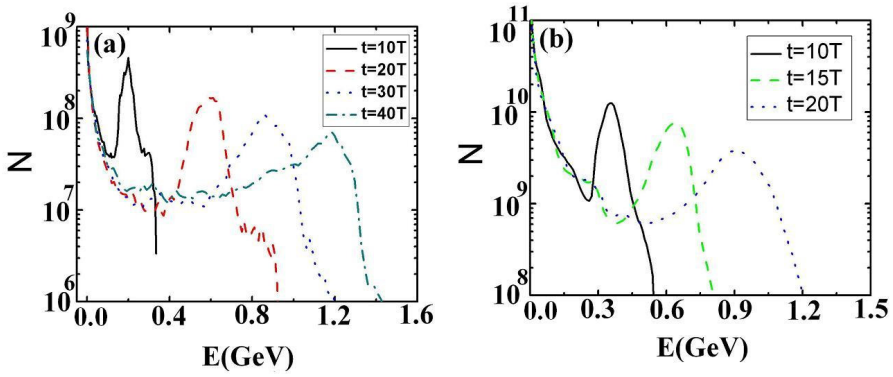

Figure 4.2: Proton energy spectra for the DMFT case in the (a) 2D simulation and (b) 3D simulation.

Fig. 4.2 (a) shows the evolution of proton energy spectrum at $t = 10T_0, 20T_0, 30T_0$, and $40T_0$. Here, the leading edge of the laser pulse reaches the left side of the foil target at about $t = 5T_0$. A clear quasi-monoenergetic peak can be seen in each spectrum. At an early time, e.g., $t = 10T_0$, the peak energy is about 200 MeV with a very narrow energy spread. As time goes on, the proton energy increases and more protons can be accelerated. At $t = 40T_0$, the peak is still very clear although the spectrum shows a relatively wide energy spread. By this time, the peak energy is as high as 1.2 GeV corresponding to 6.5×10^7 protons while the cutoff energy is about 1.5 GeV. The total number of the protons within the energy range 0.8−1.3 GeV is 2.0×10^{10}. The monoenergetic peak is accelerated up to 1.4 GeV with the full-width of half maximum divergence cone of less than 4° at $t = 50T_0$ (165fs).

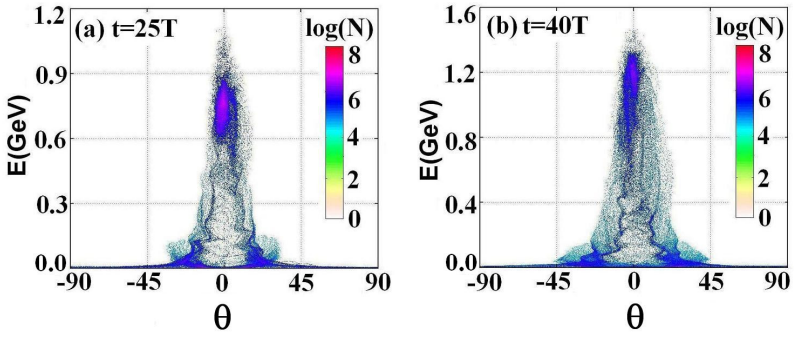

Figure 4.3: Proton energy as a function of the divergency angle for the DMFT in the 2D simulation at (a) $t = 25T_0$ and (b) $40T_0$.

The proton energy as a function of the divergency angle is shown in Fig. 4.3. It is easy to see from both of the frames that there exists a bunch of protons with a relatively high energy and low divergency. At $t = 25T_0$, the clump is composed of protons within the energy range 0.65−0.85 GeV. However, at a later time $t = 40T_0$, the same protons are shifted to the energy range 0.8−1.3 GeV. The average divergency angle for all these high quality protons is about $2.2°$ at $t = 25T_0$ and $3.5°$ at $t = 40T_0$. Here, the average divergency is calculated as following:

$$\theta_{ave} = \sqrt{\sum_{i=1,..N} (\theta_i)^2/N}, \quad \theta_i = tan^{-1}(p_y/p_x), \tag{4.4}$$

where N is the total number of the high quality protons, p_x and p_y are the momentum component in $X-$ and $Y-$direction, respectively.

Fig. 4.4 presents snapshots of the laser intensity and proton acceleration process at $t = 25T_0$ and $t = 40T_0$. Because of the lower density at the target wing, the ultra-intense laser pulse can easily penetrate the foil and then propagate into the vacuum behind the target. On the contrary, the center part of the target in the range between $Y = 10\lambda$ and $Y = 22\lambda$ is directly pushed forward by the laser radiation pressure. As a result, the laser intensity shows a clear inverted cone distribution, as displayed in Fig. 4.4(a) and (b). This inverse cone plays a very important role in proton acceleration because it always wraps the protons and keeps them together. Finally, we observe that the proton bunch becomes compact and the radius is comparable to the foil spot size σ_D. According to the theory in Chapter 2, the whole center part of the foil experiences a uniform acceleration and the foil target deformation is well avoided so that a good acceleration structure survives for a longer time, as displayed in Fig. 4.4(c) and (d).

Additionally, we also record the proton energy distribution in space (see Fig. 4.4(e) and (f)). Comparing with the density distributions, one can easily recognize the high quality proton clump mentioned above. The "radius" of the clump is about 6λ at $t = 25T_0$ and 8λ at

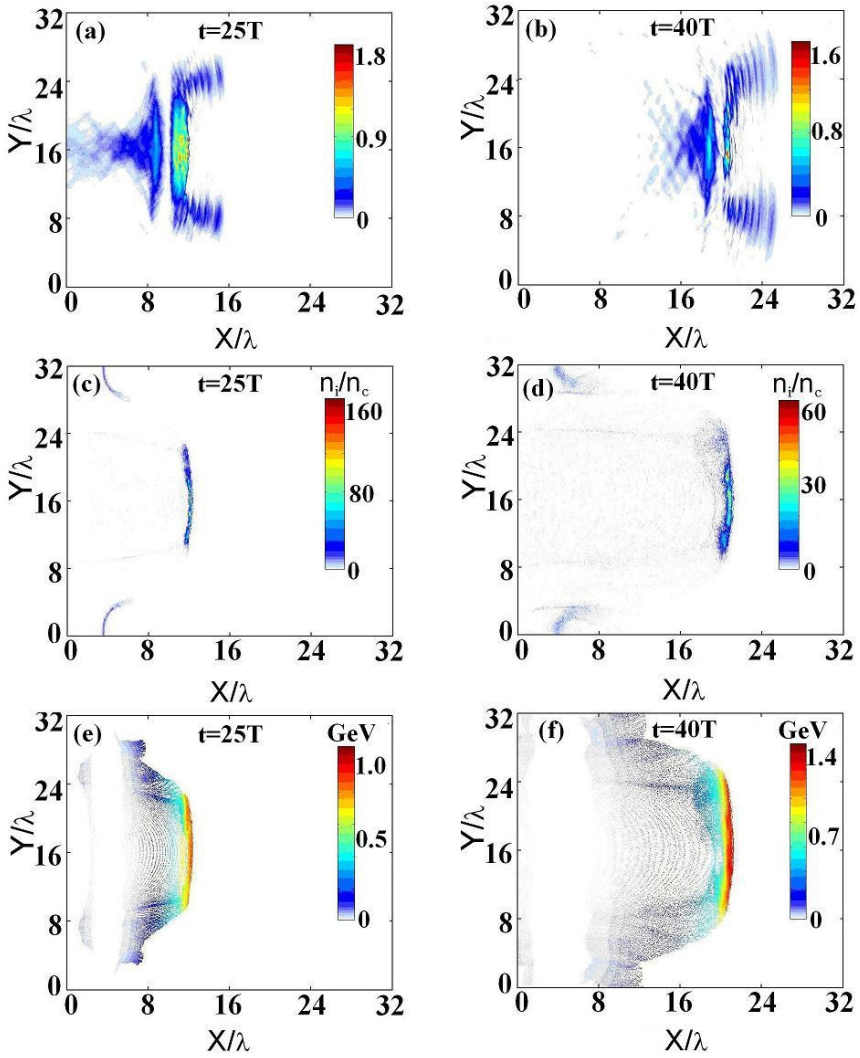

Figure 4.4: Spatial distributions of (a,b) laser intensity $(E_y^2 + E_z^2)$, (c,d) proton density, (e,f) proton energy for the DMFT case in the 2D simulation at (a,c,e) $t = 25T_0$ and (b,d,f) $t = 40T_0$.

$t = 40T_0$, which approximately equals the laser focus size σ_L.

4.2 3D simulations

3D PIC simulations have also been performed to check the robustness of the DMFT scheme. Here, both the geometry of the DMFT and the laser profile are same as in the 2D case above except the initial target position and σ_D. In the 2D case, the target is located at $x = 5\lambda$ with

$\sigma_D = 7\lambda$ while in the 3D case they are 2λ and 6λ, respectively. The pulse duration in the 3D simulations is $7T_0$, which corresponds to a trapezoidal profile $1T_0 - 5T_0 - 1T_0$. To reduce the computational time, the full simulation box has a size $X \times Y \times Z = 25\lambda \times 27\lambda \times 27\lambda$ sampled by a grid of $2500 \times 225 \times 225$ cells. Each sell has 8 macro-particles. Fig. 4.2(b) shows the proton energy spectra at $t = 10T_0$, $15T_0$ and $20T_0$. An obvious energy peak can be observed there. At $t = 20T_0$, the spectrum shows a peak with energy of 0.9 GeV corresponding to 5.4×10^9 protons. The total number of the protons with energy larger than 0.6 GeV is about 1.1×10^{12}, which contains a total energy of $155J$. The energy conversion efficiency from the laser pulse to these protons is as high as 27.1%, which is much higher than that obtained in most other mechanisms, e.g., TNSA.

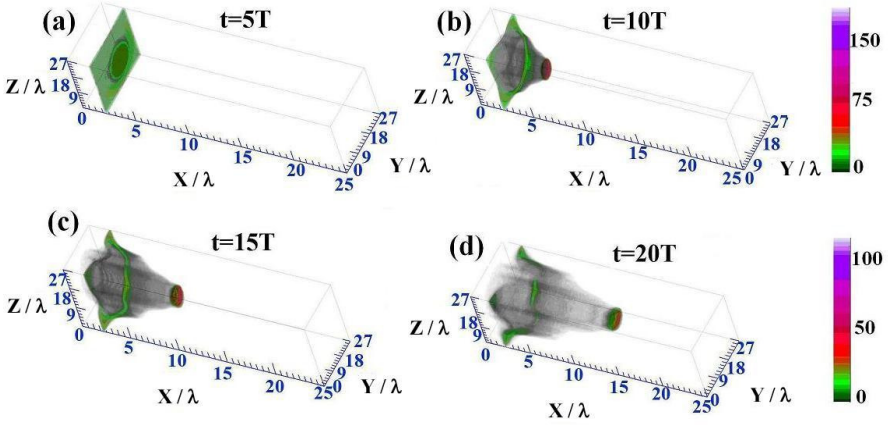

Figure 4.5: Spatial density distributions of protons for the DMFT case in the 3D simulation at $t = 5T_0$, $10T_0$, $15T_0$ and $20T_0$. A clear proton clump formed behind the target can be easily distinguished from (b), (c) and (e).

Fig. 4.5 presents the spatial density distribution of protons at different time points. We can see that the target can keep a good acceleration structure. The simulations confirm the results in the above 2D simulations. Additionally, we also observe the expected proton clump behind the target in the 3D simulations, as displayed in Fig. 4.5(b)-(d). The radius of the clump is about 4.5λ, which is smaller than the laser focus. It may be due to the easier dispersion of the protons in the 3D condition. In fact, the size of the clump depends on the cutoff density, laser focus as well as σ_D. When σ_D is matched with the laser focus, for a lower cutoff density more protons from the wing target will be uniformly accelerated, leading to a wider clump radius. On the contrary, those wing protons from the "deformation zone" experienced inhomogeneous forces and would be "filtered" by the laser pulse. As a preliminary estimation, the optimal cutoff density is half of the maximum, that is $50n_c$ in the present DMFT case.

4.3 Comparison with other foil geometries

In order to get an optimal foil geometry, we employ some additional DMFTs with various foil geometries. Here, we consider four different foil profiles as shown in Fig. 4.6(a). Among them, the case 2 is just the usual flat foil target (UFT) with the density of $100n_c$ while the case 3 is another specially-organized foil target with a density of transverse linear distribution. Both of the maximal density and cutoff density in the case 1 and 3 are same. Case 4 is a SFT proposed in Chapter 3, where the transverse foil thickness is matched to the laser intensity profile. For convenience, the SFT is made with a matched profile (corresponding to a cutoff thickness of 0.06λ) so that the whole target contains the same number of protons as that in the DMFT case. All these targets are located at the same position with the same thickness (for the SFT, it is the maximal thickness) and are irradiated by the same circularly polarized laser pulse. In order to save the computational time, we only perform 2D PIC simulations.

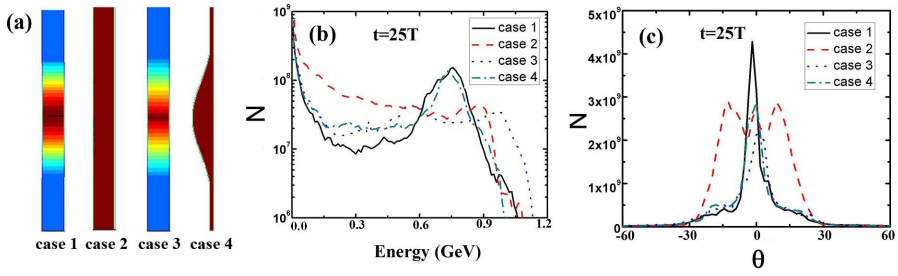

Figure 4.6: (a) Comparison among different target profiles. (b) Proton energy spectra and (c) divergency angle distributions at $t = 25T_0$.

Fig. 4.6(b) presents the spectra of all protons at $t = 25T_0$. Obviously, only the spectrum in the case 1 and 4 show a quasi-monoenergetic peak feature. That is because the both targets employ a Gaussian profile (transverse thickness or density) to match the laser intensity profile, which leads to a uniform acceleration of the target. In the UFT case, the acceleration structure is destroyed very soon due to the deformation of the foil and the spectrum shows an exponential decay. In the case 3, we do observe formation of an inverse cone in the laser intensity distribution. Yet, different sections of the target experience different acceleration because the target profile is not well matched with that of the laser. Due to the transverse linear distribution of the density, the energy spectrum is not an exponential one, but rather shows a nearly flat distribution. When we compare the DMFT with the SFT, it deserves to note that there are almost no difference for the distributions of high energy protons except that, in the DMFT case, the number of low energy protons is reduced and more energy is focused on the clump mentioned above. Finally, the energy conversion efficiency from the laser pulse to the high quality protons is increased.

Finally, we compare the divergence angle for these cases as displayed in Fig. 4.6(c). As expected, both the DMFT and SFT can produce a well-collimated proton beam. On the contrary, the angle distribution for the UFT shows a larger divergency. That is because the electrons in the UFT are easily scattered and heated by the laser. These hot electrons gradually spread into the vacuum and the TNSA dominates the ion acceleration. However, in the DMFT case and SFT case, all parts of the target (within the laser focus) are pushed forward as a whole by the laser radiation pressure. Then, the protons have a low divergency angle. On the other hand, compared to the SFT, the proton collimation in the DMFT case is much better because the shape of the SFT leads to somewhat electron scattering and heating in space. Another reason comes from the contribution of the inverse cone of the laser intensity formed behind the DMFT, which always keeps the protons together. Finally. the number of protons with the full-width of half maximum divergence cone of less than $2.7°$ in the SFT is about 1.8×10^{10}, which is only about 80% of that in the DMFT case. Overall, the beam quality in the DMFT case is higher than in the SFT and much better than in the UFT.

4.4 Conclusion

In conclusion, we studied proton acceleration from a density-modulated foil target. In order to avoid the deformation of the foil target, the transverse foil density follows a transversely Gaussian distribution to match the laser intensity profile. Meanwhile, a circularly polarized laser pulse at intensities of $2.72 \times 10^{22}\mathrm{Wcm}^{-2}$ is employed to push the target forward uniformly. Both 2D and 3D simulations demonstrate the generation of high quality proton beams. A proton clump with a higher energy and better collimation is observed behind the target, whose radius approximately equals the foil spot σ_D in the 2D simulations. The peak energy of the quasi-monoenergetic protons can be as high as 1.4 GeV. The corresponding full-width of half maximum divergence cone is less than $4.0°$. The energy conversion efficiency can be up to 27.1% in the 3D simulation which is higher than in the SFT case. By comparison to other foil geometries, e.g., UFT and SFT, both the acceleration structure and the beam quality as well as the energy conversion efficiency in the DMFT case are much improved.

In experiments, however, DMFT is hard to fabricate because it requires a very high accurateness of the special density distribution along the transverse direction. The above-mentioned SFT scheme seems to be a little easier because we can control the foil profile by several methods such as molecular beam epitaxy technique (MBE) [106], physical vapor deposition (PVD) [107] or chemical vapor deposition (CVD) [108]. Currently, a smooth control of the foil density distribution is out of reach in laboratories. In the following chapters, our attention will be focused on the more practical scheme, i.e., the SFT.

Chapter 5

Stable proton acceleration in two-ion-species shaped foil targets

By using the proposed SFT and DMFT, we succeed in avoiding the foil target deformation and obtaining uniform proton acceleration. However, the acceleration structure is not stable as we discussed in Chapter 2 because of the fast-growth of Rayleigh-Taylor-like (RT) instability. The proton beam can be accelerated for a short time, and then disperses in space. The ion energy spectrum becomes broader at a later time as displayed in Fig. 3.2 and Fig. 4.2. Finally, all the protons are scattered in space and no monoenergetic peak can be observed. In this chapter, we concentrate on the RT-like instability and try to get a solution to overcome or suppress it. By multi-dimensional PIC simulations, it is shown that the proton-RT instability can be significantly suppressed by using a two-ion-species shaped foil. The physics underlying the simulations is abundant and worth studying in detail. We create a simple three-interface model to interpret the suppression of proton-RT instability which agrees well with the numerical observations in a variety of cases.

5.1 1D simulations for a two-ion-species foil

We first consider 1D simulations by using a two-ion-species ultra-thin foil to check the differences from a single-ion-species foil, e.g., hydrogen foil as discussed in Chapter 2 and 3. The foil is assumed to be composed of heavier carbon ions and lighter protons. In the first case, the longitudinal length of the simulation box is $x = 60\lambda$ with 6×10^4 cells so that the expected density spike can be resolved. For simplicity, we take the laser wavelength as

$\lambda = 1.0\mu$m. Each cell contains about 100 numerical macro-particles. The target is 0.1λ long, located at $x = 10\lambda$ and composed of fully ionized C^{6+} and H^+ with same number density $71.42n_c$, which corresponds to an electron density $n_e = 500n_c$. A circularly polarized laser pulse is incident from the left boundary at $t = 0$. The laser intensity follows a trapezoidal profile in time. The dimensionless laser amplitude is $a_0 = 100$ and the duration is $\tau_L = 16T_0$ (~ 52.8fs, $1T_0 - 14T_0 - 1T_0$). Absorbing boundary conditions are applied to both the fields and particles.

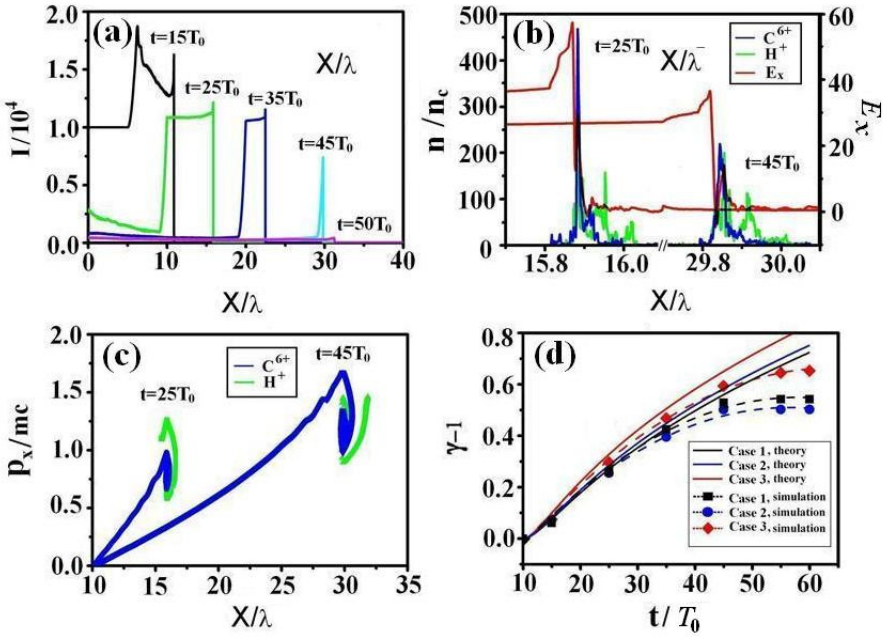

Figure 5.1: (a) Laser intensity evolution. (b) Carbon ion and proton density distributions as well as accelerating field E_x at $t = 25T_0$ and $45T_0$. (c) Carbon ion and proton phase space distributions at $t = 25T_0$ and $45T_0$. (d) Proton energy evolution.

Fig. 5.1(a) shows the laser intensity evolution. The wave front of the laser pulse arrives at the foil surface at $t = 10T_0$. We can see that a part of the incident laser pulse is initially reflected by the target at $t = 15T_0$ because the foil is opaque to the laser. The laser energy is continuously transferred to the foil until the laser-foil interaction ends at about $t = 45T_0$. Fig. 5.1(b) presents the distribution of ion density n_C, n_H, and the accelerating field E_x. At the first stage of the RPA, the electrons are pushed out by the $\mathbf{J} \times \mathbf{B}$ force and a strong charge separation field forms at the foil rear. This is similar to what we observed in a pure hydrogen SFT [87, 89]. Because of the higher charge-to-mass ratio Z_H/m_H, protons quickly move to the front of the foil at the beginning of the interaction. The separation time can be estimated by $t_{sep} = \sqrt{2lm_H/eE_L} = 2.5$fs. The ions then experience different accelerating fields, as shown by the red spike in the field distribution. As we can see, the accelerating field

inside the carbon layer is much stronger than in the proton layer so that the carbon ions can be accelerated together with the protons. The acceleration process repeats until $t = 45T_0$, similar to the "snow-plough" in the electron acceleration [109].

These simulation results also agree well with the Refs. [83, 86] where a typical "spiral structure" was observed in a pure hydrogen flat foil. The fact that both the heads of carbon ions and protons interlace with each other in phase space as shown in Fig. 5.1(c), demonstrates the above assumption on the ion acceleration process. The averaged proton energy evolution is shown in Fig. 5.1(d). At $t = 45T_0$, the proton energy is as high as 500 MeV, which is slightly higher than the carbon ion energy 450 MeV/u. Such high energies with a pronounced monoenergetic peak are yet unreachable in other acceleration mechanisms. For comparison, we also show the theoretical predictions of Eq. (2.13) in the figure marked by solid curves. Obviously, the simulations agree with the predictions though we observe some deviations at later time (see Sec.5.5 below).

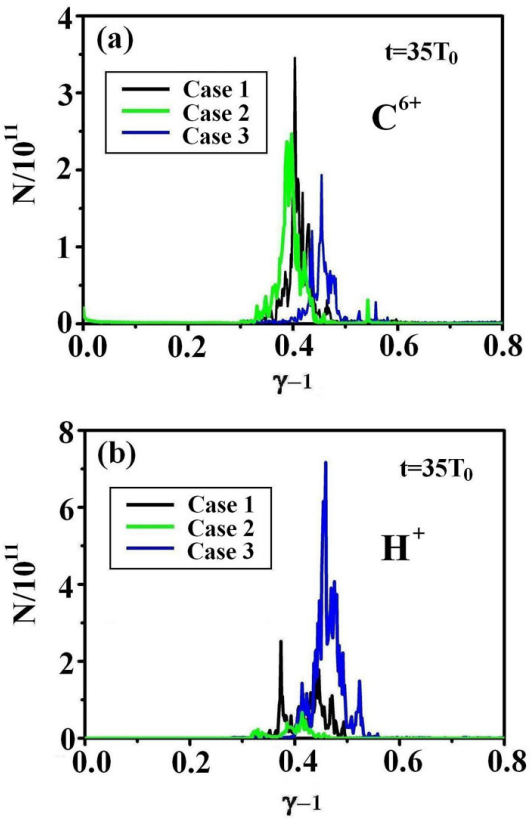

Figure 5.2: Energy spectra of (a) carbon ions and (b) protons at $t = 35T_0$. The ion density ratio $n_C : n_H$ in all three cases is 1:1 (case 1), 4:1 (case 2), and 1:4 (case 3), respectively.

We also performed additional simulations to investigate the influence of the foil composition on the final proton energy. The laser and foil parameters are same as in the case above, except for the ion density ratio. We keep the electron density same but vary the ion density ratio $n_{\mathrm{C}} : n_{\mathrm{H}}$ from $1:1$ (case 1) to $4:1$ (case 2) and $1:4$ (case 3). The area mass density ρ in the three cases is $\rho_2 : \rho_1 : \rho_3 = 1.06 : 1.00 : 0.86$. The ion energy spectra at $t = 35T_0$ are shown in Fig. 5.2. Apparently, both carbon ions and protons show a clear monoenergetic peak in spite of different area mass density ρ. Overall, the carbon ion energy per nucleon is a little lower than the proton's. For the case 1 and 2, they have similar ion energy spectra due to the close area mass density. For the case 3, the protons can be accelerated more efficiently because of the lower area mass density ρ_3. The averaged ion energy evolution is also shown in Fig. 5.1(d). As expected, a similar curve for the case 1 and 2 is observed though the proton density significantly decreases from $71.42n_c$ to $20n_c$. This demonstrates that the overall foil acceleration depends weakly on the foil composition. While reducing the area mass density, the protons tend to be more efficiently accelerated. We also find that the average proton energies for the cases are very close to the theoretical predictions as marked by the solid curve in the figure, though a deviation is observed at the post-interaction stage.

We should mention that radiation reaction (RR) effects are generally recognized to become important when the laser intensity is above $10^{22}\mathrm{Wcm}^{-2}$ [110, 111] because the electromagnetic field emitted by such a relativistic electron might influence the motion of the electron itself and thus the ion acceleration through space-charge fields. However, recent studies indicate that, for a circularly polarized laser pulse, the RR effects become relevant only when the foil is thin enough for the laser pulse to break through it [112, 113]. In this case, the final proton energy can be even increased slightly. However, such effects are not the focus of this chapter and are to be addressed in Chapter 6 in detail.

5.2 Stable proton acceleration from a two-ion-species shaped foil

The 1D simulations mentioned above confirm that the light-sail regime is still valid for a two-ion-species foil and both carbon ions and protons can be accelerated forward as a whole. However, we don't take into account multi-dimensional effects in the 1D case. Multi-dimensional simulations might exhibit a radically different acceleration dynamics if we consider multi-dimensional effects - such as transverse expansion of the bunch and the RT-like instability. In order to extend the 1D model to 2D simulations smoothly, we first have to employ a shaped foil target (SFT) [87] to avoid the foil target deformation. In the following 2D simulations, the box is $X \times Y = 80\lambda \times 32\lambda$, sampled by 16000×400 cells. Each cell

contains 100 macro-particles in the plasma region. The foil is initially located at $x = 10\lambda$ with parameters $l_0 = 0.1\lambda$, $l_1 = 0.05\lambda$, and $\sigma_T = 7\lambda$. The carbon ion density is $51.9n_c$, intermingled with protons of density $8.64n_c$ so that the total electron density is $320n_c$. A transversely Gaussian laser pulse with the focal size $\sigma_L = 8\lambda$ is incident from the left boundary. All the other parameters are same as in the 1D case above.

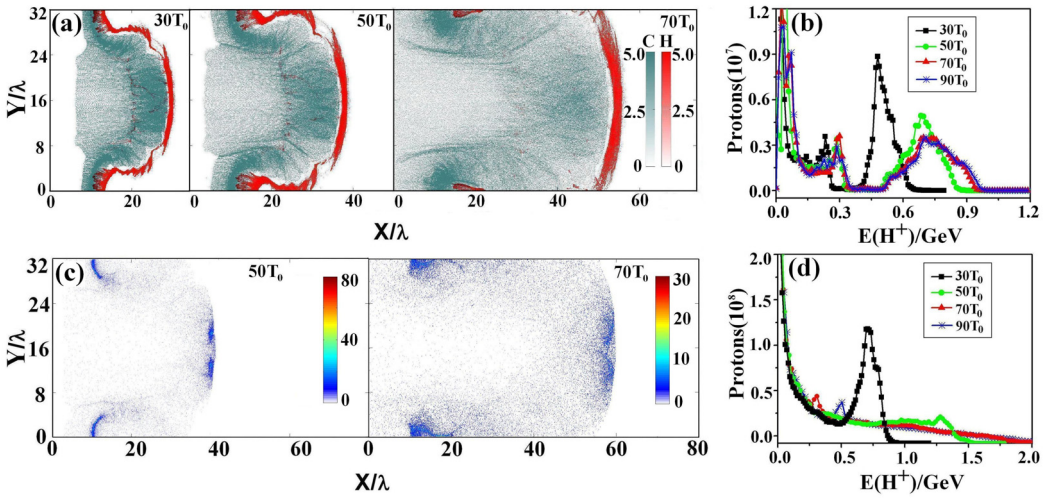

Figure 5.3: (a) Contours of protons and carbon ions in the 2D case at $t = 30T_0, 50T_0, 70T_0$. (b) Proton energy spectrum. For comparison, (c) shows the proton density distribution in a pure hydrogen foil and (d) corresponds to the energy spectrum evolution.

Fig. 5.3(a) shows the space distribution of carbon ions and protons at different times. In each frame, the teal color marks the carbon ions and the red shows the protons. Obviously, the carbon ions behave totally different as compared to the 1D simulations. They spread widely in space and do not form a clear bunch. On the contrary, the protons from the center part of the foil always ride on the carbon ion front and form a compact bunch. The sharp front separating the two species is well defined and remains stable even after the laser-foil interaction ends. We can get a further understanding of the acceleration from the phase space distribution, as displayed in Fig. 5.4(a, b). On the one hand, the carbon ions evolve into a wide cloud in space. On the other hand, their front trails the protons so that the gap between the two species is always small. The protons show a clear spiral structure, like a "matchstick", which coincides with the 1D simulations above.

Fig. 5.3(b) shows the proton energy spectrum. As expected, the peak is well pronounced and the dispersion is suppressed. The peak energy evolution is also in accordance with the predication of the 1D RPA model (not shown here). Fig. 5.4(c, d) plots the ion energy-divergency distribution at $t = 30T_0$. The high quality proton bunch with energy ~500 MeV and opening angle $\sim 5.5^\circ$ forms and persists in time even after the laser-foil interaction ends.

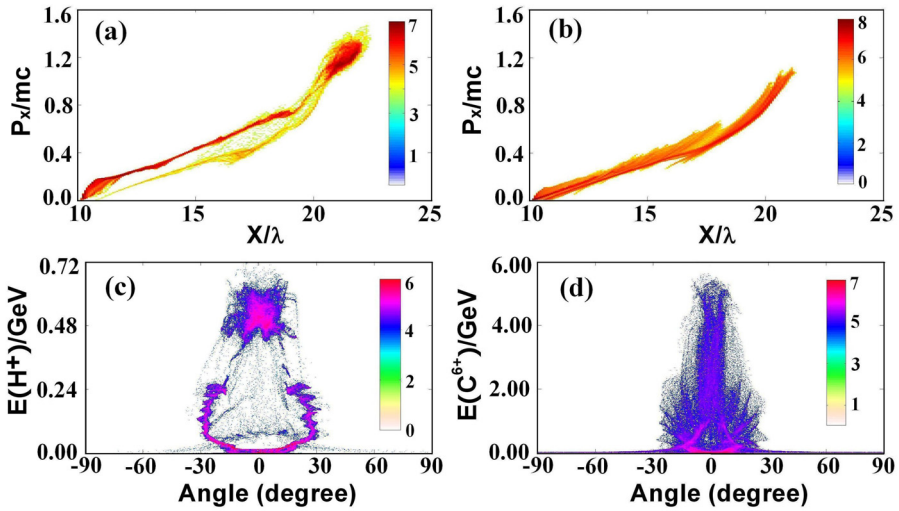

Figure 5.4: Phase space of (a) protons and (b) carbon ions at $t = 30T_0$. Frame (c) and (d) show the proton and carbon ion energy distributions as a function of the divergency angle at $t = 30T_0$.

Now we compare the stable multi-component foil case with a pure proton foil case, where the RT instability is obvious as discussed in previous chapters. We again employ a matched SFT. All the parameters are same as above except $n_{\mathrm{H}} = 320n_c$ and the carbon ions are absent. Fig. 5.3(c) shows the proton density distribution in space. We can see that the foil disrupts gradually and two proton bunches with a lower density valley in the middle form. This is very characteristic for the RT instability driven by the laser radiation. For the underlying physics we will address later. Finally, the monoenergetic peak as observed initially in Fig. 5.3(d) lowers and disappears at the end.

5.3 Three-interface model

The stability of the proton acceleration in the 2D simulations can be attributed to two effects. First, the protons rapidly separate from the carbon ions and form a thin shell, which is a prerequisite for the stable proton acceleration. Such a separation of ion species can be understood within the 1D formalism developed in Ref. [97] and the 1D simulations above. Second, the heating of the carbon ions forms an extended cloud that prevents short-wavelength perturbations of the surface from feeding through into the thin proton shell.

We propose a simple three-interface model, as shown in Fig. 5.5(a), to explain the stabilization of the proton acceleration in this two-ion-species regime. In the accelerating reference

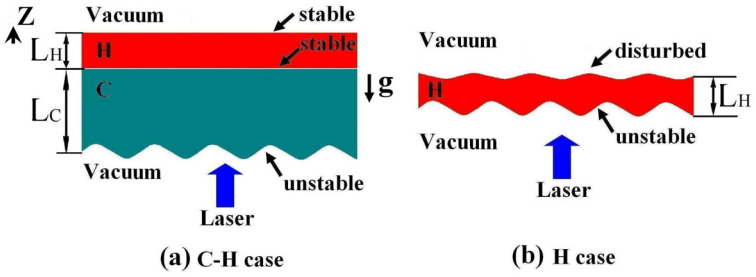

Figure 5.5: Schematic of the laser-foil interaction in (a) C-H case and (b) pure H case. Here, $L_{\mathrm{H}} \ll L_C$. In case (a), there are three interfaces: carbon-vacuum, carbon-proton, and proton-vacuum. Only the first interface is unstable. In case (b), both interfaces are finally unstable.

frame of the foil, the perturbation pressure p satisfies:

$$\frac{\partial^2}{\partial z^2}\delta p = -k_{\mathrm{RT}}^2 \delta p, \tag{5.1}$$

where k_{RT} is the wavenumber of the RT-unstable mode. Noting that δp is discontinuous across the unperturbed boundary, we obtain a solution $\delta p = A_i e^{-k_{\mathrm{RT}} z} + B_i e^{k_{\mathrm{RT}} z}$ away from interfaces, with A_i and B_i being the amplitude coefficients of the perturbation inside the layer consisting of the i'th species. In our case, both species have two interfaces: one with vacuum and one with the other species. For the carbon ions ($i = \mathrm{C}$), the only unstable interface is the carbon-vacuum boundary, where the laser pulse interacts directly with the carbon plasma. We derive from the model that the amplitude of the perturbation is exponentially decaying away from the unstable interface:

$$\frac{A_{\mathrm{H}}}{A_{\mathrm{C}}} \sim e^{-k_{\mathrm{RT}} L_{\mathrm{C}}}, \tag{5.2}$$

where L_{C} is the thickness of the carbon ion layer. In the simulations, L_{C} is several times longer than L_{H} so that the perturbation in the carbon layer would take much more time to grow (recall that the growth rate of the RT instability $\gamma \propto \sqrt{g/\lambda_{RT}}$, where g is the target's acceleration and λ_{RT} is the perturbation wavelength). The feed-through from the unstable carbon-vacuum interface to the proton layer is exponentially attenuated according to Eq. (5.2). This simple qualitative argument explains the stability of the sharp carbon-proton interface. For the thin proton layer, it is also stable because the protons are much lighter than the carbon ions. It is helpful to consider the problem from the purely hydrodynamic RT instability [114, 115] which arises when a light fluid is accelerated into a heavy fluid. In the simulations, we know that the forward protons are much lighter than the subsequent carbon ions so that the entire proton layer can keep stable. Eventually, the compact proton layer is free from the RT instability.

Now we compare the stable multi-component foil case with the pure hydrogen foil case, where the RT instability is obvious as shown in Fig. 5.3(c,d). Using the linear stability theory

of the accelerated foil [116], the growth time of the perturbation in the relativistic limit can be derived as following

$$\frac{\tau_{RT}}{T_0} = \frac{\sqrt{2}}{6}\sqrt{\frac{m_\mathrm{e}}{m_i}\frac{n_c}{n_i}\frac{\lambda}{L}}\left(\frac{\lambda_{RT}}{\lambda}\right)^{3/2} a, \tag{5.3}$$

Taking into account $\lambda_{RT} \simeq \sigma_L = 8\lambda$ and $L = 0.1\lambda$ in our case, we estimate that the time scale of the instability should be $2.2T_0$. Such a short-wavelength perturbation grows very fast so that it reaches the other side of the foil soon, as shown in Fig. 5.5(b). Finally, both interfaces are unstable and the entire target collapses quickly. Fig. 5.3(d) shows the proton energy spectrum. Although an energy peak is observed initially, it lowers gradually and disappears at $t = 45T_0$, leaving a quasi-exponential spectrum. In fact, most single-ion foils in this regime show a similar result [22, 64, 83, 86, 87, 89, 90]. The main issue is the fast growth of the short-wavelength perturbation at the unstable interface.

5.4 3D simulations

Finally, 3D simulations are performed to check the robustness of the stable acceleration mechanism. To save the computational time, the 3D simulation box is $40\lambda \times 25\lambda \times 25\lambda$, sampled by $4000\times200\times200$ cells. Each cell contains 27 particles initially. The ultra-thin SFT is composed of fully ionized carbon ions and protons with the density ratio $n_\mathrm{C} : n_\mathrm{H} = 4 : 1$. Periodic boundary conditions for particles and absorbing boundaries for fields are applied. The total laser energy is $\sim 500J$ and the duration is 33fs. All other parameters are same as in the case B except $\sigma_T = 5\lambda$ to match the laser focal spot $\sigma_L = 6\lambda$.

Fig. 5.6(a,b) illustrates the density distribution of protons and carbon ions at $t = 40T_0$. We can see a clear compact proton bunch with a few nano-Coulomb riding on the front of the carbon ions, which agrees well with the 2D simulation results above. The carbon ions spread extensively in space. This should be attributed to multi-dimensional effects, e.g., the fast-growth of the RT instability in the carbon ion layer as discussed above. In Fig. 5.6(c), we present the ion energy spectra at $t = 40T_0$. As expected, we observe a clear monoenergetic peak for protons. The peak is well maintained for a very long duration even after the laser-foil interaction ends. On the contrary, the spread carbon ions show a quasi-exponentially decaying in the energy spectrum. The cut-off energy of the carbon ions is almost same as the peak energy of the protons, as observed in the 2D cases. It indicates that the carbon ion front indeed trails the proton layer during the acceleration. We also find that there is another small energy peak for protons in the energy spectrum. By analyzing the ion energy distributions in space, we find that the protons with energy $\sim$ 280 MeV are situated in the vicinity of the carbon ion front. We believe it is due to the incomplete separation of the protons from the heavier

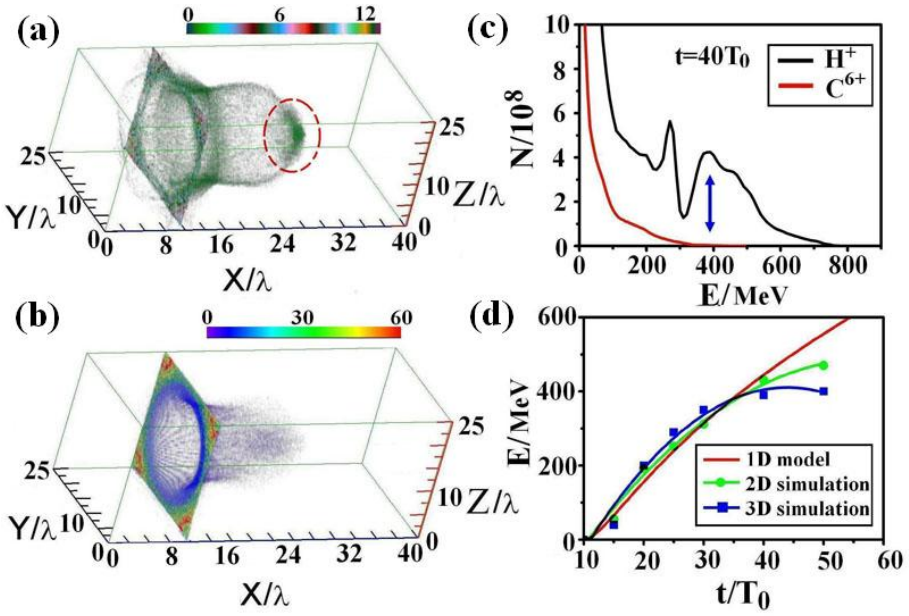

Figure 5.6: Density contours of (a) protons and (b) carbon ions in 3D simulations at $t = 40T_0$. (c) Energy spectra of protons and carbon ions. (D) Proton peak energy evolution in both 2D and 3D cases.

carbon ions in the 3D case. Fig. 5.6(d) presents the proton peak energy evolution both in the 2D and 3D simulations. Overall, 3D simulation results fit well with the 1D model marked by the red curve and the 2D simulations by the green curve. This demonstrates the domination of the RPA mechanism. The yielded proton beam with the peak energy ~ 400 MeV may have diverse potential applications in the future, such as in medical therapy of deep seated tumors and in the development of future compact ion accelerators.

5.5 Laser and foil parameter effects on the proton acceleration

Both 2D and 3D simulations demonstrate the feasibility of the two-ion-species SFT scheme for stable proton acceleration in the light-sail regime. In the following, we consider the effects of the laser intensity, ion density ratio, and ion charge-to-mass ratio on the ion acceleration. For simplicity, we only perform 2D simulations to save the computation time but the results are also valid for 3D cases.

5.5.1 Penetration of the laser pulse on the foil

Two basic cases are first investigated with 2D simulations. In the case A, the simulation box is $X \times Y = 50\lambda \times 50\lambda$, sampled by 10000×5000 cells. Each cell contains 100 numerical macro-particles in the plasma region. The foil is initially located at $x = 10\lambda$ with parameters $l_0 = 0.1\lambda$, $l_1 = 0.05\lambda$, and $\sigma_T = 7\lambda$. Both species have the same particle density $n_{\mathrm{C}} = n_{\mathrm{H}} = 45.71 n_c$, which corresponds to the electron density $n_{\mathrm{e}} = 320 n_c$ ($\sim 3.5 \times 10^{23}/\mathrm{cm}^3$). A circularly polarized Gaussian laser pulse with focal size $\sigma_L = 8\lambda$ is incident from the left boundary. The laser duration is $\tau_L = 10T_0$ ($\sim 33\mathrm{fs}, 1T_0 - 8T_0 - 1T_0$). All other parameters are same as above.

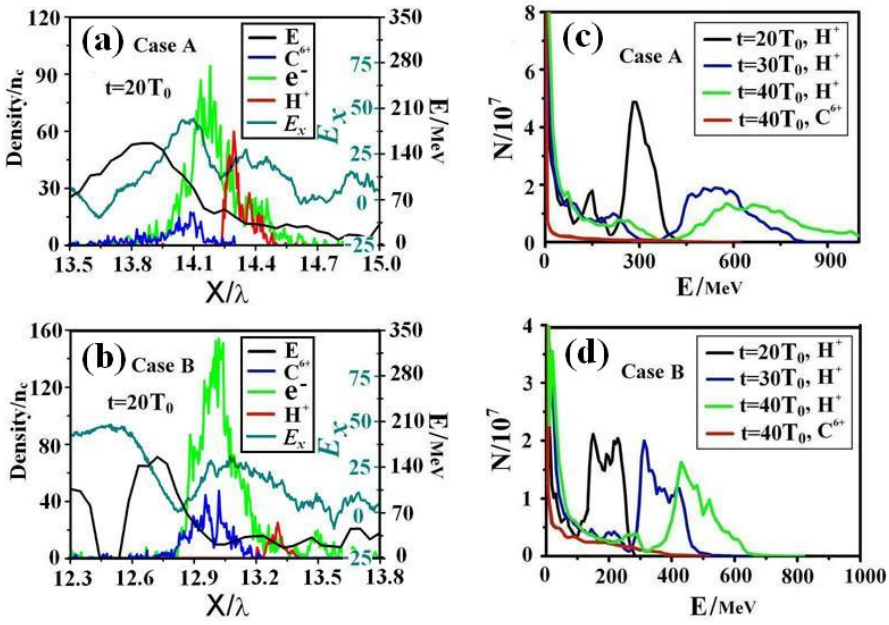

Figure 5.7: Particle density distributions and the electron energy distribution as well as the accelerating fields E_x on the laser axis at $t = 20T_0$ in the (a) case A and (b) case B. Energy spectrum evolutions of the protons and carbon ions in the (c) case A and (d) case B.

Fig. 5.7(a) shows the detailed ion acceleration process. We again find that the protons move to the front of the heavier carbon ions. Such a separation is determined by the balance between the inertial and the electrostatic forces. The sharp front separating the two species and trailing the proton beam is well defined, as shown by the sharp boundary as displayed in Fig. 5.7(a).

We observe a clear RT-like instability in the case A. A typical "λ structure" [101] can be recognized in both the ion and electron density distributions [101]. The proton layer is strongly effected, which can be understood by considering the relativistic laser transparency of

the foil. In view of the ultra-low thickness of the foil in this case, the electromagnetic wave can partially penetrate the foil and interact with both ion species. This would seed RT instability at the proton-carbon interface. Gradually, the protons also suffer from the RT instability and show an obvious "λ structure". However, the trailing carbon ion front contributes to slowing down the local bunching of the protons and hence suppresses the transverse proton-RT instability. This is the reason why we still observe a semi-stable layer of protons in front of the carbon ions at a later time, e.g., $t = 30T_0$, though the surface of the layer is strongly corrugated. Fig. 5.7(c) shows the ion energy spectra at $t = 20T_0$, $30T_0$, and $40T_0$. Although a monoenergetic peak is observed at the very beginning, it becomes broader after $t = 30T_0$. Eventually, the protons also evolve into a cloud in space.

In view of the negative effects of the laser penetration, we propose using a moderate intensity laser pulse or a higher electron density foil to avoid the RT-like instability from affecting the proton layer. We estimate the critical laser intensity for this case by

$$a \sim \pi \frac{n_{e1}}{n_c} \frac{l}{\lambda}, n_{e1} = Z_{\mathrm{C}} \times n_{\mathrm{C}} \tag{5.4}$$

For comparison, we perform another simulation to show improved proton beam acceleration. In case B, the foil is composed of fully ionized carbon ions and protons with number density ratio $n_{\mathrm{C}} : n_{\mathrm{H}} = 4 : 1$. The electron density is increased to $n_{\mathrm{e}} = 500 n_c$ ($\sim 5.5 \times 10^{23}/\mathrm{cm}^3$) so that the foil is opaque to the incident laser pulse. All the other parameters are same as the case above. Fig. 5.7(b,d) shows the simulation results. In this case, the foil is well maintained for a much longer time as compared to the case A. The protons again form a distinct layer from the carbon ions and always ride on the carbon ion front. The laser pulse does not penetrate the foil and the radiation pressure mainly acts on the carbon ion layer. As a consequence, the proton layer is kept stable and is less affected by the evolution of the RT instability in the carbon layer. Compared to the case A, the sharp front separating the two species is much more smooth. Most electrons are moving together with the carbon ions, and the spread carbon ions act as a "buffer" for proton acceleration. This leads to a more stable acceleration structure, which is verified by the energy spectra in Fig. 5.7(d). We can see that the energy peak is more pronounced and the spread (FWHM) is about 20% at $t = 30T_0$, which is only half of that in the case A. Meanwhile, we find that the cut-off energy of the carbon ions always peaks the proton spectrum in the both case A and B.

It is interesting to note that a similar phenomenon was also observed in Ref. [117, 118], where mass-limited targets were studied and the results were interpreted as the direct Coulomb explosion (DCE). In that regime, electrons are overtaking ions as flying compact layers and the return current is inhibited when mass-limited targets are used. The accelerating field from Coulomb explosion of the heavier ions accelerates the lighter protons forward. In our case, however, the laser radiation pressure is dominating the proton acceleration because the

Table 5.1: Case list

Label	Composition	n_{C}:n_{H}	n_{e}
Case A	C^{6+}, H^{+}	1:1	$320n_c$
Case B	C^{6+}, H^{+}	4:1	$500n_c$
Case C	C^{6+}, D^{+}	4:1	$500n_c$
Case D	C^{6+}, T^{+}	4:1	$500n_c$
Case E	H^{+}	-	$500n_c$
Case F	C^{5+}, H^{+}	4.8:1	$500n_c$
Case G	C^{3+}, H^{+}	8:1	$500n_c$

Note: Case E is a pure hydrogen foil. For all the cases, both the laser parameters and foil thickness are same.

electrons always accompany both the carbon ions and protons. The bulk electrons enable a good screening of the electrostatic field and thus effectively prevent the ions from Coulomb explosion. The foil is accelerated forward as a compact dense quasi-neutral plasma until the carbon ions evolve into a cloud in space. However, we find that Coulomb explosion of the proton layer becomes significant later. The peak proton energy and the cut-off energy of the carbon ions continue to increase slowly after the laser-foil interaction ends. After the interaction, e.g., $t = 35T_0$, the carbon ions evolve into a cloud in space and the electrons are extensively heated, and expand with the carbon ions. Finally, the Debye length of the electrons may become larger than the proton layer thickness. Assuming the thickness of the proton layer being $l_{\mathrm{H},0}$ initially and $l_{\mathrm{H},t}$ at a specific time point, we have $\pi\sigma_L^2 n_{\mathrm{H},0} l_{\mathrm{H},0} = \pi\sigma_T^2 n_{\mathrm{H},t} l_{\mathrm{H},t}$ according to the particle number conservation. We can then get a condition for the onset of Coulomb explosion in this two-ion-species regime as follows

$$T_{\mathrm{e},t}[\mathrm{MeV}] > 8 \times \left(\frac{n_{\mathrm{H},0} l_{\mathrm{H},0}}{n_c \lambda}\right)^2 \frac{n_{\mathrm{e},t} n_c}{n_{\mathrm{H},t}^2} \tag{5.5}$$

where $T_{\mathrm{e},t}$ and $n_{\mathrm{e},t}$ are the electron temperature and density in the proton layer at the time t, respectively. At the post-interaction stage, the electron heating is significant so that the electron temperature is much larger than the value by Eq. (5.5), and Coulomb explosion takes place. For example, at $t = 35T_0$ in the case B, the proton layer thickness is about $l_{\mathrm{H}} = 1\mu\mathrm{m}$ and the averaged Debye length of the electrons in the proton layer is $d = 1.6\mu\mathrm{m}$. In this situation, the effects of Coulomb explosion should be taken into account [119, 120]. We have to note that, Coulomb explosion is undesirable because it broadens the final proton energy spectrum, though the ion energy can be increased slightly.

5.5.2 Hydrogen mass: H_1^1, D_1^2, and T_1^3

To evaluate the effects of ion charge-to-mass ratio on the ion acceleration, we also perform simulations (see Table 5.1) where we employ carbon-deuterium (C-D foils, case C, $Z_D/m_D = 1/2$) and carbon-tritium (C-T foils, case D, $Z_T/m_T = 1/3$) instead of hydrocarbon (C-H foils, case B, $Z_H/m_H = 1/1$). All other parameters are same as in the case B. The simulation results are depicted in Fig. 5.8. As discussed above, the separation of ion species depends on the ion charge-to-mass ratio. For the C-D foil, both the carbon ion and the deuterium have same Z_i/m_i and they therefore do not separate from each other (see Fig. 5.8(b)). The laser pulse pushes both of them forward together. In this case, it is expected that the RT instability shall deteriorate both ion energy spectra (see Fig. 5.8(d)). For the C-T foil, we do observe ion separation initially because the carbon ions have a larger Z_i/m_i and hence they move to the front of the tritium. However, the tritium is initially compressed into a very thin layer, which leads to fast-growth of the perturbation at the vacuum-tritium interface. The instability soon reaches the tritium-carbon interface and pollutes the front carbon ion beams. Obviously, such a structure is unstable, and we do not observe a mono-energetic beam as seen in Fig. 5.8(d).

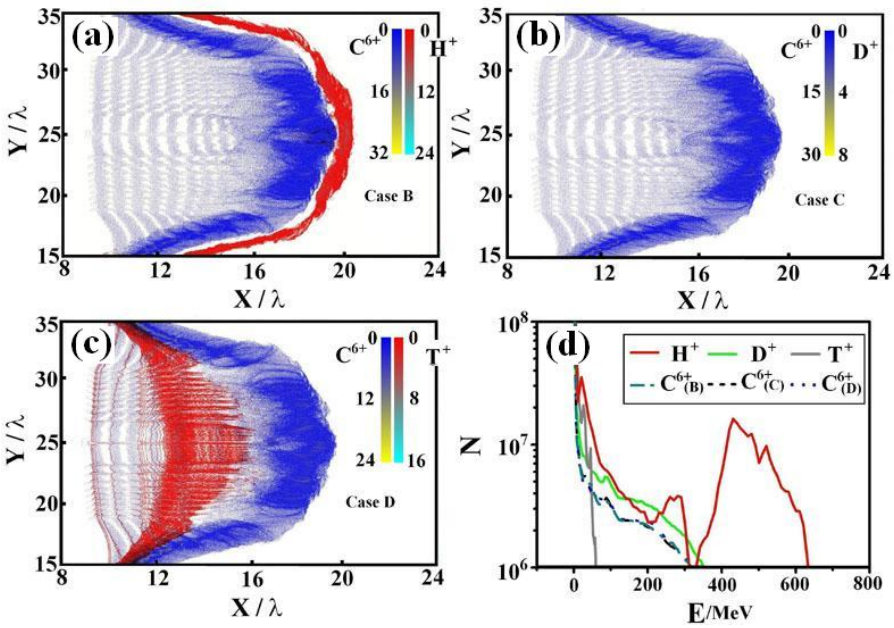

Figure 5.8: Ion density distributions in the (a) case B (C-H foil), (b) case C (C-D foil), and (c) case D (C-T foil) at $t = 30T_0$. (d) Ion energy spectra in the case B, C, and D at $t = 40T_0$.

5.5.3 Carbon ion charge

We also investigate effects of the charge state of carbon ions on the stability of the proton acceleration. In the simulations, we keep the proton density same but vary the charge on carbon ions. C^{5+} (case F, $Z/m = 1/2.4$) and C^{3+} (case G, $Z/m = 1/4$) are taken into account. For comparison, a pure hydrogen SFT (case E) is also considered. All other parameters are same as that of the case B. The simulation results and the proton energy spectra are presented in Fig. 5.9.

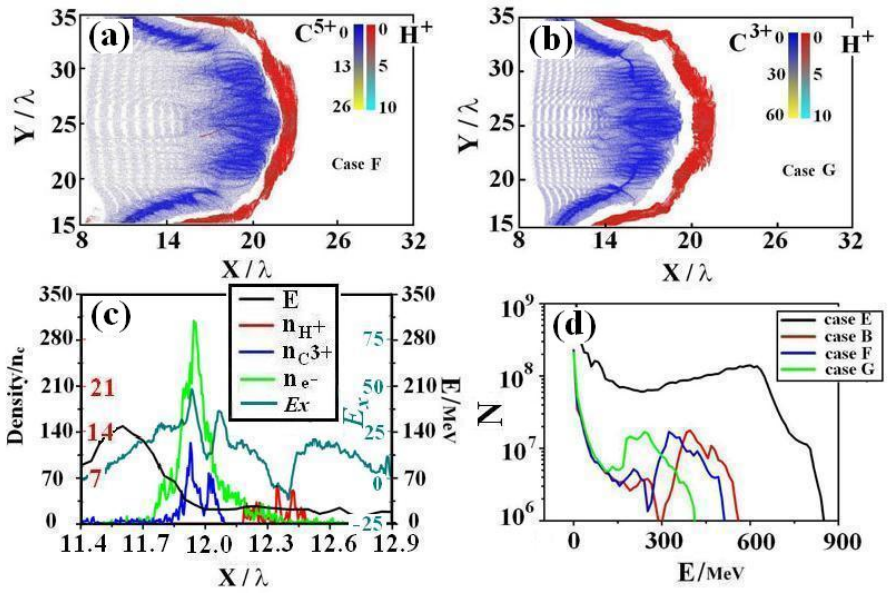

Figure 5.9: Density distributions of protons and carbon ions ((a) H^+, case E, (b) C^{5+}, case F, and (c) C^{3+}, case G.) at $t = 35T_0$. (d) Proton energy spectra in the case B, E, F, and G at $t = 35T_0$.

It is interesting to find that with the decrease of the carbon ion charge state, the gap between the carbon ions and protons grows, which leads to poorer monochromaticity of the proton energy spectrum. This implies that the RT instability is much more severe in the case of the lower charge state of the carbon ions. This effect is beyond the scope of the current three-interface model and shall be studied further.

Besides, we believe that Coulomb explosion of the proton layer also plays a role in case G because most electrons are with the carbon ions, which are far away from the protons. The wide gap prevents the electrons from neutralizing the proton layer. Finally, the electron density becomes very low in the proton layer. According to Eq. (5.5), the electron temperature for the onset of Coulomb explosion is reachable. For example, at $t = 20T_0$, the proton layer thickness, $l_H = 0.3\mu m$, is smaller than the averaged Debye length of the electrons in the

proton layer, $\lambda_D = 0.4\mu\mathrm{m}$. As shown in Fig. 5.9(c), we observe a clear dipped accelerating field with a negative component in the proton layer, which is a clear signature of Coulomb explosion. Gradually, the protons self-expand in space and the energy spectrum broadens. This is different from the case B where Coulomb explosion might take place after the interaction ends. Additional simulations show that when the charge state of the carbon ions is lower than 3, both the RT instability and Coulomb explosion of the proton layer become violent enough to destroy the monoenergetic proton beam. However, in the relativistic regime the laser pulse is powerful enough to fully ionize the carbon atoms. We therefore believe it is possible to observe stable proton acceleration in the in experiments.

Besides, we believe that a smaller transverse size of the foil would benefit the stabilization of the proton acceleration in this two-ion-species regime. In the simulations, we apply a periodic boundary condition in the transverse direction and use the transverse size of the simulation box $Y = 50\lambda$. When we decrease this size to $Y = 25\lambda$, we observe a considerable suppression of perturbation penetration into the target.

5.6 Conclusion

In conclusion, we investigated detailed ion acceleration from an ultra-thin hydrocarbon foil by the use of multi-dimensional PIC simulations. A stable compact proton beam acceleration was observed, for the first time, in the 3D geometry. This should be attributed to two effects: ion species separation and heavier ion spreading in space. The laser pulse does not penetrate the foil and the radiation pressure mainly acts on the carbon ion layer. The carbon ions act to buffer the compact proton layer from the RT-like instability. The proposed three-interface model well describes the simulation results and is further supported by simulations of various compound foils, such as C-D, C-T, and pure hydrogen foils. It is also found that with the decrease of the carbon ions charge state, both the RT instability and Coulomb explosion become increasingly violent and tend to degrade the monoenergetic proton beam. Finally, the robustness of the stable two-ion-species regime is checked by the full 3D simulations.

With the development of the nano-technology [121], ultra-thin foils could be available soon in experiments. Compared to the normally used two-layer foils, they are much easier to fabricate. Benefiting from the state-of-the-art lasers such as HiPER and ELI, we believe that the stable acceleration mechanism described above will be experimentally demonstrated soon and has a great potential for applications in science and medicine.

Chapter 6

Radiation reaction effects and betatron-like hard X-ray emission

In previous chapters, special attention was paid to the ion acceleration in the light-sail regime. The research on the accompanying electron acceleration and revelent dynamic behaviors, such as longitudinal time domain and transverse oscillation, is very little, which is, contrarily, a prerequisite to correctly understand the underlying physics in the light-sail regime. For high energy particles undergoing acceleration, self-radiation is concomitant. The radiation reaction effects should be considered when the radiation damping force is comparable to the external one. For the above-mentioned processes for particle acceleration, electrons endure intensive acceleration. When the laser intensity increases further, the radiation reaction cannot be neglected. Naumova *et al.* have studied the radiation reaction effect on the laser hole boring process and pointed out that it plays a positive role as it allows one to maintain the electron thermal energy on a relatively low level and prevents the electron backward motion through the pulse [104].

In this chapter, we take into account the radiation reaction effect on the ion acceleration. For simplicity, we modify the PIC code according to the momentum conservation law. At any given time, we suppose that the radiation spectrum is synchrotron-like and the relativistic electrons emit radiation along their momentum direction. By using the modified code, we study the electron dynamics in the light-sail regime and observe the generation of GeV spiral electron bunches with an obvious attosecond structure. Such energetic spiral electron bunches would be of great interest for emission of efficient betatron-like X-ray and even γ burst, which might have diverse applications, e.g., in understanding the physics of laser-plasma interaction process on a femtosecond scale.

6.1 Radiation damping in the relativistic case

When a charged particle (ion or electron) is accelerated, it creates a radiation field that shall act back on the particle itself [122]. This self force is called radiation force or friction force, which has been extensively studied and discussed together with almost one century's debate on this question [111]. For a simple introduction to this question, let's recall the calculation of radiation damping in the relativistic case derived about 70 years ago by Landau and Lifshitz [123]. Assuming a single charged particle, we can write the motion equation of the particle using a four-vector g^i as

$$mc\frac{du^i}{ds} = \frac{e}{c}F^{ik}u_k + g^i, \tag{6.1}$$

$$\frac{dx^i}{ds} = u^i, \tag{6.2}$$

where m, e, c are the particle mass, charge and the speed of light, respectively. $u_i = (\gamma, \mathbf{p}/mc)$ is the four-velocity and $F_{ik} = \partial_i A_k - \partial_k A_i$ is the electromagnetic field tensor with A_i being the electromagnetic four-vector and $i = 0, 1, 2, 3$. There has been a long search for an improved classical equation that can comprehensively describe the motion of a radiating charge in the prescribed laser electromagnetic field [110]. In the Lorentz-Abraham-Dirac (LAD) form [107], we consider the requirement $g^i u_i = 0$ for any force four-vector and find g^i is given by

$$g^i = \frac{2e^2}{3c}\left(\frac{d^2u^i}{ds^2} - u^i u^k \frac{d^2u_k}{ds^2}\right), \tag{6.3}$$

As we know, the above LAD form of the friction force Eq.(6.3) poses nonphysical "runaway" solutions (self-accelerating of electrons). Many studies have contributed to pursing an accurate solution without this nonphysical effect over the last decades.

In accordance with the equations of motion, we can directly express d^2u^i/ds^2 in terms of the field tensor of the external field acting on the particle:

$$\frac{du^i}{ds} = \frac{e}{mc^2}F^{ik}u_k, \tag{6.4}$$

$$\frac{d^2u^i}{ds^2} = \frac{e}{mc^2}\frac{\partial F^{ik}}{\partial x^i}u_k u^l + \frac{e^2}{m^2c^4}F^{ik}F_{kl}u^l, \tag{6.5}$$

Here, the product of the tensor $\partial F^{ik}/\partial x^l$ is antisymmetric in the indices i,k, and symmetric tensor $u_i u_k$ gives identically zero. Finally, we obtain the friction force in the so-called Landau-Lifshitz (LL) form (also known as the reduced LAD equation)

$$g^i = \frac{2e^3}{3mc^3}\frac{\partial F^{ik}}{\partial x^l}u_k u^l - \frac{2e^4}{3m^2c^5}F^{il}F_{kl}u^k + \frac{2e^4}{3m^2c^5}\left(F_{kl}u^l\right)\left(F^{km}u_m\right)u^i, \tag{6.6}$$

Calculating the space components of the four-vector above, we can get the three-dimensional expression for the damping force in the relativistic case with respect to laboratory frame [123]

$$\mathbf{f}_R = \frac{2e^3}{3mc^3}\gamma\left[\left(\frac{\partial}{\partial t} + \mathbf{v}\cdot\bigtriangledown\right)\mathbf{E} + \frac{1}{c}\mathbf{v}\times\left(\frac{\partial}{\partial t} + \mathbf{v}\cdot\bigtriangledown\right)\mathbf{H}\right] \tag{6.7}$$

$$+\frac{2e^4}{3m^2c^4}\left[\mathbf{E}\times\mathbf{H} + \frac{1}{c}\mathbf{H}\times(\mathbf{H}\times\mathbf{v}) + \frac{1}{c}\mathbf{E}(\mathbf{v}\cdot\mathbf{E})\right] \tag{6.8}$$

$$-\frac{2e^4}{3m^2c^5}\gamma^2\mathbf{v}\left[\left(\mathbf{E} + \frac{1}{c}\mathbf{v}\times\mathbf{H}\right)^2 - \frac{1}{c^2}(\mathbf{E}\cdot\mathbf{v})^2\right], \tag{6.9}$$

where $\gamma = [1 - (v^2/c^2)]^{-1/2}$ is the Lorentz factor. Obviously, the third term of the radiation damping force (Eq. 6.9) is proportional to γ^2, which dominates over the preceding one ($\propto \gamma$). Thus, the motion equation of the charged particle in external laser fields can be expressed as [113]

$$\frac{d\mathbf{p}}{dt} = \mathbf{f}_L - \mathbf{f}_R \tag{6.10}$$

$$\mathbf{f}_L = -(\mathbf{E} + \mathbf{v}\times\mathbf{B}) \tag{6.11}$$

$$\mathbf{f}_R = \left(\frac{4}{3}\pi\frac{r_e}{\lambda}\right)\gamma^2\left[\mathbf{E}^2 - (\mathbf{v}\cdot\mathbf{E})^2 + \mathbf{v}^2\mathbf{B}^2 - (\mathbf{v}\cdot\mathbf{B})^2 - 2\mathbf{v}\cdot(\mathbf{E}\times\mathbf{B})\right]\mathbf{v}, \tag{6.12}$$

where $r_e \equiv e^2/mc^2 = 2.8\times10^{-9}\mu\mathrm{m}$ is the classical electron radius.

The LL equation is equivalent to the LAD equation up to the first order, which avoids the nonphysical effect and has analytical solutions. However, we have to note that the above approach is classical and quantum electrodynamic effects are neglected. The LL radiation friction force being a perturbation is valid based on the assumption that there exists a frame of reference, where the friction force is small compared to the Lorentz force. However, it is not easy to prove the existence of such a reference frame. Besides, the equation of motion, energy and momentum are also not conserved exactly for a single electron in the LL form [113]. A rigorous derivation considering energy and momentum conservation should be given. Therefore, many studies contributed to this problem in the last decades. Here, we try to treat the problem from a different angle of view to pursue an approximation to the solution.

6.2 Synchrotron radiation damping

Before showing the effects of the radiation damping in this new approach, we first check the threshold of the laser intensity for the radiation reaction effects to become important. For an electron with velocity $v \sim c$, one can get the radiation power $P(t)$ at the local radiation time t as

$$P(t) = \frac{2e^2}{3m^2c^3}\left(\frac{d\mathbf{p}}{dt}\right)^2, \tag{6.13}$$

when $\mathbf{a}_{acce}||\mathbf{v}$, and

$$P(t) = \frac{2e^2}{3m^2c^3}\left(\frac{d\mathbf{p}}{dt}\right)^2\gamma^2, \tag{6.14}$$

when $\mathbf{a}_{acce} \perp \mathbf{v}$. Here, $\mathbf{p}$ is the electron momentum, γ is the relativistic factor, and e and m are the charge and mass of electron, respectively. So the radiation due to the transverse acceleration is γ^2 stronger than the one due to the longitudinal acceleration. For the synchrotron-like radiation, the radiation is mainly along the direction of electron motion and concentrated within an angle of θ with $\Delta\theta \sim 1/\gamma$.

Based on the above knowledge, in the PIC code, we consider the radiation only due to the transverse acceleration and only the electrons whose energies $\gamma \geq 5$ are assumed to contribute to the radiation. To simulate the damping effects, we suppose that, at any given moment in time, the electron radiation spectrum is synchrotron-like [124] and an electron gets a momentum variation in the opposite direction of the radiation because of momentum conservation. By the use of the normalized variables as in the PIC code ($p \sim p/mc$, $t \sim t/T_0 = \omega_0 t/2\pi$), from Eq. (6.14) we can get the momentum variation rate as

$$\frac{dp_{rad}}{dt} = \frac{2e^2}{3mc^2\lambda}\left(\frac{dp}{dt}\right)^2\gamma^2, \tag{6.15}$$

In one simulation step it changes to

$$\left(\frac{dp_{rad}}{dt}\right)dt = n_{ph}\frac{\omega_c}{\omega_0}\frac{E_{ph0}(eV)}{5.11\times10^5}, \tag{6.16}$$

where h is the Planck constant, ω_0 is the laser frequency and E_{ph0} is the photon energy of the laser pulse. For simplicity, here we have also assumed that the radiation is in the form of photons. The critical frequency ω_c is given by the relation $\omega_c = (3/4\pi)\gamma^2|\Delta P_\perp|/(dt)$; $\Delta P_\perp$ is the variation in transverse electron momentum force during the time step of dt. The corresponding photon number is $n_{ph} = 8\pi e^2 dp/9hc$. The radiation reaction force on the

electron can thus be written as

$$f_C = \frac{dp_{rad}}{dt} = 1.88 \times 10^{-9}\gamma^2 \left(\frac{dp}{dt}\right)^2 / \lambda(\mu\mathrm{m}), \tag{6.17}$$

The reaction force points in the opposite direction of the electron motion. In order to demonstrate the validation of the approach above, we compare the friction force above with one derived by Sokolov *et al.* [125] where a modified LAD model was proposed that does not contradict quantum electrodynamic (QED) fundamentals. We notice that the force we used here is same as the main radiation reaction force in Eq.(12) in Ref. [125]. Generally, although our method is based on the simple momentum conservation and the assumption of synchrotron-like radiation frequency, it approximately equals this modified LAD model [126]. However, it is relatively easy to implement in the existing PIC code.

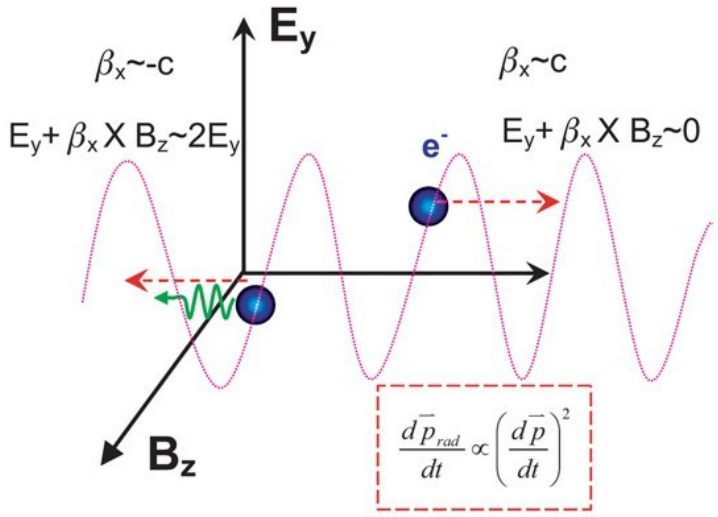

Figure 6.1: Schematic map of laser electron interaction. Here a linearly polarized laser pulse is used.

In our PIC code, we follow trajectories of each electron and calculate the emission during the interaction. We calculate the damping effects by considering the electron's recoil due to the emitted radiation. The recoil contribution is added in the code after the normal push by the Lorentz force on the electrons. At the same time, we record the radiated photon frequency and number for final spectrum analysis. The radiation we record in every simulation step is the photons radiated at the local time of radiation, not that at the observation time.

Besides the radiation reaction force, the electron also feels the external force as (here we

show only the transverse force due to the laser field)

$$\frac{d\mathbf{p}_{Laser_\perp}}{dt} = 2\pi q_e(\mathbf{E} + \frac{\mathbf{v}}{c} \times \mathbf{B})_\perp = -2\pi(\mathbf{E}_\perp + \frac{\mathbf{v}_x}{c} \times \mathbf{B}_\perp), \tag{6.18}$$

where **E** and **B** are the intensities of electric and magnetic fields normalized by $m\omega_0 c/e$. We can get the threshold of the laser intensity for the radiation damping effect by using

$$\frac{d\mathbf{p}_{rad}}{dt} \sim \frac{d\mathbf{p}_{Laser_\perp}}{dt}, \tag{6.19}$$

For a laser pulse, $|\mathbf{E}| = |\mathbf{B}| = a$. For an electron moving along with a linearly polarized laser pulse, we have

$$\gamma = \sqrt{1 + a^2} \approx a(a >> 1), \tag{6.20}$$

Here, $a = eE/m\omega_0 c$ is the normalized laser amplitude and γ is the Lorentz factor. To get a large radiation effect, we require $\gamma a \geq 8.47 \times 10^7$, and correspondingly the laser intensity should satisfy $a \geq 550$. For a $1\mu\mathrm{m}$ laser, this corresponds to $4.2 \times 10^{23}\mathrm{Wcm}^{-2}$, which is higher than the intensity attainable with the current laser systems. However, for an electron with a longitudinal velocity of $\beta_x \simeq 0$, the equation changes to $\gamma^2 a \geq 8.47 \times 10^7$. When the electron moves in the opposite direction of the laser pulse with the longitudinal velocity $\beta_x \simeq -1$, then the condition becomes $\gamma^2 a \simeq 4.23 \times 10^7$. That is, the threshold of a can be γ times smaller when the electrons with the same energy (γ) move backward (see Fig. 6.1). The reason is that the radiation force is proportional to the square of the acceleration force ($\mathbf{E} + \mathbf{v}_x/c \times \mathbf{B} \approx 0$). For the electrons moving forward, the transverse force they feel is about zero, so the radiation force is even smaller. However, for the electrons moving backward, the transverse acceleration force is about $4\pi q e\mathbf{E}$, so the radiation force is much larger.

As a primary result, we finally conclude that the radiation comes mainly from the electrons moving backward in the laser pulse and the radiation damping impedes this backward motion, which can reduce the particles' volume in the phase space and improve the ion acceleration energy and quality. These results are in excellent agreement with the subsequent simulations [112].

6.3 GeV spiral electron bunches generation and betatron-like hard X-ray emission

Previous studies have demonstrated the validation of the algorithm in the betatron radiation by the relevant experiments [127]. In the following, we use the modified code to study the electron dynamics in the light-sail regime. As we know, in a simple 1D model of the light-sail regime, the electrons move together in the longitudinal direction with the heavy protons at almost the same velocity v_p, as scaled by [23, 95]

$$\frac{v_p}{c} = 1 - [\varsigma(t) + \varkappa(t)]^{\frac{1}{3}} - [\varsigma(t) - \varkappa(t)]^{\frac{1}{3}}, \tag{2.7}$$

Considering the bulk mass of the ions, we generally assume that the ions move only in the laser direction and there is no transverse oscillation. However, the light electrons endure not only longitudinal acceleration by the laser radiation pressure, but also transverse oscillation because of the intense laser electric field $E_\perp$. For a linearly polarized laser pulse irradiating a droplet [128], the electron oscillation is well confined in the incident plane. However, the structure is unstable due to the strong electron heating and the bunch can propagate for a very short time ($\sim$ 40fs) with a few MeV energy and then dissipate in space. Instead, for a circularly polarized laser pulse in the light-sail regime, the electrons can be accelerated dramatically in the longitudinal direction according to Eq.(2.7) and therefore keep a much stable spiral structure in the transverse direction because of the higher electron energies ($\sim$ GeV) and significant suppression of electron heating.

We first operate full 3D simulations. In order to resolve the possible ultra-short time domain of the electron bunches in the 3D case, the simulation box is $X \times Y \times Z = 16\lambda_0 \times 15\lambda_0 \times 15\lambda_0$, which is sampled by $3200 \times 300 \times 300$ cells with 800 particles in each cell. The time step is $\triangle t = 0.0045T_0$ where $T_0 = \lambda_0/c = 3.3$fs is the laser cycle. A shift window is used to save the simulation time and the data space. A circularly polarized super-Gaussian laser pulse with transverse profile $a = a_0 exp(-r^8/\sigma_L^8)$ is incident from the left side of the simulation box onto a thin solid hydrogen foil, where $a_0 = 100$ and $\sigma_L = 4\sqrt{2}\lambda_0$. The laser pulse has a trapezoidal profile in time and the duration is $\tau_L = 12T_0(1T_0 - 10T_0 - 1T_0)$. The foil is initially located between $x = 5.0\lambda_0 - 5.1\lambda_0$ with the transverse size $8\lambda_0 \times 8\lambda_0$ which is a little smaller than the focal spot size (so-called "mass-limited" target). The plasma density is $n_\mathrm{e} = n_p = 320n_c$ with $n_c = m_\mathrm{e}\omega_0^2/4\pi^2$ the critical density and m_e the electron rest mass. Here, $a_0 = \pi n_\mathrm{e} L/(n_c\lambda_0)$ is well satisfied to get an optimal acceleration in the light-sail regime [97].

Fig. 6.2 shows the 3D multiplanar viewer of the laser mass-limited foil interaction. At the center of the simulation box, we can see a very clear rotation structure of the electrons around the proton bunch. It is the first time to observe such a compact attosecond structure with

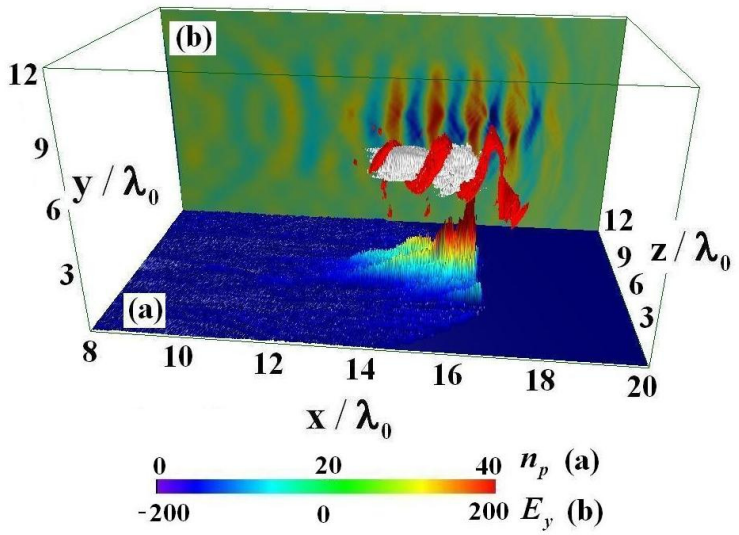

Figure 6.2: 3D multiplanar viewer of the laser-foil interaction. (a) Proton density projection in $x-z$ plane; (b) Transverse electric field E_y projection in $x-y$ plane.

electron density well above n_c in the light-sail regime. In fact, there are still several rotation rings in front of the proton bunch which are not shown in the figure due to the strong noise in the post-visualization code. For the ions, as expected we observe a monoenergetic proton bunch which has been reported in several previous work [13, 21, 23, 64, 86, 87, 90, 94, 95, 96]. At the beginning of the laser-foil interaction, electrons move in front of protons instantly because of the lower mass, $m_e \ll m_p$, and then the laser radiation pressure pushes the both forward as a whole. Gradually, the lateral laser pulse overtakes the mass-limited foil from the boundary. This overtaking electromagnetic wave wraps, confines, and compresses the foil into a "cluster-like" plasma so that its transverse size becomes much smaller than the laser focal spot. Obviously, such a tight self-organizing "cluster-like" bunch is very favorable for the generation of compact attosecond electron bunches because the strong electric field of the overtaking laser, $\mathbf{E}_\perp = \mathbf{E}_y + \mathbf{E}_z$, can accelerate them dramatically and directly in the transverse direction. In each laser cycle, the electrons in the originally compressed "cluster-like" plasma can be pulled out and move together with the laser electric field. Finally, we observe such a compact rotation structure in space as displayed in Fig. 6.2.

In order to get insight into dynamics of the electron acceleration, we perform 2D simulations with a longer laser duration and larger focal spot size but much faster computation. In the 2D case, the laser duration is $\tau_L = 22T_0(1T0 - 20T_0 - 1T_0)$ and the focal sport radius is $\sigma_L = 8\sqrt{2}\lambda_0$. The transverse foil size is $16\lambda_0$ and the simulation box is $X \times Y = 50\lambda_0 \times 30\lambda_0$. Fig. 6.3 shows the simulation results. Obviously, the slice structure with duration ~ 100as in Fig. 6.3(a) corresponds to the rotation rings as observed in the 3D case above. The overtaking

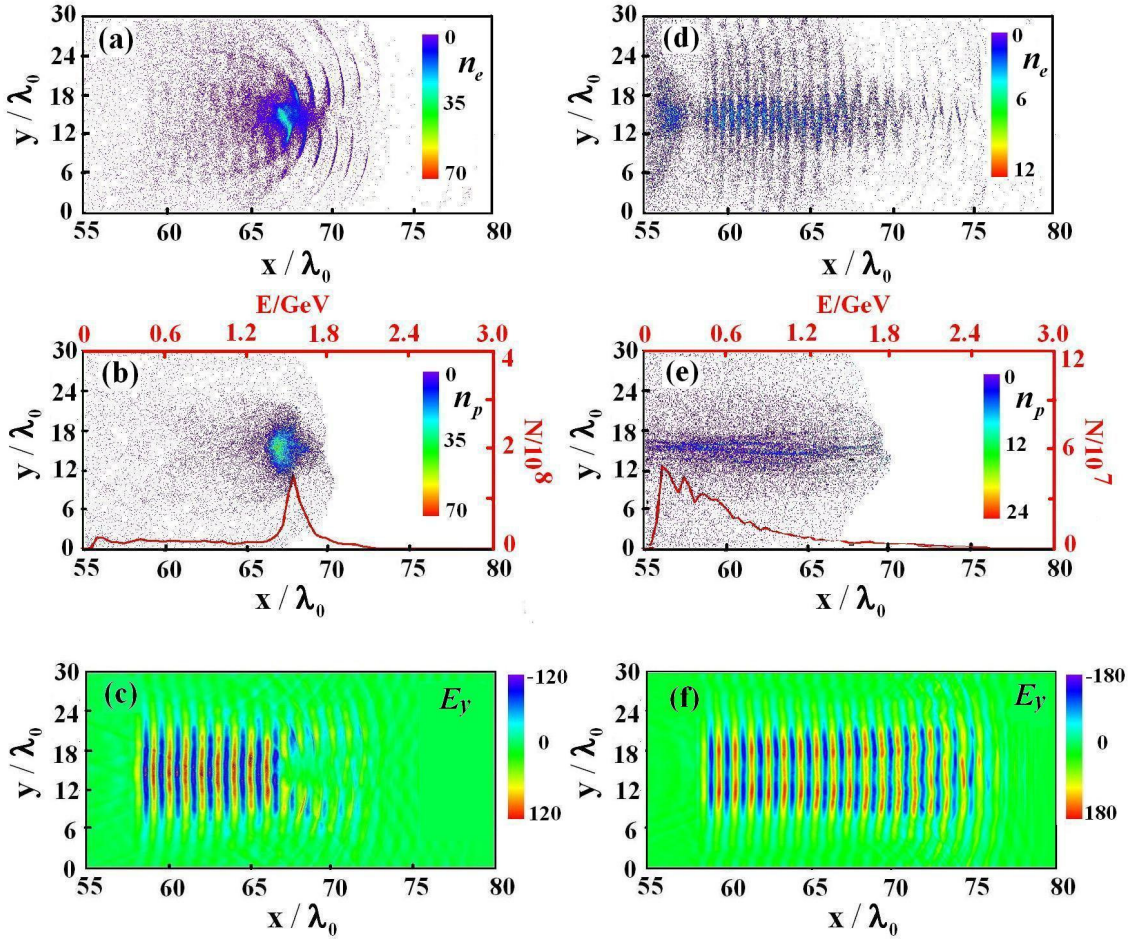

Figure 6.3: 2D simulations of the laser-foil interaction at $t = 80T_0$. The frames (a, b, c) are, respectively, the distributions of the electron density, proton density, and electric field E_y for circularly polarized laser pulse. The frames (d, e, f) represent the same but for linearly polarized laser pulse.

laser pulse from the boundary of the mass-limited foil is also clear in Fig. 6.3(c), which wraps and compresses the "cluster-like" plasma. This is the reason why we can still observe a stable, well-confined slice structure at a later time. The attosecond electron slices are continually pulled out by the intense electric field from the center which can be regarded as an electron injection source, and are accelerated in an opposite direction. Meanwhile, a monoenergetic proton bunch with peak energy as high as 1.5 GeV and energy spread $\sim 8\%$ is obtained, that should be, until now, the best results for ion acceleration in the light-sail regime.

For comparison, we also do simulations with linearly polarized laser pulses as displayed in Fig. 6.3(d-f). Unfortunately, we fail to observe any attosecond electron bunch in Fig. 6.3(d). The reason should be attributed to the strong electron heating, e.g., $\mathbf{J} \times \mathbf{B}$ heating or pon-

deromotive heating, due to the oscillating component in the ponderomotive force as described by $f_p = (e^2/4\gamma m_e\omega_0^2)\partial E^2[1+\cos(2\omega_0 t)]/\partial z$. The laser pulse penetrates the foil, modulates the movement of the hot electrons, and propagates freely in the laser direction, as shown in Fig. 6.3(f). Finally, the protons also spread in space and the energy spectrum shows a thermal distribution as seen in Fig. 6.3(e). This indicates a totally different acceleration mechanism from the droplet case where attosecond electron bunches can be generated by using a linearly polarized laser pulse through the so-called Mie theory [128]. However, in our case the laser radiation pressure plays a dominant role for the electron acceleration.

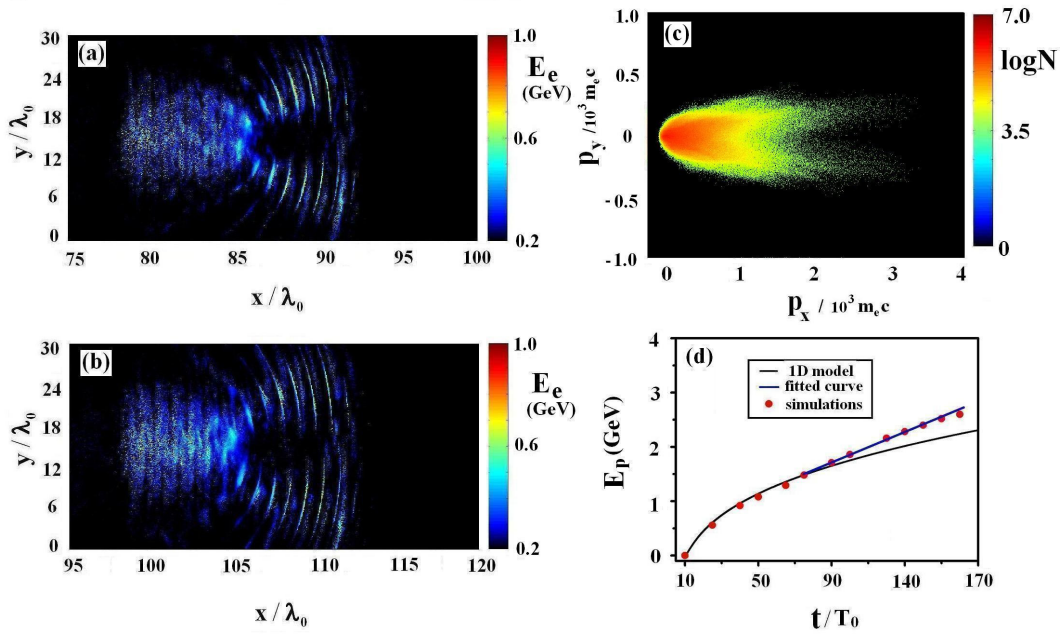

Figure 6.4: Electron energy distribution in space at (a) $t = 100T_0$ and (b) $120T_0$. (c) Electron momentum distribution in space at $t = 120T_0$: p_x vs p_y. (d) Proton peak energy evolution.

We have to note that a full-width flat foil might also generate attosecond electron bunches as long as the lateral laser pulse can penetrate through the "deformation zone" of the foil. However, the electron bunch has a much worse quality, e.g., lower energies and shorter lifetime. It is because the penetrated electromagnetic wave is significantly modified by the laser-foil interaction and the attosecond electron bunches are pulled out in an anisotropic way.

In order to check robustness of the scheme, we show the electron energy distribution in space as depicted in Fig. 6.4(a,b). As we can see, the energetic electron bunches can keep a very stable attosecond structure even at $t = 120T_0$ when they already propagated for about 250fs. More impressive is the high energies ($\sim$ GeV) and densities ($\sim 5n_c$). This is beyond the prediction of the 1D light-sail model, from which the electron energy is only a few

MeV. Actually, in recent years several schemes have been suggested to produce ultra-short attosecond electron bunches, such as by using the laser wakefield accelerator [129], or by the interaction of moderate laser pulse with plasma channel [130], wire or slice targets [131, 132], nanofilms [133], and submicro droplets [128]. However, the obtained electron energy is only a few to a few tens of MeV which limits not only the lifetime of the attosecond electron bunch itself, but also the brightness and even wavelength of the radiation [129]. In our case, the obtained energy is significantly higher than in those schemes. This implies, absolutely, new physics or mechanism inside.

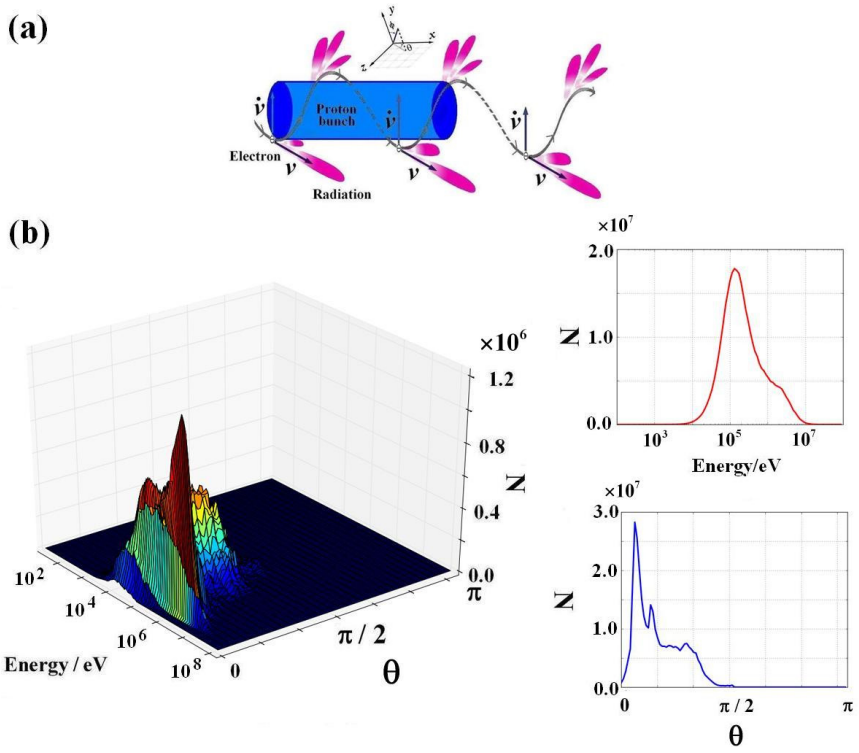

Figure 6.5: (a) Schematic of the laser pressure driven vine-trunk model. (b) The spectrum of the betatron-like radiation in the 3D case.

We set up a model, called laser-driven vine-trunk model, to interpret the high electron energies in the light-sail regime, as shown in Fig. 6.5(a). In this model, the protons are driven by the laser radiation pressure at the velocity described by Eq.(2.7). The electrons move together with the protons at the very beginning and start to oscillate in the transverse direction. The frequency of the electron oscillation is comparable to the relativistic plasma frequency [134, 135], $\omega_\beta = \sqrt{4\pi e^2 n_i/2\gamma_e m_e}$. The laser electric field can be written as $\mathbf{E} = \mathbf{E}_0 e^{-i(\omega_0 t - kx)}$ with $\mathbf{E}_0 = m_e c\omega_0 \mathbf{a}_0/e$. Thus, the laser frequency as witnessed by a electron at a specific location $x_t = v_{||}t$ is $\Omega = \omega_0 - kv_{||} = \omega_0(1 - v_{||}/c)$. When the transverse electron oscillation frequency, ω_β, gets close to the laser frequency, Ω, a betatron resonance

occurs and an efficient energy coupling between the laser pulse and the electron takes place. The resonance condition can be rewritten as

$$1 - \frac{v_{\parallel}}{c} - \sqrt{\frac{n_i/n_c}{2\gamma_{\rm e}}} \sim 0, \tag{6.21}$$

Here, $v_{\parallel}/c = p_{\parallel}/\sqrt{1+p_{\parallel}^2+p_{\perp}^2}$. Noting that $v_{\parallel}/c = \sqrt{1-1/\gamma_{\parallel}^2}$, we obtain $p_{\parallel}^2 = (\gamma_{\parallel}^2 - 1)(1+\mu^2 a_0^2)$ where we assume $p_{\perp} = \mu a_0$ with μ a constant. Considering $a_0 \gg 1$, we finally derive the formula

$$p_{\parallel} \simeq \mu a_0 \sqrt{\gamma_{\parallel}^2 - 1}, \tag{6.22}$$

$$\gamma_{\rm e} = \sqrt{1+\mu^2 a_0^2 \gamma_{\parallel}^2} \approx \mu a_0 \gamma_{\parallel}, \tag{6.23}$$

With the development of the laser-foil interaction, the ion density n_i decreases significantly but the energy $\gamma_{\rm e}$ increases a lot. When $\mu \gg 1$, Eq. (6.21) is well satisfied and a betatron-like resonance occurs, vice versa. In our simulations, we get the maximum $p_x = 2000$ and $p_y(p_z) = 380 \approx 4a$ at $t = 120T_0$ as seen in Fig. 6.4(c) which shows clearly that the transverse motion of the electrons is essentially oscillations driven resonantly by the laser field. In fact, we can also get $\gamma_{\rm e} \approx 2078$, $v_{\parallel}/c \approx 0.962$ and the ion density $6n_c$ at this time point from the simulations. Obviously, the resonance condition Eq. (6.21) is really stratified and the energy exchange takes place. We can also estimate the critical energy of the attosecond electron bunches in this model. Taking $\mu = 4$ and $\gamma_{\parallel} = \gamma_p = 4$ ($E_p \approx 3$ GeV), then we can get $\gamma_{\rm e} = 1050$ and $E_{\rm e} = 525$ MeV, which agrees well with the simulations in Fig. 6.4(a,b). For the maximum energy, considering $\gamma_{\parallel} \gg \gamma_p$, it can be up to a few GeV.

Furthermore, we observe an obvious enhancement of the proton peak energy as displayed in Fig. 6.4(d). The peak deviates from the 1D prediction since $t = 80T_0$. The only reason for the energy enhancement should be attributed to the betatron-like resonance introduced energy coupling between the laser and electrons, which enables more energies transferred from electrons to the protons through the space-charge separation field.

Finally, we show the radiation spectrum in Fig. 6.5(b). As we can see, most radiation is well collimated in the forward direction, e.g., $\theta = 25^{\circ}$ and the total photon number is up to 10^9. More impressive is the high photon energies with a broad band ranging from hundreds KeV to a few MeV. This means that the radiation is actually hard X-ray and even γ burst. Meanwhile, the brightness of the radiation is about 10^7 photons/eV. It is the first time to observe such a short brilliant, small divergency, and broad frequency spread radiation in the light-sail

regime, which might be served as a novel compact short-wavelength radiation source. This ultra-short duration and even femtosecond temporal domain are of great importance for time-resolved studies of atomic and molecular dynamics, chemical and biological process, plasma diagnostics, etc. [15, 136]

6.4 Conclusion

In this chapter, we first concentrated on the radiation reaction effects on the ion acceleration in the PIC code. At any given time, we suppose that the radiation spectrum is synchrotron-like and the relativistic electrons emit radiation along their momentum direction with the spectrum defined by the function $S(\omega/\omega_c)$. Instead of using the complicated Landau-Lifshitz (LL) equation [123], we make use of the momentum conservation law in the code programming, track all electrons with energy above the threshold, calculate the radiation from each electron, and record the emitted photon numbers. The validation of the algorithm has been demonstrated in several previous work.

By using the modified code, we studied in detail the electron acceleration in the light-sail regime and found a new mechanism for the generation of dense GeV spiral electrons with an obvious attosecond structure from a mass-limited foil target. It is shown that the electrons move together with the protons longitudinally and rotate dramatically around the latter in the transverse direction. The strong periodic electric field of the overtaking laser pulse, $E_\perp$, leads to the attosecond electron bunches generation. When the oscillation frequency of the electron gets close to the laser frequency as witnessed by the electron, a betatron-like resonance occurs and an effective energy exchange between the laser and electrons takes place. The radiation-lost energy can thus be compensated for and the proton acceleration can also be enhanced through the space-charge separation field. The produced GeV electron bunches can keep a very stable attosecond structure with a few GeV energies and much longer lifetime as compared to previous schemes [128, 130, 131, 132, 133]. The emitted hard X-ray have a high-brightness (10^7photons/eV), small divergency ($25°$) and broad frequency spread (10KeV-10MeV), which may be served as a novel compact short-wavelength radiation source in future.

Chapter 7

Summary and outlook

Laser-driven plasma-based ion accelerators have attracted increasing attention in recent years due to their diverse applications and significant advantages as compared to the conventional ion accelerators. Several ion acceleration mechanisms have been proposed to produce high-energy, low-divergency, and small-energy spread ion beams, such as, TNSA, shock wave acceleration, Coulomb explosion, and so on. However, the energy conversion efficiency from the laser to ion beams is still very low and the quality of the produced ion beams is far away from the requirements of real applications. Till now, the highest proton energy obtained in laser-plasma experiments is only 67.5 MeV with less than 20% energy conversion efficiency. For direct application of ion beams in oncology, one requires protons with energy $E \sim 235 - 250$ MeV, spread $\Delta E/E \leq 1\%$, flux $N = 10^{12}$, dose 5×10^{10} pr/s, or heavy carbon ions with energy $E \sim 120 - 400$ MeV/u, dose 4×10^{8} pr/s, so that one can use the Bragg-peak to treat a tumor close to a fragile and vital organ. Obviously, it is a long way to apply the laser-driven ions in medical application and an efficient ion acceleration mechanism should be explored, which can deliver the required quality ion beams.

Since the advent of the CPA technology in 1985, the laser intensity is continuously increasing and has reached $2.2 \times 10^{22}\mathrm{Wcm}^{-2}$ recently, which stimulated the research on the laser-driven ion acceleration. In this dissertation, we discuss in detail one of the most promising and efficient ion acceleration mechanisms, namely, radiation pressure acceleration or light-sail regime that was initially proposed for propelling interstellar vehicle by terrestrial laser beam. Recently, this regime was re-visited because of the remarkable advancement in focused laser intensity. One of the advantages of the light-sail regime is the high energy conversion efficiency, that is, in principle, as high as 100% in a 1D case. Based on a simple "flying plasma mirror" model, accurate expressions of the ion energy, velocity, and the correlation between

the ion momentum and ion energy were derived. It is found that, for the lower ion momentum $p \ll 1$ or velocity $\beta \ll \sqrt{2}/2$, $p \approx At$ where A is a constant. As the target approaches the speed of light ($\beta \to 1$), $p \approx (3/4At)^{1/3}$. This indicates that the ion energy initially increases at a rate of $(It/\rho)^2$, but slows to $(It/\rho)^{1/3}$. These conclusions are well demonstrated by a series of 1D simulations.

However, when we extend the model to multi-dimensional cases, several issues come of, such as foil target deformation and transverse instabilities. These multi-dimensional effects should be carefully attended for better understanding a real experiment. In real experiments, when a transversely Gaussian laser pulse irradiates a flat foil, the foil is soon distorted that results in strong electron heating and thus a broad energy spectrum. To overcome the foil target deformation and realize a uniform foil acceleration, a so-called shaped foil target (SFT) is suggested, in which it is shown by multi-dimensional PIC simulations that the ion acceleration structure can be kept for a longer time compared to a normal flat target. The final spectrum shows a monoenergetic character. To demonstrate the robustness of the scheme, several facts such as the surface roughness and the transverse profile of the shaped foil on the ion acceleration are evaluated. An optimal foil cutoff thickness and spot size are given by multi-parametric PIC simulations that should benefit the future experiments and applications.

Besides, we also suggest an alternative method to produce high quality proton beams by avoiding the foil target deformation using the so-called density modulated foil target (DMFT). In this case, the initial foil target is a flat one, but the transverse plasma density follows a Gaussian distribution to match the laser intensity profile. A circularly polarized laser pulse is employed, and is normally incident on this target from the left boundary. Both 2D and 3D simulations have been performed, which shows that protons from the center part of the target can be monoenergetically accelerated and are well collimated in the forward direction. Overall, the beam quality is improved as compared to the case using a SFT. The reason should be attributed to the surface curvature of the SFT that makes the electromagnetic wave obliquely irradiate the foil surface. The resulting electron heating is inevitable though it is not so significant as in a flat foil case.

By using the proposed SFT and DMFT, we succeed in avoiding the foil target deformation and obtaining uniform proton acceleration. However, the acceleration structure is still not stable because of the fast-growth of Rayleigh-Taylor-like (RT) instability. In multi-dimensional PIC simulations, it is shown that the proton-RT instability can be significantly suppressed by using a two-ion-species shaped foil. The physics underlying the simulations is abundant and worth studying in detail. We create a simple three-interface model to interpret the suppression of proton-RT instability, which agrees well with the numerical observations in a variety of cases. A stable compact proton beam acceleration is observed, for the first time, in the 3D geometry. This should be attributed to two effects: ion species separation and heavier

ion spreading in space. The laser pulse does not penetrate the foil and the radiation pressure mainly acts on the carbon ion layer. The carbon ions act to buffer the compact proton layer from the RT-like instability. It is also found that with the decrease of the carbon ions charge state, both the RT instability and Coulomb explosion become increasingly violent and tend to degrade the monoenergetic proton beam. Furthermore, the robustness of the stable two-ion-species regime is checked by the full 3D simulations.

Finally, we study in detail the radiation reaction effects on the ion acceleration. For simplicity, we modify the PIC code according to the momentum conservation law. At any given time, we suppose that the radiation spectrum is synchrotron-like and the relativistic electrons emit radiation along their momentum direction. Previous simulations have demonstrated the validation of the assumption. By using the modified code, we study the electron dynamics in the light-sail regime and observe the generation of GeV spiral electron bunches with a clear attosecond structure. It is shown that the electrons move together with the protons longitudinally and rotate dramatically around the latter in the transverse direction. The strong periodic electric field of the overtaking laser pulse, $E_{\perp}$, leads to the attosecond electron bunches generation. When the oscillation frequency of the electron gets close to the laser frequency as witnessed by the electron, a betatron-like resonance occurs and an effective energy exchange between the laser and electrons takes place. Such energetic spiral electron bunches would be of great interest for the emission of efficient betatron-like X-ray and even γ burst, which might have diverse applications, e.g., in oncology and plasma diagnostics.

We have to note that, a tunable and efficient ion acceleration mechanism is not available up to now. Although a two-ion-species shaped foil can produce a stable light-ion acceleration, the energy conversion efficiency is very low because the heavy ions occupy most laser energy. Besides, a new and complete solution to overcome or suppress RT-like instability should be explored in the light-sail regime to produce a stable and monoenergetic proton beam. The recently proposed method using a surface imposed modulation should be a candidate and is worthy of the research in the future [137].

As discussed in Chapter 2, the energy gain in the light-sail regime becomes much slower at later time even though we don't consider the multi-dimensional effects. Therefore, the light-sail regime is only favorable to produce GeV ion beams. However, we might combine the light-sail regime with other ion acceleration mechanisms, such as TNSA and even Bubble regime [138]. For the latter, we might pre-accelerate the protons in the light-sail regime and then eject them into the acceleration phase of the Bubble field. 2D simulations have already demonstrated the validation of the scheme and the final energy of the protons could be up to near sub-TeV, although there are still several tough issues in this case.

For energetic electron bunch generation in the light-sail regime, we have to deduce the exact

scaling law. The effects of the foil geometry and laser parameters on the electron generation should be considered in the following research. For the betatron-like hard X-ray emission, we have to characterize the spectrum in detail so that it can contribute to the future experimental studies.

In summary, we have demonstrated a stable, efficient, and tunable ion acceleration, although we did encounter several problems and challenges. We hope that our efforts in producing a usable ion beam will contribute to ongoing research of producing ion beams for oncology.

Bibliography

[1] D. Strickland and G. Mourou. Compression of amplified chirped optical pulses. *Optics Communications*, 56(3):219–221, 1985.

[2] P. Maine and G. Mourou. Amplification of 1-nsec pulses in nd: glass followed by compression to 1 psec. *Optics Letters*, 13(6):467–469, 1988.

[3] RR Freeman, PH Bucksbaum, H. Milchberg, S. Darack, D. Schumacher, and ME Geusic. Above-threshold ionization with subpicosecond laser pulses. *Physical Review Letters*, 59(10):1092–1095, 1987.

[4] MV Ammosov, NB Delone, and VP Krainov. Tunnel ionization of complex atoms and of atomic ions in an alternating electromagnetic field. *Sov Phys JETP*, 64(6):1191–1194, 1986.

[5] G. Mainfray and G. Manus. Multiphoton ionization of atoms. *Reports on Progress in Physics*, 54:1333, 1991.

[6] A. Pukhov. Strong field interaction of laser radiation. *Reports on Progress in Physics*, 66:47, 2003.

[7] B. Dromey, M. Zepf, A. Gopal, K. Lancaster, MS Wei, K. Krushelnick, M. Tatarakis, N. Vakakis, S. Moustaizis, R. Kodama, et al. High harmonic generation in the relativistic limit. *Nature Physics*, 2(7):456–459, 2006.

[8] U. Teubner and P. Gibbon. High-order harmonics from laser-irradiated plasma surfaces. *Reviews of Modern Physics*, 81(2):445, 2009.

[9] C. Winterfeldt, C. Spielmann, and G. Gerber. Colloquium: Optimal control of high-harmonic generation. *Reviews of Modern Physics*, 80(1):117, 2008.

[10] H. Hamster, A. Sullivan, S. Gordon, W. White, and RW Falcone. Subpicosecond, electromagnetic pulses from intense laser-plasma interaction. *Physical Review Letters*, 71(17):2725–2728, 1993.

[11] Z.M. Sheng, K. Mima, J. Zhang, and H. Sanuki. Emission of electromagnetic pulses from laser wakefields through linear mode conversion. *Physical Review Letters*, 94(9):095003, 2005.

[12] R. Bonifacio, C. Pellegrini, and LM Narducci. Collective instabilities and high-gain regime in a free electron laser. *Optics Communications*, 50(6):373–378, 1984.

[13] F. Pegoraro and SV Bulanov. Photon bubbles and ion acceleration in a plasma dominated by the radiation pressure of an electromagnetic pulse. *Physical Review Letters*, 99(6):065002, 2007.

[14] G.A. Mourou, T. Tajima, and S.V. Bulanov. Optics in the relativistic regime. *Reviews of Modern Physics*, 78(2):309, 2006.

[15] M. Uiberacker, T. Uphues, M. Schultze, AJ Verhoef, V. Yakovlev, MF Kling, J. Rauschenberger, NM Kabachnik, H. Schröder, M. Lezius, et al. Attosecond real-time observation of electron tunnelling in atoms. *Nature*, 446(7136):627–632, 2007.

[16] T. Tajima and JM Dawson. Laser electron accelerator. *Physical Review Letters*, 43(4):267–270, 1979.

[17] B.M. Hegelich, BJ Albright, J. Cobble, K. Flippo, S. Letzring, M. Paffett, H. Ruhl, J. Schreiber, RK Schulze, and JC Fernandez. Laser acceleration of quasi-monoenergetic mev ion beams. *Nature*, 439(7075):441–444, 2006.

[18] H. Schwoerer, S. Pfotenhauer, O. Jäckel, K.U. Amthor, B. Liesfeld, W. Ziegler, R. Sauerbrey, KWD Ledingham, and T. Esirkepov. Laser-plasma acceleration of quasi-monoenergetic protons from microstructured targets. *Nature*, 439(7075):445–448, 2006.

[19] S. Ichimaru. Nuclear fusion in dense plasmas. *Reviews of Modern Physics*, 65(2):255, 1993.

[20] T. Esirkepov, M. Borghesi, SV Bulanov, G. Mourou, and T. Tajima. Highly efficient relativistic-ion generation in the laser-piston regime. *Physical Review Letters*, 92(17):175003, 2004.

[21] A. Macchi, S. Veghini, and F. Pegoraro. "light sail" acceleration reexamined. *Physical Review Letters*, 103(8):085003, 2009.

[22] XQ Yan, M. Chen, ZM Sheng, and JE Chen. Self-induced magnetic focusing of proton beams by weibel-like instability in the laser foil-plasma interactions. *Physics of Plasmas*, 16:044501, 2009.

[23] T.P. Yu, A. Pukhov, G. Shvets, and M. Chen. Stable laser-driven proton beam acceleration from a two-ion-species ultrathin foil. *Physical Review Letters*, 105(6):065002, 2010.

[24] A. Zhidkov, J. Koga, A. Sasaki, and M. Uesaka. Radiation damping effects on the interaction of ultraintense laser pulses with an overdense plasma. *Physical Review Letters*, 88(18):185002, 2002.

[25] S.W. Bahk, P. Rousseau, TA Planchon, V. Chvykov, G. Kalintchenko, A. Maksimchuk, GA Mourou, and V. Yanovsky. Generation and characterization of the highest laser intensities (10^{22} W/cm^2). *Optics Letters*, 29:2837–2839, 2004.

[26] V. Yanovsky, V. Chvykov, G. Kalinchenko, P. Rousseau, T. Planchon, T. Matsuoka, A. Maksimchuk, J. Nees, G. Cheriaux, G. Mourou, et al. Ultra-high intensity-300-tw laser at 0.1 hz repetition rate. *Optics Express*, 16(3):2109–2114, 2008.

[27] E. Esarey, CB Schroeder, and WP Leemans. Physics of laser-driven plasma-based electron accelerators. *Reviews of Modern Physics*, 81(3):1229, 2009.

[28] WP Leemans, B. Nagler, AJ Gonsalves, C. Toth, K. Nakamura, CGR Geddes, E. Esarey, CB Schroeder, and SM Hooker. Gev electron beams from a centimetre-scale accelerator. *Nature Physics*, 2(10):696–699, 2006.

[29] A. Caldwell, K. Lotov, A. Pukhov, and F. Simon. Proton-driven plasma-wakefield acceleration. *Nature Physics*, 5(5):363–367, 2009.

[30] SC Wilks, AB Langdon, TE Cowan, M. Roth, M. Singh, S. Hatchett, MH Key, D. Pennington, A. MacKinnon, and RA Snavely. Energetic proton generation in ultra-intense laser–solid interactions. *Physics of Plasmas*, 8:542, 2001.

[31] R.W. Hellwarth. *Advances in Quantum Electronics*. New York:Comlumbia University Press, 1961.

[32] H.W. Mocker and RJ Collins. Mode competition and self-locking effects in a q-switched ruby laser. *Applied Physics Letters*, 7(10):270–273, 1965.

[33] A.V. Korzhimanov, AA Gonoskov, E.A. Khazanov, and A.M. Sergeev. Horizons of petawatt laser technology. *Physics-Uspekhi*, 54:9, 2011.

[34] A. Dubietis, G. Jonuauskas, and A. Piskarskas. Powerful femtosecond pulse generation by chirped and stretched pulse parametric amplification in bbo crystal. *Optics Communications*, 88(4-6):437–440, 1992.

[35] MD Perry, D. Pennington, BC Stuart, G. Tietbohl, JA Britten, C. Brown, S. Herman, B. Golick, M. Kartz, J. Miller, et al. Petawatt laser pulses. *Optics Letters*, 24(3):160–162, 1999.

[36] See more information for Extreme-Light-Infrastructure. http://www.extreme-light-infrastructure.eu.

[37] See more information for NIF. https://lasers.llnl.gov.

[38] See more information for HiPER. http://www.hiper-laser.org.

[39] T. Tajima and J. Jpn. Soc. therapy rad. *Oncol*, 9:83, 1998.

[40] SV Bulanov and VS Khoroshkov. Feasibility of using laser ion accelerators in proton therapy. *Plasma Physics Reports*, 28(5):453–456, 2002.

[41] E. Fourkal, JS Li, W. Xiong, A. Nahum, and CM Ma. Intensity modulated radiation therapy using laser-accelerated protons: a monte carlo dosimetric study. *Physics in Medicine and Biology*, 48:3977, 2003.

[42] WL Kruer and K. Estabrook. J×b heating by very intense laser light. *Physics of Fluids*, 28:430, 1985.

[43] P. Gibbon. *Short Pulse Interactions with Matter: An Introduction*. London:Imperial College Press, 2005.

[44] M.C. Kaluza. Laser-based particle acceleration. *Optik and Photonik*, 5(2):56–59, 2010.

[45] A. Pukhov and J. Meyer-ter Vehn. Laser wake field acceleration: the highly non-linear broken-wave regime. *Applied Physics B: Lasers and Optics*, 74(4):355–361, 2002.

[46] A. Pukhov and S. Gordienko. Bubble regime of wake field acceleration: similarity theory and optimal scalings. *Philosophical Transactions of the Royal Society A: Mathematical, Physical and Engineering Sciences*, 364(1840):623, 2006.

[47] SPD Mangles, CD Murphy, Z. Najmudin, AGR Thomas, JL Collier, AE Dangor, EJ Divall, PS Foster, JG Gallacher, CJ Hooker, et al. Monoenergetic beams of relativistic electrons from intense laser–plasma interactions. *Nature*, 431(7008):535–538, 2004.

[48] CGR Geddes, C. Toth, J. Van Tilborg, E. Esarey, CB Schroeder, D. Bruhwiler, C. Nieter, J. Cary, and WP Leemans. High-quality electron beams from a laser wakefield accelerator using plasma-channel guiding. *Nature*, 431(7008):538–541, 2004.

[49] J. Faure, Y. Glinec, A. Pukhov, S. Kiselev, S. Gordienko, E. Lefebvre, J.P. Rousseau, F. Burgy, and V. Malka. A laser–plasma accelerator producing monoenergetic electron beams. *Nature*, 431(7008):541–544, 2004.

[50] K. Nakamura, B. Nagler, C. Tóth, CGR Geddes, CB Schroeder, E. Esarey, WP Leemans, AJ Gonsalves, and SM Hooker. Gev electron beams from a centimeter-scale channel guided laser wakefield accelerator. *Physics of Plasmas*, 14:056708, 2007.

[51] CE Clayton, JE Ralph, F. Albert, RA Fonseca, SH Glenzer, C. Joshi, W. Lu, KA Marsh, SF Martins, WB Mori, et al. Self-guided laser wakefield acceleration beyond 1 gev using ionization-induced injection. *Physical Review Letters*, 105(10):105003, 2010.

[52] D. Neely. Laser driven ion acceleration developments. *Advanced Accelerator Concepts Workshop 2010*, June, 2010, in Annapolis (adapted).

[53] L.O. Silva, M. Marti, J.R. Davies, R.A. Fonseca, C. Ren, F.S. Tsung, and W.B. Mori. Proton shock acceleration in laser-plasma interactions. *Physical Review Letters*, 92(1):15002, 2004.

[54] L. Ji, B. Shen, X. Zhang, F. Wang, Z. Jin, X. Li, M. Wen, and J.R. Cary. Generating monoenergetic heavy-ion bunches with laser-induced electrostatic shocks. *Physical Review Letters*, 101(16):164802, 2008.

[55] X. Zhang, B. Shen, L. Ji, F. Wang, Z. Jin, X. Li, M. Wen, and J.R. Cary. Ion acceleration with mixed solid targets interacting with circularly polarized lasers. *Physical Review Special Topics-Accelerators and Beams*, 12(2):021301, 2009.

[56] E. Fourkal, I. Velchev, and C.M. Ma. Coulomb explosion effect and the maximum energy of protons accelerated by high-power lasers. *Physical Review E*, 71(3):036412, 2005.

[57] S.P. Hatchett, C.G. Brown, T.E. Cowan, E.A. Henry, J.S. Johnson, M.H. Key, J.A. Koch, A.B. Langdon, B.F. Lasinski, R.W. Lee, et al. Electron, photon, and ion beams from the relativistic interaction of petawatt laser pulses with solid targets. *Physics of Plasmas*, 7:2076, 2000.

[58] P.A. Norreys. Laser-driven particle acceleration. *Nature Photonics*, 3(8):423–425, 2009.

[59] P. Mora. Plasma expansion into a vacuum. *Physical Review Letters*, 90(18):185002, 2003.

[60] J. Fuchs, P. Antici, et al. Laser-driven proton scaling laws and new paths towards energy increase. *Nature Physics*, 2(1):48–54, 2005.

[61] J. Schreiber, F. Bell, F. Grüner, U. Schramm, M. Geissler, M. Schnürer, S. Ter-Avetisyan, B.M. Hegelich, J. Cobble, E. Brambrink, et al. Analytical model for ion acceleration by high-intensity laser pulses. *Physical Review Letters*, 97(4):045005, 2006.

[62] M. Passoni, L. Bertagna, and A. Zani. Target normal sheath acceleration: theory, comparison with experiments and future perspectives. *New Journal of Physics*, 12:045012, 2010.

[63] RA Snavely, MH Key, SP Hatchett, TE Cowan, M. Roth, TW Phillips, MA Stoyer, EA Henry, TC Sangster, MS Singh, et al. Intense high-energy proton beams from petawatt-laser irradiation of solids. *Physical Review Letters*, 85(14):2945–2948, 2000.

[64] APL Robinson, M. Zepf, S. Kar, RG Evans, and C. Bellei. Radiation pressure acceleration of thin foils with circularly polarized laser pulses. *New Journal of Physics*, 10:013021, 2008.

[65] S.D. Baton, M. Koenig, P. Guillou, B. Loupias, A. Benuzzi-Mounaix, J. Fuchs, C. Rousseaux, L. Gremillet, D. Batani, A. Morace, et al. Relativistic electron transport and confinement within charge-insulated, mass-limited targets. *High Energy Density Physics*, 3(3-4):358–364, 2007.

[66] F. Perez, L. Gremillet, M. Koenig, SD Baton, P. Audebert, M. Chahid, C. Rousseaux, M. Drouin, E. Lefebvre, T. Vinci, et al. Enhanced isochoric heating from fast electrons produced by high-contrast, relativistic-intensity laser pulses. *Physical Review Letters*, 104(8):085001, 2010.

[67] S. Buffechoux, J. Psikal, M. Nakatsutsumi, L. Romagnani, A. Andreev, K. Zeil, M. Amin, P. Antici, T. Burris-Mog, A. Compant-La-Fontaine, et al. Hot electrons transverse refluxing in ultraintense laser-solid interactions. *Physical Review Letters*, 105(1):015005, 2010.

[68] T. Kluge, W. Enghardt, SD Kraft, U. Schramm, K. Zeil, TE Cowan, and M. Bussmann. Enhanced laser ion acceleration from mass-limited foils. *Physics of Plasmas*, 17:123103, 2010.

[69] T. Kluge, W. Enghardt, SD Kraft, U. Schramm, Y. Sentoku, K. Zeil, TE Cowan,

R. Sauerbrey, and M. Bussmann. Efficient laser-ion acceleration from closely stacked ultrathin foils. *Physical Review E*, 82(1):016405, 2010.

[70] Y. Sentoku, K. Mima, H. Ruhl, Y. Toyama, R. Kodama, and TE Cowan. Laser light and hot electron micro focusing using a conical target. *Physics of Plasmas*, 11:3083, 2004.

[71] H. Nakamura, B. Chrisman, T. Tanimoto, M. Borghesi, K. Kondo, M. Nakatsutsumi, T. Norimatsu, M. Tampo, KA Tanaka, T. Yabuuchi, et al. Superthermal and efficient-heating modes in the interaction of a cone target with ultraintense laser light. *Physical Review Letters*, 102(4):045009, 2009.

[72] R. Sonobe, S. Kawata, S. Miyazaki, M. Nakamura, and T. Kikuchi. Suppression of transverse proton beam divergence by controlled electron cloud in laser-plasma interactions. *Physics of Plasmas*, 12:073104, 2005.

[73] T. Okada, AA Andreev, Y. Mikado, and K. Okubo. Energetic proton acceleration and bunch generation by ultraintense laser pulses on the surface of thin plasma targets. *Physical Review E*, 74(2):026401, 2006.

[74] M. Nakamura, S. Kawata, R. Sonobe, Q. Kong, S. Miyazaki, N. Onuma, and T. Kikuchi. Robustness of a tailored hole target in laser-produced collimated proton beam generation. *Journal of Applied Physics*, 101:113305, 2007.

[75] TP Yu, YY Ma, M. Chen, FQ Shao, MY Yu, YQ Gu, and Y. Yin. Quasimonoenergetic proton beam from ultraintense-laser irradiation of a target with holed backside. *Physics of Plasmas*, 16:033112, 2009.

[76] M.P. Liu, H.C. Wu, B.S. Xie, J. Liu, H.Y. Wang, and MY Yu. Energetic collimated ion bunch generation from an ultraintense laser interacting with thin concave targets. *Physics of Plasmas*, 15:063104, 2008.

[77] XH Yang, YY Ma, FQ Shao, H. Xu, MY Yu, YQ Gu, TP Yu, Y. Yin, CL Tian, and S. Kawata. Collimated proton beam generation from ultraintense laser-irradiated hole target. *Laser and Particle Beams*, 28(02):319–325, 2010.

[78] SA Gaillard, T. Kluge, KA Flippo, M. Bussmann, B. Gall, T. Lockard, M. Geissel, DT Offermann, M. Schollmeier, Y. Sentoku, and TE Cowan. Increased laser-accelerated proton energies via direct laser-light-pressure acceleration of electrons in microcone targets. *Physics of Plasmas*, 18:056710, 2011.

[79] M. Roth, TE Cowan, MH Key, SP Hatchett, C. Brown, W. Fountain, J. Johnson, DM Pennington, RA Snavely, SC Wilks, et al. Fast ignition by intense laser-accelerated proton beams. *Physical Review Letters*, 86(3):436–439, 2001.

[80] A. Lévy, T. Ceccotti, P. D'Oliveira, F. Réau, M. Perdrix, F. Quéré, P. Monot, M. Bougeard, H. Lagadec, P. Martin, et al. Double plasma mirror for ultrahigh temporal contrast ultraintense laser pulses. *Optics Letters*, 32(3):310–312, 2007.

[81] C. Thaury, F. Quéré, J.P. Geindre, A. Levy, T. Ceccotti, P. Monot, M. Bougeard, F. Réau, et al. Plasma mirrors for ultrahigh-intensity optics. *Nature Physics*, 3(6):424–429, 2007.

[82] G. Marx. Interstellar vehicle propelled by terrestrial laser beam. *Nature*, 211, 1966.

[83] A. Macchi, F. Cattani, T.V. Liseykina, and F. Cornolti. Laser acceleration of ion bunches at the front surface of overdense plasmas. *Physical Review Letters*, 94(16):165003, 2005.

[84] X. Zhang, B. Shen, X. Li, Z. Jin, and F. Wang. Multistaged acceleration of ions by circularly polarized laser pulse: Monoenergetic ion beam generation. *Physics of Plasmas*, 14:073101, 2007.

[85] X. Zhang, B. Shen, X. Li, Z. Jin, F. Wang, and M. Wen. Efficient gev ion generation by ultraintense circularly polarized laser pulse. *Physics of Plasmas*, 14:123108, 2007.

[86] XQ Yan, C. Lin, ZM Sheng, ZY Guo, BC Liu, YR Lu, JX Fang, and JE Chen. Generating high-current monoenergetic proton beams by a circularlypolarized laser pulse in the phase-stableacceleration regime. *Physical Review Letters*, 100(13):135003, 2008.

[87] M. Chen, A. Pukhov, TP Yu, and ZM Sheng. Enhanced collimated gev monoenergetic ion acceleration from a shaped foil target irradiated by a circularly polarized laser pulse. *Physical Review Letters*, 103(2):024801, 2009.

[88] LL Ji, BF Shen, XM Zhang, FC Wang, ZY Jin, CQ Xia, M. Wen, WP Wang, JC Xu, and MY Yu. Generating quasi-single-cycle relativistic laser pulses by laser-foil interaction. *Physical Review Letters*, 103(21):215005, 2009.

[89] M. Chen, T.P. Yu, A. Pukhov, and Z.M. Sheng. Target shape effects on monoenergetic gev proton acceleration. *New Journal of Physics*, 12:045004, 2010.

[90] B. Qiao, M. Zepf, M. Borghesi, and M. Geissler. Stable gev ion-beam acceleration from thin foils by circularly polarized laser pulses. *Physical Review Letters*, 102(14):145002, 2009.

[91] TP Yu, M. Chen, and A. Pukhov. High quality gev proton beams from a density-modulated foil target. *Laser and Particle Beams*, 27(04):611–617, 2009.

[92] HB Zhuo, ZL Chen, W. Yu, ZM Sheng, MY Yu, Z. Jin, and R. Kodama. Quasimonoenergetic proton bunch generation by dual-peaked electrostatic-field acceleration in foils irradiated by an intense linearly polarized laser. *Physical Review Letters*, 105(6):65003, 2010.

[93] H.C. Wu, J. Meyer-ter Vehn, J. Fernández, and BM Hegelich. Uniform laser-driven relativistic electron layer for coherent thomson scattering. *Physical Review Letters*, 104(23):234801, 2010.

[94] SV Bulanov, E.Y. Echkina, T.Z. Esirkepov, IN Inovenkov, M. Kando, F. Pegoraro, and G. Korn. Unlimited ion acceleration by radiation pressure. *Physical Review Letters*, 104(13):135003, 2010.

[95] TP Yu, A. Pukhov, G. Shvets, M. Chen, TH Ratliff, SA Yi, and V. Khudik. Simulations of stable compact proton beam acceleration from a two-ion-species ultrathin foil. *Physics of Plasmas*, 18:043110, 2011.

[96] A. Henig, S. Steinke, M. Schnürer, T. Sokollik, R. Hörlein, D. Kiefer, D. Jung, J. Schreiber, BM Hegelich, XQ Yan, et al. Radiation-pressure acceleration of ion beams driven by circularly polarized laser pulses. *Physical Review Letters*, 103(24):245003, 2009.

[97] VK Tripathi, CS Liu, X. Shao, B. Eliasson, and RZ Sagdeev. Laser acceleration of monoenergetic protons in a self-organized double layer from thin foil. *Plasma Physics and Controlled Fusion*, 51:024014, 2009.

[98] APL Robinson, P. Gibbon, M. Zepf, S. Kar, RG Evans, and C. Bellei. Relativistically correct hole-boring and ion acceleration by circularly polarized laser pulses. *Plasma Physics and Controlled Fusion*, 51:024004, 2009.

[99] AA Gonoskov, AV Korzhimanov, VI Eremin, AV Kim, and AM Sergeev. Multicascade proton acceleration by a superintense laser pulse in the regime of relativistically induced slab transparency. *Physical Review Letters*, 102(18):184801, 2009.

[100] A. Pukhov. 3d electromagnetic relativistic particle-in-cell code vlpl: Virtual laser plasma lab. *J. Plasma Phys. v61*, 425.

[101] M. Chen, A. Pukhov, ZM Sheng, and XQ Yan. Laser mode effects on the ion acceleration during circularly polarized laser pulse interaction with foil targets. *Physics of Plasmas*, 15:113103, 2008.

[102] C.A.J. Palmer, NP Dover, I. Pogorelsky, M. Babzien, GI Dudnikova, M. Ispiriyan, MN Polyanskiy, J. Schreiber, P. Shkolnikov, V. Yakimenko, et al. Monoenergetic pro-

ton beams accelerated by a radiation pressure driven shock. *Physical Review Letters*, 106(1):14801, 2011.

[103] L. Cao, W. Yu, MY Yu, H. Xu, XT He, Y. Gu, Z. Liu, J. Li, and C. Zheng. Nonlinear laser focusing using a conical guide and generation of energetic ions. *Physical Review E*, 78(3):036405, 2008.

[104] N. Naumova, T. Schlegel, VT Tikhonchuk, C. Labaune, IV Sokolov, and G. Mourou. Hole boring in a dt pellet and fast-ion ignition with ultraintense laser pulses. *Physical Review Letters*, 102(2):25002, 2009.

[105] X.R. Hong, B.S. Xie, S. Zhang, H.C. Wu, A. Aimidula, X.Y. Zhao, and M.P. Liu. High quality ion acceleration from a double-layer target dominated by the radiation pressure of a transversely gaussian laser pulse. *Physics of Plasmas*, 17:103107, 2010.

[106] AY Cho and JR Arthur. Progress in solid state chemistry. *Pergamon, New York*, 10:157, 1975.

[107] J.E. Mahan. *Physical Vapor Deposition of Thin Films*. New York:Wiley, 2000.

[108] See more information for CVD. http://www.crystec.com/tridepe.htm.

[109] CJ McKinstrie and EA Startsev. Electron acceleration by a laser pulse in a plasma. *Physical Review E*, 54(2):1070–1073, 1996.

[110] Y. Hadad, L. Labun, J. Rafelski, N. Elkina, C. Klier, and H. Ruhl. Effects of radiation reaction in relativistic laser acceleration. *Physical Review D*, 82(9):096012, 2010.

[111] R.T. Hammond. Radiation reaction at ultrahigh intensities. *Physical Review A*, 81(6):062104, 2010.

[112] M. Chen, A. Pukhov, T.P. Yu, and Z.M. Sheng. Radiation reaction effects on ion acceleration in laser foil interaction. *Plasma Physics and Controlled Fusion*, 53:014004, 2011.

[113] M. Tamburini, F. Pegoraro, A. Di Piazza, CH Keitel, and A. Macchi. Radiation reaction effects on radiation pressure acceleration. *New Journal of Physics*, 12:123005, 2010.

[114] L. Rayleigh. On waves propagated along the plane surface of an elastic solid. *Proceedings of the London Mathematical Society*, 1(1):4, 1885.

[115] G. Taylor. The instability of liquid surfaces when accelerated in a direction perpendicular to their planes. i. *Proceedings of the Royal Society of London. Series A, Mathe-*

matical and Physical Sciences, 201(1065):192–196, 1950.

[116] SV Bulanov, T.Z. Esirkepov, D. Habs, F. Pegoraro, and T. Tajima. Relativistic laser-matter interaction and relativistic laboratory astrophysics. *The European Physical Journal D-Atomic, Molecular, Optical and Plasma Physics*, 55(2):483–507, 2009.

[117] SS Bulanov, A. Brantov, V.Y. Bychenkov, V. Chvykov, G. Kalinchenko, T. Matsuoka, P. Rousseau, S. Reed, V. Yanovsky, DW Litzenberg, et al. Accelerating monoenergetic protons from ultrathin foils by flat-top laser pulses in the directed-coulomb-explosion regime. *Physical Review E*, 78(2):026412, 2008.

[118] AV Brantov and V.Y. Bychenkov. Monoenergetic proton beams from mass-limited targets irradiated by ultrashort laser pulses. *Plasma Physics Reports*, 36(3):256–262, 2010.

[119] O. Klimo, J. Psikal, J. Limpouch, and VT Tikhonchuk. Monoenergetic ion beams from ultrathin foils irradiated by ultrahigh-contrast circularly polarized laser pulses. *Physical Review Special Topics-Accelerators and Beams*, 11(3):031301, 2008.

[120] V.Y. Bychenkov, VN Novikov, D. Batani, VT Tikhonchuk, and SG Bochkarev. Ion acceleration in expanding multispecies plasmas. *Physics of Plasmas*, 11:3242, 2004.

[121] K. Ostrikov. Colloquium: Reactive plasmas as a versatile nanofabrication tool. *Reviews of Modern Physics*, 77(2):489, 2005.

[122] J.D. Jackson. *Classical Electrodynamics*. New York: Wiley, 1962.

[123] L.D. Landau and E.M. Lifshitz. *The Classical Theory of Fields*. Pergamon:London, 1979.

[124] S. Kiselev, A. Pukhov, and I. Kostyukov. X-ray generation in strongly nonlinear plasma waves. *Physical Review Letters*, 93(13):135004, 2004.

[125] I.V. Sokolov, N.M. Naumova, J.A. Nees, G.A. Mourou, and V.P. Yanovsky. Dynamics of emitting electrons in strong laser fields. *Physics of Plasmas*, 16:093115, 2009.

[126] P.A.M. Dirac. Classical theory of radiating electrons. *Proceedings of the Royal Society of London. Series A. Mathematical and Physical Sciences*, 167(929):148, 1938.

[127] A. Rousse, K.T. Phuoc, R. Shah, A. Pukhov, E. Lefebvre, V. Malka, S. Kiselev, F. Burgy, J.P. Rousseau, D. Umstadter, et al. Production of a kev x-ray beam from synchrotron radiation in relativistic laser-plasma interaction. *Physical Review Letters*, 93(13):135005, 2004.

[128] TV Liseykina, S. Pirner, and D. Bauer. Relativistic attosecond electron bunches from laser-illuminated droplets. *Physical Review Letters*, 104(9):095002, 2010.

[129] MJH Luttikhof, AG Khachatryan, FA van Goor, and K.J. Boller. Generating ultrarelativistic attosecond electron bunches with laser wakefield accelerators. *Physical Review Letters*, 105(12):124801, 2010.

[130] N.M. Naumova, J.A. Nees, and G.A. Mourou. Relativistic attosecond physics. *Physics of Plasmas*, 12:056707, 2005.

[131] Y.Y. Ma, Z.M. Sheng, Y.T. Li, W.W. Chang, X.H. Yuan, M. Chen, H.C. Wu, J. Zheng, and J. Zhang. Dense quasi-monoenergetic attosecond electron bunches from laser interaction with wire and slice targets. *Physics of Plasmas*, 13:110702, 2006.

[132] XH Yang, H. Xu, YY Ma, FQ Shao, Y. Yin, HB Zhuo, MY Yu, and CL Tian. Propagation of attosecond electron bunches along the cone-and-channel target. *Physics of Plasmas*, 18(2):3109, 2011.

[133] V.V. Kulagin, V.A. Cherepenin, M.S. Hur, and H. Suk. Theoretical investigation of controlled generation of a dense attosecond relativistic electron bunch from the interaction of an ultrashort laser pulse with a nanofilm. *Physical Review Letters*, 99(12):124801, 2007.

[134] A. Pukhov, Z.M. Sheng, and J. Meyer-ter Vehn. Particle acceleration in relativistic laser channels. *Physics of Plasmas*, 6:2847, 1999.

[135] C. Gahn, GD Tsakiris, A. Pukhov, J. Meyer-ter Vehn, G. Pretzler, P. Thirolf, D. Habs, and KJ Witte. Multi-mev electron beam generation by direct laser acceleration in high-density plasma channels. *Physical Review Letters*, 83(23):4772–4775, 1999.

[136] A.L. Cavalieri, N. Müller, T. Uphues, V.S. Yakovlev, A. Baltuška, B. Horvath, B. Schmidt, L. Blümel, R. Holzwarth, S. Hendel, et al. Attosecond spectroscopy in condensed matter. *Nature*, 449(7165):1029–1032, 2007.

[137] M. Chen, N. Kumar, A. Pukhov, and T.P. Yu. Stabilized radiation pressure dominated ion acceleration from surface modulated thin-foil targets. *Physics of Plasmas*, 18:073106, 2011.

[138] L.L. Yu, H. Xu, W.M. Wang, Z.M. Sheng, B.F. Shen, W. Yu, and J. Zhang. Generation of tens of gev quasi-monoenergetic proton beams from a moving double layer formed by ultraintense lasers at intensity (10^{21}-10^{23}W/cm^2). *New Journal of Physics*, 12(4):5021, 2010.

List of publications

Published papers

- **T. P. Yu**, Y. Y. Ma, M. Chen, F. Q. Shao, M. Y. Yu, Y. Q. Gu, and Y. Yin, "Quasimonoenergetic proton beam from ultraintense-laser irradiation of a target with holed backside", *Phys. Plasma* **16**, 033112 (2009). based on Chapter 1
- **T. P. Yu**, M. Chen, and A. Pukhov, "High quality GeV proton beams from a density-modulated foil target", *Laser Part. Beams* **27**, 611-617 (2009).
based on Chapter 3,4.
- **T. P. Yu**, A. Pukhov, G. Shvets, and M. Chen, "Stable Laser-Driven Proton Beam Acceleration from a Two-Ion-Species Ultrathin Foil", *Phys. Rev. Lett.* **105**, 065002 (2010).
based on Chapter 5.
- **T. P. Yu**, A. Pukhov, G. Shvets, M. Chen, T. H. Ratliff, S. A. Yi, and V. Khudik, "Simulations of stable compact proton beam acceleration from a two-ion-species ultrathin foil", *Phys. Plasmas* **18**, 043110 (2011). based on Chapter 2,5.
- M. Chen, A. Pukhov, **T. P. Yu**, and Z. M. Sheng, "Enhanced Collimated GeV Monoenergetic Ion Acceleration from a Shaped Foil Target Irradiated by a Circularly Polarized Laser Pulse", *Phys. Rev. Lett.* **103**, 024801 (2009). based on Chapter 2,3.
- M. Chen, **T. P. Yu**, A. Pukhov, and Z. M. Sheng, "Target shape effects on monoenergetic GeV proton acceleration", *NEW J. Phys.* **12** 045004 (2010).
based on Chapter 2,3.
- M. Chen, A. Pukhov, **T. P. Yu**, and Z. M. Sheng, "Radiation reaction effects on ion acceleration in laser foil interaction", *Plasma Phys. Control. Fusion* **53**, 014004 (2011).
based on Chapter 6.
- M. Chen, N. Kumar, A. Pukhov, and **T. P. Yu**, "Stabilized Radiation Pressure Dominated Ion Acceleration from Surface modulated Thin-foil Targets", *Phys. Plasma* **18**, 073106 (2011).

- Y. Y. Ma, Z. M. Sheng, Y. Q. Gu, M. Y. Yu, Y. Yin, F. Q. Shao, **T. P. Yu**, and W. W. Chang, "High-quality MeV protons from laser interaction with umbrellalike cavity target", *Phys. Plasma* **16**, 034502 (2009).
- X. H. Yang, Y. Y. Ma, F. Q. Shao, H. Xu, M. Y. Yu, Y. Q. Gu, **T. P. Yu**, Y. Yin, C. L. Tian, and S. Kawata, "Collimated proton beam generation from ultraintense laser-irradiated hole target", *Laser and Particle Beams* **28**, 319-325 (2010).

Submitted papers

- **T. P. Yu**, A. Pukhov, N. Kumar, *et. al.*, "GeV spiral electron bunches generation and betatron-like hard X-ray emission from radiation pressure acceleration of thin solid foil targets", submitted to *Phys. Rev. Lett.* (2011). based on Chapter 2,6.
- Y. Y. Ma, S. Kawata, **T. P. Yu**, Y. Q. Gu, Z. M. Sheng, M. Y. Yu, H. J. Liu, H. B. Zhuo, Y. Yin, K. Takahashi, X. Y. Xie, C. L. Tian, and F. Q. Shao, "Electron bow-wave injection in laser-driven bubble acceleration", submitted to *Phys. Rev. E* (2011).

International conference

- Tongpu Yu, Alexander Pukhov, and Min Chen, "Stable proton beam acceleration from a two-species subwavelength foil", 30th International Workshop on Physics of High Energy Density in Matter, at Waldemar-Petersen-Haus, Hirschegg, Austria (2010.2). (Poster)
- T.P. Yu, A. Pukhov, and M. Chen, "Stable Proton Beam Acceleration from a Two-species Ultrathin Foil Target", 1st International particle acceleration conference (IPAC10), at Kyoto International Conference Center (KICC), Kyoto, Japan (2010.5). (Poster)
- Tong-Pu Yu, Min Chen, Gennady Shvets, and Alexander Pukhov, "Stable proton beam acceleration in two-ion-species regime dominated by the laser radiation pressure", 5th Asia summer school and symposium on laser-plasma acceleration and radiation, in Blue palace hotel, Shanghai, China (2010.8). (Invited talk)
- Tongpu Yu, Alexander Pukhov, Gennady Shvets, and Min Chen, "Stable proton beam acceleration in two-ion-species foils", 31st International Workshop on Physics of High Energy Density in Matter, at Waldemar-Petersen-Haus, Hirschegg, Austria (2011.2). (Talk)
- Tongpu Yu, Alexander Pukhov, Naveen Kumar, and Zhengming Sheng, "GeV spiral electron generation and betatron-like hard X-ray emission from radiation pressure acceleration of thin solid foil targets", ISTC-GSI YOUNG SCIENTISTS SCHOOL 2011 "Ultra-High Intensity Light Science and Applications", GSI, Darmstadt, Germany (2011.10). (Poster)

Acknowledgement

This dissertation would not have been possible without the guidance, help, and support from several individuals. First and foremost, I express my deepest gratitude to my supervisor, Prof. Dr. Alexander Pukhov, for his detailed and constructive comments, excellent guidance and sufficient patience throughout this work. Without his efficient guidance, I would never have been able to finish my phd so smoothly in three years.

I am deeply grateful to Prof. Gennady Shvets from University of Texas at Austin and Dr. Min Chen from Lawrence Berkeley National Laboratory for their detailed and constructive comments and for their important supports throughout the work. I also appreciate Prof. Dr. K.H. Spatschek as my second referee and his valuable comments on the thesis.

I wish to express my warm and sincere thanks to my colleagues and friends, Dr. Naveen Kumar, Dr. Ajit Upadhyay, Oliver Jansen, Dr. Daniel der Brügge, Tobias Tueckmantel, Dr. Götz Lehmann, Prof. Dr. Mingyang Yu, Prof. Dr. Yunfeng Liang, Dr. Feng Liu, Prof. Zhengming Sheng, and Johannes Thomas. They have inspired me so much during my studying, such as code programming, paper writing and organizing, and so on. I will never forget the discussions with them on various topics covering physical problems, politics and education issues, life and dream, etc. Especially, I thank Mrs. Elvira Gröters and Mr. Evgenij Bleile for their great help and suggestions during my studying in Düsseldorf. Meanwhile, I also thank Institut für Theoretische Physik I, for providing me with such an excellent atmosphere for doing research.

I owe my most sincere gratitude to my Chinese supervisor Prof. Fuqiu Shao and Dr. Yanyun Ma. They have always provided me sufficient support and caring for my studying in Germany.

Last but not the least, I owe my loving thanks to my family in China. Without their encouragement and understanding, it would have been impossible for me to finish this work.

The financial support of China Scholarship Council and conference attending supports from TR18, GRK1203, and DAAD, are also gratefully acknowledged.

Erklärung

Hiermit erkläre ich vorliegende Dissertation selbstständig verfasst, keine anderen als die angegebenen Quellen und Hilfsmittel benutzt, sowie Zitate kenntlich gemacht zu haben.

Düsseldorf, den